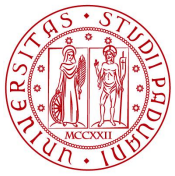

UNIVERSITÀ DEGLI STUDI DI PADOVA

Dipartimento di Ingegneria Industriale DII

Corso di Laurea Magistrale in Ingegneria Aerospaziale

Investigation of vibrational conveyors parameters for the transport of lunar regolith

---

Relatore: Prof. Mirco Zaccariotto

Corelatore: Prof. Philipp Reiss (TUM)

Tutor: M.Sc. Alexander Smolka (TUM)

Alessandro G. Scudeler - 2018733

ANNO ACCADEMICO 2022/2023

A Nonna Nives

Contents

List of Tables

List of Figures

Abstract

This thesis explores one possible application of the concept of *In Situ Resource Utilization* (ISRU) for space exploration: the transport and handling of regolith through the use of vibratory conveyors. A vibratory conveyor with piezoelectric actuators was identified as being the ideal setup for use on the surface of the Moon, due to its low-power requirements and low number of moving part. An experimental campaign was conducted on the model, investigating the effect of vibration amplitude, frequency, and trough inclination on the bulk material flow, constituted of monosized glass sphere. The results showed a more than linear relationship between frequency and transport time, highlighting the effect of resonance in the conveyor discharge flow. A *Discrete Element Method* (DEM) simulation was developed as a digital twin of the setup. The numerical model was validated with both analytical and experimental results showing good accordance with real-life experiments, with the model being able to predict the evolution of mass flow and transport speed due to the variation of actuation frequency. The DEM model was then used to obtain new results in the low-gravity environments of the Moon and Mars, resulting in the observation of a much higher predicted mass flow than what observed under Earth's gravity. This thesis provides a basis for the development of a more advanced simulation setups to help in the design of vibratory conveyors specialized for ISRU on extraterrestrial environments.

Abstract

Questa tesi si focalizza su una possibile applicazione pratica del concetto di *In Situ Resource Utilization* (ISRU) nell'ambito dell'esplorazione spaziale: il trasporto e la gestione della regolite lunare tramite l'utilizzo di trasportatori vibranti. I trasportatori vibranti, attuati tramite attuatori piezoelettrici, sono stati identificati come soluzione ideale per future operazioni logistiche sulla superficie lunare, grazie al loro basso consumo energetico e al ridotto numero di componenti mobili soggetti all'erosione causata dalla regolite. Al fine di comprendere le capacità di trasporto di tali strumenti, è stata condotta una campagna sperimentale su un modello in scala, studiando le variazioni del comportamento di trasporto del materiale in base all'ampiezza e alla frequenza di vibrazione, nonché all'inclinazione del trasportatore stesso. I test sono stati effettuati utilizzando un particolare materiale granulare composto da sfere di vetro di dimensioni uniformi e conosciute, al fine di limitare la variabilità sperimentale. I risultati hanno dimostrato una relazione non lineare tra la frequenza di vibrazione e il tempo totale di trasporto per una determinata quantità di materiale, evidenziando l'effetto positivo della risonanza meccanica tra l'attuatore e i giunti elastici sul flusso di scarico del trasportatore. Allo stesso tempo, è stato sviluppato un modello numerico basato sul *Discrete Element Method* (DEM) per simulare il comportamento del setup sperimentale. Il modello numerico è stato implementato utilizzando il linguaggio di programmazione scientifica ad alte prestazioni *Julia* e successivamente validato utilizzando sia risultati analitici che sperimentali, mostrando una buona corrispondenza con i risultati ottenuti dagli esperimenti. La simulazione è stata in grado di predire con un buon livello di precisione l'evoluzione del flusso di massa trasportato e della velocità di trasporto in base alla variazione della frequenza di vibrazione. Una volta calibrato e validato, il modello DEM è stato utilizzato per ottenere nuovi risultati sulle prestazioni di tali sistemi in ambienti a bassa gravità, come la superficie della Luna e di Marte. In generale, per tali ambienti, è stata osservata una previsione di flusso di massa molto più elevata rispetto a quella prevista in gravità terrestre, a causa delle diverse interazioni tra le particelle, le vibrazioni di attuazione e l'accelerazione di gravità locale. Questa tesi si propone di fornire una base per lo sviluppo ulteriore di simulazioni più avanzate, che possano fungere da strumenti di supporto nella progettazione di trasportatori vibranti specializzati per l'ISRU in ambienti extraterrestri.

Chapter 1

Introduction

The ability to efficiently perform In Situ Resource Utilization (ISRU) is a critical requirement for long-term exploration of the Moon and Mars, where the establishment of a future planetary base is becoming more and more of a reality. ISRU is the process of using the resources found on a planet or moon to support human exploration, settlement, and scientific advancement. This is an essential approach to the exploration of celestial bodies where transporting materials from Earth can be difficult and expensive. A variety of materials can be useful to humans: water found on the surface of a planet can be processed into breathable oxygen and fuel, while other resources such as metals, minerals, and gases can be used in a wide range of construction and manufacturing processes. By harnessing and utilizing locally available resources, ISRU can help reduce the cost and risk of space exploration and enable humans to establish sustainable bases on other planets.

In this process, solving the problem of material conveyance proves to be an essential necessity, especially for granular materials such as lunar regolith. Considering the constraints that exist on the lunar surface, a vibratory conveyor proves to be a more suitable logistical solution for transporting bulk materials than a belt conveyor due to its simple configuration, low number of moving parts, and reduced energy consumption [1]. In addition, this type of system can be manufactured from heat- and corrosion-resistant materials, making it an ideal solution for harsh environments such as the lunar surface. Therefore, a vibratory conveyor was chosen as an ideal candidate to solve the problem of bulk material handling for ISRU application. A particularly interesting application for vibratory conveyors is their use as a sensor feed system in rovers or other planetary installations, where a small and precise amount of material is required, necessitating a precise flow control system. In particular, piezoelectric actuators were chosen as the main actuation system for the conveyor since, being practically devoid of moving parts, they offer the best chance at surviving the harsh erosive effect of lunar regolith.

While the utilization and study of these logistic solutions has been going on for decades, their operation in extraterrestrial environments is still an open research field, with a lack of availability of experimental data on which to base the design of future systems. Therefore, the development of a suitable simulation code is of high research interest, allowing researchers and engineers to test and predict the behavior of their systems without the need to build expensive experimental setups for each iteration. Simulations prove to be an invaluable tool in the early design phase,

where many different configurations and designs need to be tested, making this process much faster than it would be if there was a need to experimentally test all the different approaches. In the case of bulk solids, the most common simulation algorithms are based on the Discrete Element Method developed by Cundall in 1979 [2]. Many different variations have been devised over the years, but the basic idea has remained the same: to simulate the evolution of bulk materials by computing and evolving over time the motion of thousands of virtual particles that can collide and interact with each other.

Therefore, this thesis will focus on both aspects of the problem: on the one hand, a large part of the work will be focused on the study of vibratory conveyors and on an extensive experimental campaign carried out on an existing conveyor setup, while at the same time, a discrete element model simulation code will be developed from scratch to be used as a new tool for the preliminary study of these systems. The newly acquired experimental knowledge on the discharge behavior of vibratory conveyors will be used to calibrate the numerical model and to validate its results, providing insight into the errors introduced by the simulation code with respect to the experimental data. Finally, the calibrated model will be used to simulate the performance of vibratory conveyors installed under lunar and Martian gravity, providing new insights into the possibility of using these systems for ISRU applications. The main topic of interest will be the analysis of the effect of different actuation parameters on the transport performance of the system, with particular emphasis on the possibility of controlling the discharged mass flow via simple control systems acting on the frequency and amplitude of the excitation system.

1.1 State of the art

Vibratory conveyors have been in use for over a century, with the first patent filed in 1886 by Oliver Evans for a vibratory feeder. However, it wasn't until the 1950s that vibratory conveyors became popular for industrial use due to their ability to efficiently transport materials while being low maintenance and durable.

In a vibratory conveyor, a vibration motor generates a force that causes the conveyor to vibrate, which, in turn, propels the material along the conveyor bed. Such conveyors can be designed to move materials in a straight line or to rotate them in a circular motion, offering a versatile solution commonly implemented in various industrial settings. Indeed, vibratory conveyors, often referred to as vibration feeders, are used across many different industries, including food processing, pharmacy, mining, and recycling. One of their key advantages lies in their capability to handle a wide range of materials, from powders to large pieces, while being relatively low-maintenance and easy to clean. This is primarily attributed to the presence of fewer moving parts compared to other types of mechanical conveyors. They can also operate at high speeds and with high precision, making them ideal for applications where accuracy is critical, as well as being relatively energy efficient [3]. In recent years, advances in technology have led to numerous improvements in the design of vibratory conveyors: the use of electromagnetic drives has allowed more precise control of vibration frequency and amplitude [4] [5], while the use of advanced materials and coatings has improved the durability and longevity of this type of system.

On the other hand, the evolution of simulations regarding the behavior of bulk materials is still an open field with a lot of research efforts still dedicated to it. The Discrete Element Method (DEM) has been used for decades to model the behavior of granular materials with an increasing

level of detail. In a DEM approach, bulk solids are treated as a collection of discrete particles, each governed by the laws of mechanics, that can move and interact freely in a meshless environment. This numerical model was first developed by Cundall and Strack in 1979 [2] and applied to the study of geomechanics. These early approaches made use of virtual rigid disks, as they were initially limited to two-dimensional simulations, but as time went on and the computational resources available increased, Cundall proposed a new three-dimensional approach in 1988 [6] which made use of rigid spheres. At the same time he worked on another aspect of the problem resulting in the paper by Hart et al [7] which presented the first implementation of a discrete element model code that could work with two-dimensional polygons of arbitrary shape, paving the way for much more complex and realistic simulations. These new methods quickly evolved to handle three-dimensional polyhedral particles with both rigid and elastic material responses. As the technique evolved and matured, it was applied to various fields of research and engineering, ranging from engineering mechanics, to the study of rocks and soils. It has been applied to the study of statistical micromechanics by Cundall [6], to the study of the behavior of granular soils by Ting et al. [8], and to the analysis of the structure in jointed rocks by Morris et al. [9].

Due to its flexibility, DEM is ideally suited to implement more sophisticated particle interactions in the simulation, such as long-range electromagnetic effects. An example of this application was first proposed by Laurentie et al. [10], who implemented a tribocharging model in a two-dimensional DEM simulation to study its effect on polyamide and polycarbonate particles in a vibrating bed. The work was further developed by Rasera et al. [11] who extended the tribocharging model to three-dimensional DEM simulations. All these approaches in different topics show the incredible flexibility and power of this kind of computational simulations, which prove to be an invaluable tool to study the behavior of bulk and granular materials.

Chapter 2

Theoretical Background

This chapter delves into the fundamental physical principles necessary for the development and implementation of the methods presented in the subsequent parts of this thesis. The focus centers on the theory background essential for comprehending the Discrete Element Method (DEM) which utilizes a collision model that incorporates springs and dampeners to simulate particle interactions. Therefore, a clear understanding of the underlying physical laws holds significant importance for the thesis continuation.

Furthermore, the chapter explores the concept of the harmonic oscillator, a fundamental model employed to study systems exhibiting periodic motion. This system is relevant to the Discrete Element Model implementation due to the fact that inter-particle interactions mimic the behavior of a dampened harmonic oscillator. The chapter further discusses the distinctions between damped and undamped oscillators and their applications in various physical systems, with the hope of providing a clear and solid understanding of the physical principles underlying these models.

2.1 Spring, dampeners and harmonic oscillators

As will be explained in the following chapters, the theoretical impact model for DEM simulations describes the interaction between two particles with a mass-spring-damper model. It is therefore useful to quickly present here the mathematical description of these two key components, the spring and the dampener, to provide a complete theoretical background to understand the inner workings of the simulation algorithm.

2.1.1 Springs

Springs are common mechanical components utilized in a wide range of applications, such as suspensions, shock absorbers, and mechanical watches. They consists of an elastic, but still largely rigid, material shaped into a particular form that can return into its original shape after being compressed or extended. The amount of energy stored is directly proportional to the degree of deformation. In an ideal scenario, where the spring possesses a perfectly constant stiffness, it exerts a force that corresponds to its change in length. but, in the real world, this relationship is still applicable in the case of *small deflections*. To quantify the behavior of a spring, we introduce the

concept of the *spring constant*. The spring constant represents the ratio between the mechanical deflection of the spring and the force generated and it is typically dependent on the geometry and material properties of the spring. The spring constant is typically expressed in units of force divided by distance, such as Newton per meter ($\mathrm{N\,m^{-1}}$).

The mathematical description of an ideal spring follows *Hooke's Law*, which states that the force with which the spring reacts to the deformation is linearly proportional to the distance from its equilibrium length:

$$F = -kx \tag{2.1}$$

where x represents the displacement, k is the spring constant and F is the exerted force. This description can be considered a good representation of the behavior when the springs are not stretched or compressed beyond their elastic limit.

2.1.2 Dampeners

Dampeners, also known as dashpots, are another class of mechanical devices that resists motion via viscous friction employing this effect to dissipate energy. They are often used to reduce the amplitude of oscillations in mechanical systems and to prevent damage caused by excessive vibrations. The analysis of dampers is a little more elaborate compared to the one of springs since it is necessary to consider peculiar properties such as damping coefficient, damping ratio, and energy dissipation.

The main descriptor for typical viscous dampeners is the *damping coefficient* that is the defined as the ratio between the force applied by the dashpot and the velocity with which its output is moving:

$$c = \frac{F}{v} \tag{2.2}$$

where F is the force and v is the velocity of the damper. The energy dissipated per unit time by a dampener is proportional to the damping coefficient and the square of the velocity:

$$P = cv^2 \tag{2.3}$$

Another important coefficient that helps to describe the behavior of this component is the *damping ratio*, which is used as an indication of the effectiveness of a damper in reducing the amplitude of oscillations in a particular mass-spring-dampener system. This parameter is defined as the ratio between the aforementioned damping coefficient c and the critical damping coefficient c_{cr} that will be better defined in the next chapter.

$$\zeta = \frac{c}{c_{cr}} = \frac{c}{2\sqrt{mk}} \tag{2.4}$$

2.1.3 Harmonic oscillators

The combination of a mass, a spring and, eventually, a dampener, generates one of the most basic model used in physics, the harmonic oscillator. This kind of models can be applied to wide variety of natural events and can be used to describe pendulums, acoustical systems, RLC circuits or waves. Typically an harmonic oscillator is a system that, when displaced from its equilibrium position is subjected to a restoring force F that is oriented in such a way to push the system back to

its equilibrium position. This kind of systems can be either an ideal oscillator, with no frictional forces, or a dampened oscillator, where some kind of damping proportional to the velocity is added to the system.

Simple harmonic oscillator

A simple example of an harmonic oscillator could be a mass connected on a spring bouncing back and forth without any kind of friction. In general an harmonic oscillator is a system that is neither driven nor damped, that is to say that there are no other forces acting on the mass apart from the restoring force F which always tend to pull the mass m towards the direction of the equilibrium point ($x = 0$) with a magnitude that depends only on the position x of the mass and a constant k. By imposing the balance of the forces, as per Newton's second law, the system yields:

$$F = ma = m\frac{d^2x}{dt^2} = -kx \tag{2.5}$$

By solving this differential equation it is possible to obtain the equation of motion for the point mass:

$$x(t) = A\cos(\omega t + \phi) \tag{2.6}$$

where ω is the *angular frequency* of the harmonic motion, defined as:

$$\omega = \sqrt{\frac{k}{m}} \tag{2.7}$$

This motion, being described by a sinusoidal function, is periodic with a period $T = 2\pi/\omega$ and frequency $f = 1/T$, and a constant amplitude A. The position at a given time also depends on the *phase* ϕ, which is used to determine the starting point on the sine wave. From Equation 2.7 it is clear that the period and the frequency of the oscillation depend on the mass m and the constant k, while amplitude and phase are determined by the starting conditions. The total mechanical energy stored in an harmonic oscillator is constant over the course of the movement, since there is no kind of energy dissipation, while the potential energy in a generic position x is expressed as:

$$U = \frac{1}{2}kx^2 \tag{2.8}$$

Damped harmonic oscillator

The harmonic oscillator that are observed in real life always shows signs of friction and/or damping, that progressivly slows the motion of the system toward an equilibrium point. In this scenario, in addition to the aforementioned restoring force, the mass is subject to a new frictional force that is acting always against the direction of motion. The friction force F_f can typically be modeled as proportional to the velocity v of the object, according to a proportionality term called *damping coefficient* c:

$$F_f = -cv \tag{2.9}$$

Just as before, to analyze the system, it is useful to impose the balance of the forces, according to Newton's second law:

$$F = -kx - c\frac{dx}{dt} = m\frac{d^2x}{dt^2} \tag{2.10}$$

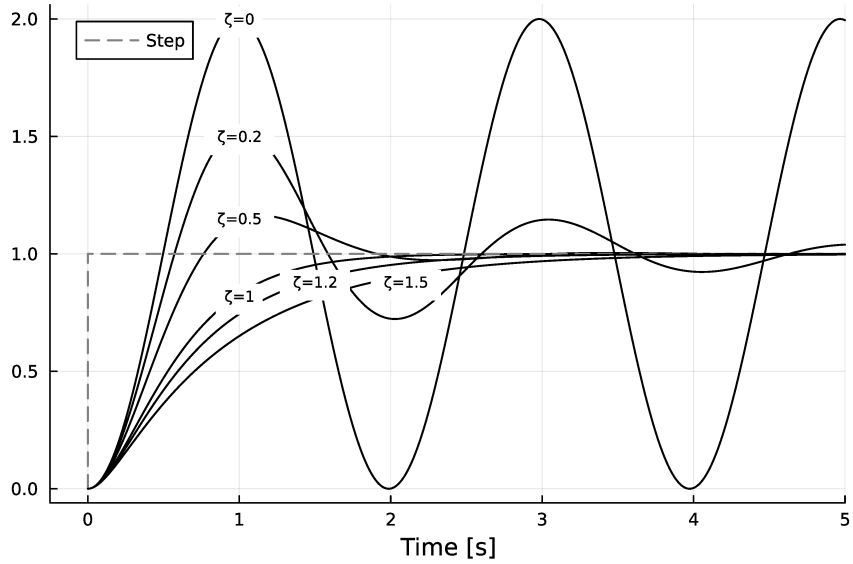

Figure 2.1: Different unit step responses for a damped harmonic oscillator with different values of ζ

Which can be rewritten as:

$$\frac{d^2x}{dt^2} + 2\zeta\omega_0\frac{dx}{dt} + \omega_0^2 x = 0 \tag{2.11}$$

where $\omega_0 = \sqrt{k/m}$ is the undamped angular frequency of the oscillator, as seen before, and $\zeta = c/2\sqrt{mk}$ is the damping ratio.

As was briefly presented in Chapter 2.1.2, the damping ratio is used to define the oscillating behavior of a dampened system. A dampened harmonic oscillator can either be:

Overdamped ($\zeta > 1$) Which characterizes a system that returns to its equilibrium position without oscillating;

Critically Damped ($\zeta = 1$) Which defines a system that returns to its equilibrium condition as quickly as possible without oscillating, although accepting an overshoot;

Underdamped ($\zeta < 1$) Defines a system that oscillates, with a different frequency than in the undamped case, with the oscillation amplitude gradually going to zero and reaching a condition of equilibrium;

The response of the system under a unit step load, with different values of damping ratio are presented in Figure 2.1.

This model can be further expanded upon by considering the action of other driving force, obtaining a *driven harmonic oscillator*. This kind of system can present resonance effects at particular frequencies that amplifies the response of the system to the external force.

2.2 Inclined plane

The problem of studying the motion of objects moving along an inclined plane is a classic physics problem. It involves an object that is sliding down an incline of tilt θ due to the effect of gravity. The problem can include, or not, the presence of friction between the object and the surface. Its solution is straightforward and requires the use of some trigonometry and the laws of motion.

The first step in the solution of this problem is to draw a free body diagram of the object on the tilted plane, as in Figure 2.2. In the diagram the force of gravity is acting on the center of mass of the object, creating its weight force $\vec{P}$, always acting vertically downward. Along the surface of the incline, in a direction opposed to the one in which the object is sliding, it is possible to observe the presence of a frictional force $\vec{f}_a$. Firstly, the weight can be resolved in its two components: one parallel to the inclined plane $\vec{P}_{\parallel}$ and the other perpendicular to the surface $\vec{P}_{\perp}$. The component of the weight that is parallel to the inclined plane surface is the force that is dragging the object down the incline, while the perpendicular component is equal and opposite to the normal force. These two components can be computed with simple trigonometry as:

$$\vec{P}_{\parallel} = \vec{P}\sin(\theta) = mg\sin(\theta) \tag{2.12}$$

$$\vec{P}_{\perp} = \vec{P}\cos(\theta) = mg\cos(\theta) \tag{2.13}$$

Where m is the mass of the object and g is the gravitational acceleration constant.

In the presence of friction between the object and the surface, it is important to consider both types of frictional forces: *static friction*, opposing the motion of the object while it is at rest, and *kinetic friction*, which opposes the motion of the object while it is moving. The magnitude of the static frictional force is given by:

$$F_{static} \leq \mu_s P_{\perp} \tag{2.14}$$

where F_{static} is the static frictional force, μ_s is the coefficient of static friction, and $P_{\perp}$ is the magnitude of the normal force. If the force dragging the object down is less than or equal to the maximum static frictional force, the object will remain at rest while, if the applied force is greater than the maximum static frictional force, the object will begin to move.

The magnitude of the kinetic frictional force is given by:

$$F_{kinetic} \leq \mu_k P_{\perp} \tag{2.15}$$

where $F_{kinetic}$ is the kinetic frictional force, μ_k is the coefficient of kinetic friction, and $P_{\perp}$ is the normal force. It is important to remember that the kinetic frictional force always acts in the opposite direction to the motion of the object. In the case of a non-rolling objects, the solution is pretty much done at this point. If $P_{\parallel}$ results to be bigger than F_{static}, the object will start to slide down the incline. Knowing that, it is possible to sum the two forces that are acting along the inclined surface $P_{\parallel}$ and $f_a = F_{kinetic}$ to obtain the total net force acting on the object $F_{net} = F_{\parallel} - f_a$. By using Newton's second law it is possible to compute the downward acceleration of the object as:

$$a = \frac{F_{net}}{m} \tag{2.16}$$

The other important configuration is the one considering a rolling motion, without slipping, as in Figure 2.3. This kind of motion is the one observed for example in a disk rolling down an

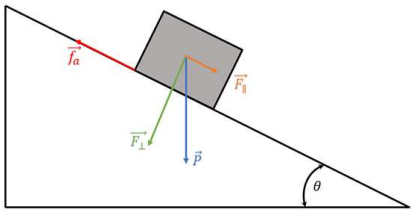

Figure 2.2: Force decomposition for a non rotating object on an inclined plane

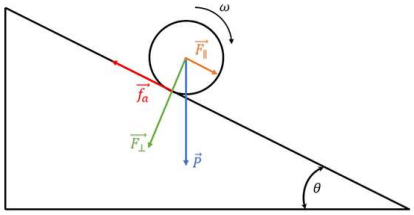

Figure 2.3: Force decomposition for a rotating object on an inclined plane

incline with enough surface static friction to guarantee that the condition of ideal rolling motion is satisfied. The presence of friction is what enables the disk, in this example, to roll down without slipping thanks to a torque generated by friction itself on the disc. Given the equilibrium of the forces, following Newton's second law:

$$P_\parallel - f_a = ma \tag{2.17}$$

$$\implies mg\sin(\theta) - f_a = ma \tag{2.18}$$

it is possible to express the torque τ acting on the disk as:

$$\tau = f_a R = I\alpha \tag{2.19}$$

where R is the radius and I is the inertia moment of the disk, while α indicates the angular acceleration generated by the torque on the disk itself. Knowing that the object is rolling without slipping it is possible to link the angular and linear acceleration to each other through the radius R as:

$$\alpha = \frac{a}{R} \tag{2.20}$$

Knowing that, for a disk, the moment of inertia is equal to $I = 1/2mR^2$, it is possible to substitute the definition of α in Equation 2.19, obtaining:

$$f_a R = \frac{1}{2}mR^2\frac{a}{R} \tag{2.21}$$

$$\implies f_a = \frac{ma}{2} \tag{2.22}$$

By substituting the expression of the frictional force in Equation 2.18 it is possible to solve for the acceleration of the disk:

$$mg\sin\theta - \frac{ma}{2} = ma \tag{2.23}$$

$$mg\sin\theta = \frac{3}{2}ma \tag{2.24}$$

$$a = \frac{2}{3}g\sin\theta \tag{2.25}$$

2.3 The nature of bulk materials

Bulk solids, or bulk materials, are a class of materials composed of a large amount of particles of possibly different size, chemical composition, density and shape, that are grouped together to form a bulk. The mechanical behavior of these materials depends upon many different factors but the main ones can be identified as the size, the shape and the density of the particles comprising the bulk.

Understanding the nature of bulk solids is essential when designing equipment for its handling or storage since these materials present some peculiar characteristics that are not often found in others. That is why this this chapter will focus on a broad overview of bulk solids with the aim of providing a starting base for the evolution of this work.

In the case of bulk solids, the first big difference with other classes of materials is the fact that it is possible to characterize them on two levels:

1. By features describing the behavior of the material in its bulk form, such as the flow properties, moisture content, compaction behavior and electrostatic charging

2. By features describing the characteristics of the constituent particles such as their density, hardness, size, shape and texture

Both approaches will be explored more in depth in this chapter, focusing on achieving a basic understanding of the main numerical parameters used to describe both bulk materials in their bulk form and their constituent particles.

2.3.1 Voids and bulk density

When considering a bulk solid as an arrangement of particles of different shapes and sizes packed together, it is easy to see how there will always be a certain amount of free space between them. The percentage of the total volume not occupied by the particles is the first important parameter for the description of this class of material and is usually referred as *voidage* or *void fraction* ϵ. It is computed as:

$$\epsilon = \frac{V_{voids}}{V_{part} + V_{voids}} \tag{2.26}$$

It is obviously possible to use the complementary term, the *fractional solid content* computed as $(1 - \epsilon)$. The void fraction is obviously subject to continuous changes as the bulk moves around, so its value is typically considered to be the voidage in *static* conditions, with the material at rest. It is important not to confuse the void fraction of the bulk solids with the porosity, which is a term usually used to describe the ration of the volume of pores within a single particle of the bulk, with respect to the particle's total volume.

Typical values of voidage in static bulk materials composed of spheres of the same size can range from about 0.26 for a regular tridimensional hexagonal packing (Figure 2.4a), to around 0.48 for regular cubic packing (Figure 2.4b). In general the voidage usually lies between these two extremes, with a high voidage value corresponding to a loosely packed bulk. This parameter heav-

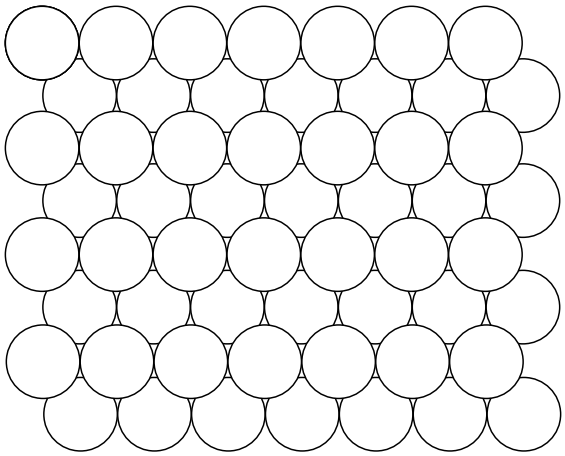

(a) Regular 3D hexagonal arrangement: $\epsilon = 0.26$

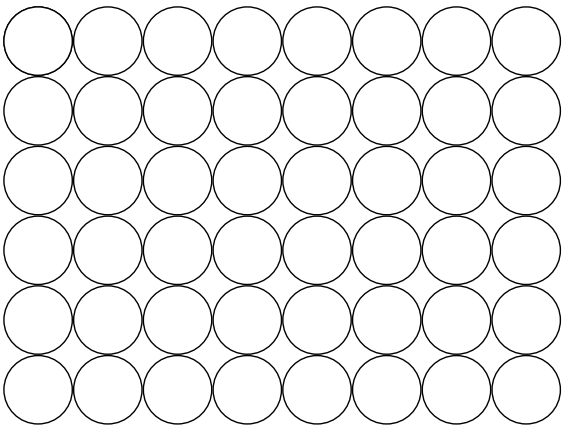

(b) Regular 3D cubic arrangement: $\epsilon = 0.48$

Figure 2.4: Possible regular packing arrangements for spherical particles of the same size

ily depends on the shape and size of the constituent particles since, bulks composed by extremely irregular shapes with small particles, can present much higher void fractions.

The presence of voids in the bulk will make it so that the bulk material will present a macroscopic density that is different from the one of its constituent particles. This apparent density is usually called *bulk density* ρ_b and can be naturally defined as the ratio between the mass of the material and its total volume, comprising the voids:

$$\rho_b = \frac{m_{solids} + m_{voids}}{V_{solids} + V_{voids}} \tag{2.27}$$

If the density of the fluid ρ_f that is filling the voids and the density of the particles ρ_p are known, it is possible to obtain the bulk density as:

$$\rho_b = (\rho_p - \rho_f)(1 - \epsilon) + \rho_f \tag{2.28}$$

In the case of dry bulk solids in a terrestrial environment the voids are usually filled with air and thus the effect of the fluid's density ρ_f would be negligible compared with ρ_p, so that the relationship between bulk and particle density can be rewritten as:

$$\rho_b = \rho_p(1 - \epsilon) \tag{2.29}$$

This equation proves to be valid in vacuum environment, since the voids can be considered almost completely empty with $\rho_f \sim 0$.

As previously noted, both the voidage and the bulk density are dependent on the packing arrangement of the bulk. It is thus necessary to pair any stated value of the bulk density with an indication of the condition of the material at the time of measurement. Usually the main two configurations are the *loose* or *poured* state, where the bulk material was simply poured in the measuring device, and the *packed* state, where the material was packed by dropping the measuring cylinder a couple of times on to a table.

Table 2.1: Qualitative categorization of bulk materials' particle size

Descriptive term	Typical size range	Examples
Coarse solid	5-100 mm	Coal, aggregates, ecc
Granular solid	0.3-5 mm	Granulated sugar,rice, cereals, ecc
Particulate solid:		
Coarse powder	100-300 µm	Table salt
Fine powder	10-100 µm	Icing sugar
Superfine powder	1-10 µm	Face powder
Ultrafine powder	<1 µm	Paint pigments

The determination of the density of the constituent particles, on the other hand, can prove to be particularly difficult, since it requires knowledge of the total particle volume not including the voids. This measurement can be easily obtained when considering larger particles, since it is only necessary to measure the volume of liquid that is displaced by a known mass of particles poured in a measuring cylinder. However, it can prove to be particularly challenging to obtain this value in the case of fine powders that could also face some partial solubilization in the chosen reference liquid. To analyze this types of particles it is almost always necessary to utilize a air-comparison pycnometer [12], a commercially available instrument that works by comparing the buoyancy of a known volume of air with that of the sample, which is placed inside a sealed chamber after an initial calibration made using a reference sample with a known density. The volume of air displaced by the reference sample is measured and compared to the volume of air displaced by the sample of bulk material. Once the displaced volume is known it is possible to compute the density of the bulks' particles even in the case of very fine powders.

2.3.2 Particle size

In the context of bulk solids it is difficult to define a precise meaning of the word *size* of the constituent particles. Particle size is generally used to indicate some kind of average dimension across the particles, often depending on the different industry's standards. It is however useful to introduce the typical size ranges in which bulk materials are typically categorized, using generic terms such as "coarse solid", "fine powder" and so on. An example of a possible classification of bulk materials with respect to the constituent particle's size can be seen in Table 2.1, extracted from the work of Woodcock and Mason [12]. This table contains a possible qualitative description of bulk solids based on the size range of their particles.

Considering the "loose" definition of particle size it is useful to refer back to the simplest ideal particle: the perfectly spherical particle. A mass of monosized, spherical particles can be clearly described by a single dimension, which is the particle diameter. In the same way, a bulk of spherical particles with different sizes can be described by an *average* particle diameter, together with some information on the distribution of the varying sizes around the average value. When particles are non-spherical it becomes more difficult to clearly define a set of parameters to describe the size and shape distribution. In industrial application it is common to approach this problem by representing the size of an irregularly shaped particle with a single, arbitrarily defined quantity, usually some kind of *equivalent diameter* that corresponds to the diameter of a sphere that behaves in the same way under certain conditions, or that offers the same value of some characteristic.

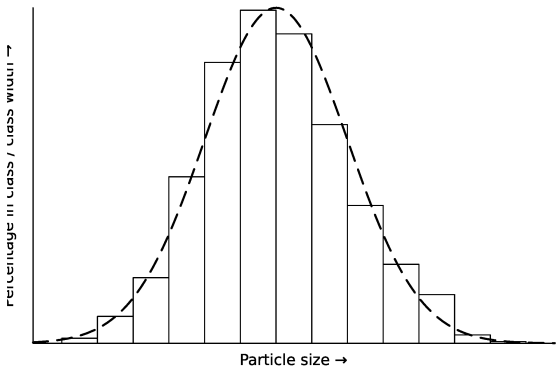

Figure 2.5: Graphical representation of particle size distribution through a relative percentage frequency distribution

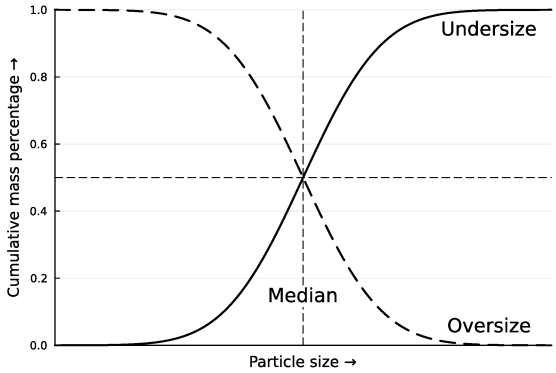

Figure 2.6: Graphical representation of particle size distribution through a cumulative percentage

Typical examples are the *equivalent volume diameter* d_v, defined as the diameter of a sphere with the same volume as the particle, while, for example, in other applications it might be better to consider the *equivalent surface diameter*.

Given a chosen particle size convention it is possible to proceed with the analysis of the size distribution using typical methods such as: sieve analysis [13], sedimentation and elutration, optical microscopy, Coulter counter [14], and laser diffraction spectrometry [15]. Once the size distribution is known, it is often useful to express this data as a histogram over the dimension classes where the area of each rectangle is proportional to the percentage of particles in that class size. It is then possible to obtain a smooth curve along the histogram that yield a frequency distribution of the classes, as can be seen in Figure 2.5. Another possible approach to the visual representation of the particle size distribution is the use of a cumulative plot, where particle size is plotted along the horizontal axis, while the vertical axis represents cumulative percentage undersize or oversize, as in Figure 2.6. This simple plot makes it possible to more reliably predict values not directly measured experimentally [12], and to read the *median size* directly, at the crossing between the two curves. This can prove to be useful since that dimension is one of the most commonly used to indicate the average size of the particles in a bulk solid, since it is one of the easiest to determine.

2.3.3 Particle shape

Another important characteristic of any bulk material is the shape of its constituent particles, since it has a significant influence on the packing and flow behavior of the material. The description of the shape of non-spherical particles proves to be quite difficult, so it is often relegated to a qualitative analysis categorizing the general shape of the particles as *acicular, flaky, nodular* and so on. Defining irregular shapes in mathematical terms is not easy, but one possible solution would be the use of *shape factors* indicating the extent to which particles differ from an ideal sphere.

One of the most commonly used shape factor is the *sphericity* Φ_s, which is defined be the ratio of the surface area of a sphere with the one of an irregular particle of the same volume:

$$\Phi_s = \frac{\text{surface area of a sphere}}{\text{surface area of a particle}} \qquad \text{of the same diameter} \tag{2.30}$$

The sphericity can be also linked to the volume and surface diameter, as defined in the previous Chapter, as follows:

$$\Phi_s = \frac{\pi d_v^2}{A_{sp}} = \left(\frac{d_v}{d_s}\right)^2 \tag{2.31}$$

where A_{sp} is the surface area of the particle. Knowing that Φ_s must be always less than unity, it is easy to conclude that the *volume diameter* d_v will always be smaller than the *surface diameter* d_s.

Clearly, experimental determination of sphericity requires knowledge of both the volume and surface area of the particle, which can both be quite challenging to measure. However, it is important to note that in the majority of storage and conveying applications, such detailed information on the shape of the particle is often not required. A more general knowledge of the shape is often sufficient for the design of such systems and is easily obtained with a simple optical microscope analysis. If the particles appear fragile, it could indicate possible degradation of the material during transport; a fibrous appearance may indicate a tendency for the particles to clump together during transport, causing flow problems; while the presence of sharp particles may warn of the possibility of high wear damage to various components in contact with them.

2.3.4 Cohesion and adhesion

One of the most common qualitative terms used to describe the behavior of a moving bulk solid is its *flowability*, a generic term used to indicate whether one of these materials is free-flowing or cohesive. This behavior can be influenced by a number of different effects but it's mainly due to the effect of attraction forces, or *cohesion forces*, between the constituent particles. These forces can have numerous different origins, such as moisture, electrostatic charging, magnetism, shape of the particles ecc [16]. When these attraction forces are low, the bulk material can flow easily, with the particles moving freely with respect to one another but, in the case of high cohesive forces, the particles tend to aggregate forming bigger lumps generating an erratic flow behavior [17]. Quantitative analysis of cohesion in bulk solids are made through the use of shear cell, where the shear resistance of a sample of bulk solid at zero compressive normal stress is measured [12] [18].

Another important aspect of the flowability of bulk solids is the interaction between them and a fixed boundary surface on which they slide. In this kind of situations the *adhesion* is the main parameter controlling the flowability of the material. While cohesion describes the inter-particle forces, adhesion is defined in terms of the forces that make the particles stick to some kind of containing surface, such as hoppers or channels' walls and can be measured with similar means as cohesion [18].

Angle of repose

A measurement that is often used to give a first indication of the flow behavior of a bulk solid is the so called *angle of repose*. This angle is observable when a certain sample quantity of a bulk material is poured, or let to slip, as to form a heap. The angle of repose is the angle of the natural slope of the free surface of a bulk solid heap, produced with specified test procedure, and can be considered a property of the material itself [12]. The value of the angle of repose is dependent on both the nature of the bulk solid and the way the heap is formed but, using a set of standardized tests, it is possible to obtain reasonably consistent values for a given sample material.

While the angle of repose can not be directly used as a quantitative measure of the flowability of a bulk material, it can prove to be a crude evidence of its likely flow behavior, as presented in Table 2.2 from Woodcock and Mason [12].

Table 2.2: Qualitative relationship between angle of repose and flowability of a bulk solid

Angle of repose	
25-30°	Very free-flowing
30-38°	Free-flowing
38-45°	Fair flowing
45-55°	Cohesive
>55°	Very cohesive

Arching

The cohesiveness of a bulk solid is a significant factor on the material's ability to form a stable *arch* or *bridge* over an opening. This phenomenon can be observed even when the opening is significantly larger than the particle size of the bulk solid. Hence, knowledge about the flow and arching behavior of bulk solids is crucial in designing storage containers and other components of bulk handling installations such as hoppers that must be able to discharge their contents smoothly under gravity without any obstruction to the flow.

The main factors that enable the phenomenon of arching to occur are the presence of very fine particles and moisture, both of which have the tendency to increase the cohesion of the bulk. Also the compaction that naturally happens during storage of this kind of materials helps to increase the cohesion between particles increasing the strength of eventual arches and thus aggravating the flow.

It is possible to distinguish two forms of stable arch that can be observed in bulk solids handling: the first one is a simple *mechanical arch* that develops when particles with a size comparable to the one of the opening interlock with each other, while the second is a *cohesive arch* that results from consolidation and cohesion of the bulk solid, and is typical of materials with very fine particle size [19]. An example of these two types of arches can be seen in Figure 2.7, where the case of arching in a hopper was considered. While the former case can be easily solved by using a bigger opening that is at least ten times larger than the size of the largest particle size [12], the latter has proven much more difficult to model and predict, making the design of hoppers and conveyors for this kind of applications more challenging.

2.3.5 Moisture content

As previously highlighted, bulk materials are characterized by the presence of empty space between the particles that constitute the bulk. These voids make it possible for water and other fluids to enter the volume of the bulk and interact with the particles changing the overall behavior of the materials. The moisture content can produce drastic changes on the flow behavior of bulk solids, in addition to other effects such as chemical reaction, deterioration of material qualities and so on [20][21]. Therefore moisture analysis represents one of the most frequently performed tasks in the characterization of this class of materials.

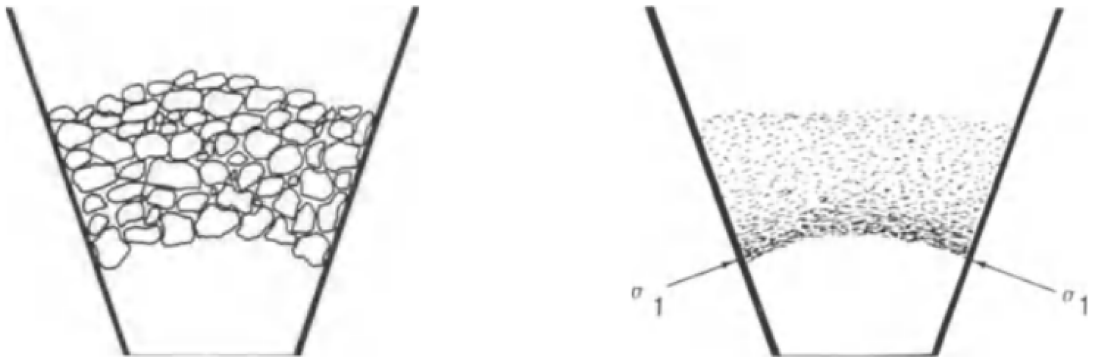

Figure 2.7: Arching phenomena in hoppers: on the left a mechanical arch, on the right a cohesive arch - from Woodcock and Mason 1988 [12]

The moisture content is typically expressed in terms of the mass percentage of water to dry solids:

$$\text{moisture content} = \frac{\text{mass of water}}{\text{mass of dry solids}} \times 100\,\% \tag{2.32}$$

while another possible definition is the moisture content in terms of mass percentage of water to wet solids:

$$\text{moisture content} = \frac{\text{mass of water}}{\text{total mass of solids and water}} \times 100\,\% \tag{2.33}$$

The measurement of the moisture content proves to be quite simple: first a representative sample of the bulk material is weighted, then the sample is placed in an oven for a certain amount of time. The sample is heated up using microwaves or infrared light for a certain amount of time as to make it dry completely and is then weighted again. The difference in the mass of the sample before and after the drying process should correspond to the water mass that was originally present in the sample.

$$\text{moisture content} = \frac{\text{initial mass of the sample} - \text{final mass of the sample}}{\text{final mass of the sample}} \times 100\,\% \tag{2.34}$$

Oven-drying has the disadvantage of being a lengthy process that usually takes several hours to complete so other faster methods has been used in different industrial and scientific settings, such as: measurements of infrared and microwave absorption [22], and nuclear magnetic resonance [23]. Another way of evaluating the moisture content in a material is the use of capacitive sensor that can offer high accuracy measurements by comparing measures from both the humid and dry sample, as demonstrated by Zabolotnyi and Koshevoi [24].

Moisture in bulk materials can be attributed to the presence of waters in mainly two different forms:

Surface moisture observed when water is present only on the surface of the particles and within the voids of the bulk

Inherent moisture which describes the presence of crystallized water within the structure of the particles composing the bulk solid

The moisture content can increase until when all the inter-particle voids are filled with water, the bulk material is thus said to be *saturated*.

Chapter 3

Vibratory Conveyors Technology

As mentioned earlier, this work is focused on expanding the knowledge of possible logistic solutions for local transportation of planetary and lunar regolith for In-Situ Resource Utilization (ISRU). The ISRU approach, applied in the sense of planetary exploration and colonization, involves the use of locally available resources as building materials or as sources of oxygen, metals, and other useful elements. In order to enable the full extraction and utilization of these materials, it is necessary to develop and deploy a reliable system for transporting these granular raw materials from the point of extraction to the required destination, which could also be located at a certain altitude with respect to the starting zone. Considering the constraints of lunar and planetary engineering, a vibratory conveyor, with its simple design and configuration, lack of moving parts, and low power consumption is a suitable solution for this kind of logistic problems. This type of transport technology presents a lot of interesting capabilities in terms of planetary ISRU. It can easily transport high-temperature or corrosive materials by using a trough specially designed for this kind of operations. At the same time it enables the use of actuators without moving parts that are, in this way, less subject to the strong abrasive power of lunar regolith. The next chapters will focus on a complete description of this type of material transport method with a strong focus on the design characteristics to be considered when designing this kind of system for planetary operations.

3.1 Vibratory conveyors

Vibratory conveyors are a logistical solution commonly used in industry to transport a wide variety of particulate and granular materials. When considering the goal of using this type of technology for *In-Situ Resource Utilizatio*n (ISRU) on the surface of other planets and moons, they become an interesting technology thanks to their simplicity and ease of control.

On a functional level, a vibratory conveyor consists of three main components: a trough dedicated to the transport of the material, a support system for the trough, usually consisting of springs or articulated links, which allows it to vibrate at a high frequency, and an appropriate excitation mechanism capable of generating the desired motion patterns. The trough is the part dedicated to holding and transporting the material. It can have different shapes that can modify the transport

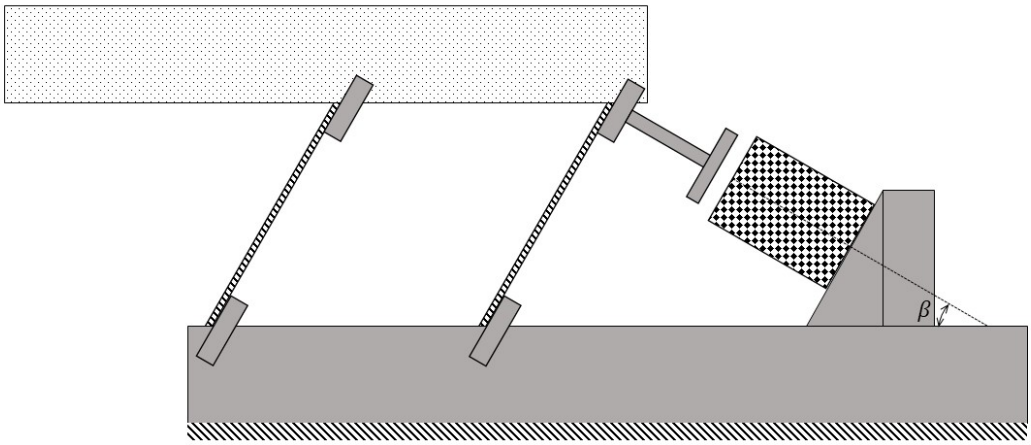

Figure 3.1: Conceptual sketch of a generic linear vibratory conveyor

behavior of the bulk, but it usually has a rounded or flat cross section and has the main objective of transmitting the motion from the actuator to the particles of the bulk material. Since the trough must be able to vibrate in order to generate the movement of the particles that make up the bulk material, it must be supported by some kind of flexible structure that, while connected to the conveyor's base, must provide the necessary mechanical flexibility to obtain an adequate transmission of motion from the actuator to the trough. This structure usually takes the form of simple springs, as in [25], or leaf springs made of thin metal plates, as in [26] and [27]. The active part of any vibratory conveyor is the actuator, that acts as a driving (or excitation) mechanism producing the vibration needed for the transport to happen. A conceptual sketch of the model can be seen in Figure 3.1 where all of the main features can be seen in their reciprocal relation. It is also possible to identify the angle β, defined between the actuator's excitation direction and the base of the conveyor, considered to be parallel to the transport track. This angle has a significant influence on transport speed, since it determines the force components, along x and y directions, to be transferred to the particles.

Since the widespread use of vibratory conveyors in various industrial settings, there are multiple ways to produce the vibration, with different technologies at play depending on the requirements for the conveyor [12][26]. The most common solutions can be seen in Figure 3.2. The actuation mechanisms can take the form of a standard electric motor as in 3.2a and 3.2b, or it can be done with electromagnetic coils as in 3.2c and, finally, with piezoelectric actuators, as in 3.2d.

3.1.1 Electric motor actuators

The more traditional types of excitation mechanisms use a standard electric motor attached to the conveyor structure. As can be seen in Figure 3.2a and 3.2b, the motor can generate the vibrations

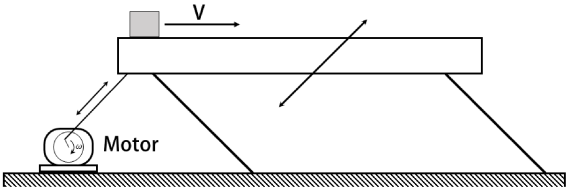

(a) Direct electric motor actuation

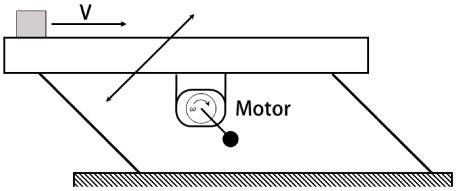

(b) Electric motor with eccentric mass

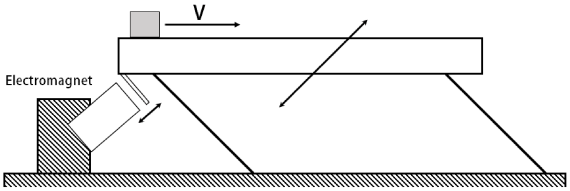

(c) Electromagnetic actuator

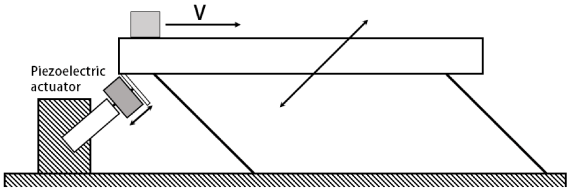

(d) Piezoelectric actuator

Figure 3.2: Different types of excitation mechanisms for vibratory conveyors. The arrows indicate the direction of motion

either through a *crank mechanism* or by spinning an *unbalanced mass*. These simple methods, while widely used in Earth conditions, present some shortcomings when used in a lunar environment. The high abrasive power of the lunar regolith will have a detrimental effect on the moving parts used for this solution, requiring frequent maintenance interventions that may be difficult or even impossible in a planetary exploration mission.

3.1.2 Electromagnetic actuators

A first approach to solving the presence of moving parts would be to use electromagnetic actuators as the excitation mechanism. This type of actuator uses an alternating electromagnetic field, generated by AC powered coils, to generate the vibratory motion of the trough. This design ensures that there is no contact between the two parts of the electromagnets, one of which is mounted on the support frame and the other on the vibrating trough. Electromagnetic drives are usually designed to operate at the standard frequency of the electrical grid, 50 or 60 Hz, depending on the local standard, and thus operate at a frequency of 100 Hz to 120 Hz, given that each electrical cycle corresponds to two vibration pulses [12]. Contactless excitation has some nice advantages in terms of wear and maintenance, but this technology still has some serious shortcomings regarding its potential application in space exploration missions. The transport capabilities of a vibratory conveyor powered by this type of technology are limited by the magnitude of the excitation forces that can be generated by the electromagnets. To generate a force strong enough to move the entire conveyor trough with the material inside, it is necessary to use large and therefore heavy electromagnets, which cannot be made lighter due to their intrinsic manufacturing process. This can be a problem in space applications, where the mass of the systems plays a critical role in mission planning. In addition, as shown by Despotovic et al. [4][5], it can be difficult to accurately predict the motion generated by electromagnetic excitation because electromagnetic forces are the result of a nonlinear interaction between a metallic moving part and an electromagnetic field, making it difficult to design and implement precise and reliable control systems to be used for ISRU missions.

3.1.3 Piezoelectric actuators

One of the most recent technologies for the actuation of vibratory conveyors is based on the use of piezoelectric actuators. These mechanisms are able to convert electrical energy into mechanical energy based on the principle of piezoelectricity, a property of certain dielectric materials to physically deform when subjected to an electric field [28]. Compared to the more traditional actuation mechanisms previously discussed, a piezoelectric actuation system can provide some advantages when used for vibratory conveyors for ISRU:

- The technology offers a high degree of flexibility in terms waveform, amplitude, and frequency modulation of the excitation motion, all of which can be easily modified by changing the input voltage.

- The ability to generate vibration without any moving parts reduces the effects of wear from the highly abrasive lunar regolith, increasing reliability and reducing the need for frequent maintenance.

A piezoelectric actuator is therefore highly suitable for space applications because of its simple configuration, absence of frictional parts, and no requirement of a significant amount of power.

Furthermore these components are usually really small and lightweight, making them an ideal choice for this kind of applications. That is why a piezoelectric actuator was chosen as the actuation method for the development of this work. More information about piezoelectricity and piezoelectric actuators will be given in Chapter 3.2.

3.2 Piezoelectric Actuation

As mentioned above, a piezoelectric actuator is a type of actuator that converts electrical energy into mechanical energy based on the principle of piezoelectricity, which is the property of certain dielectric materials to physically deform in the presence of an electric field or, conversely, to produce a macroscopic change in their electric polarization when subjected to mechanical deformation. Given the bidirectionality of the piezoelectric effect, it is possible to exploit it for the design and construction of both sensors, which measure the mechanical deformation while providing an electrical current output, and actuators, which generate a physical deformation when subjected to an electrical current [29]. Typical examples of materials that exhibit this type of effect to some degree are: natural quartz crystals, semi-crystalline polyvinyldiene, poly-crystalline piezoceramics, bone, and even wood [28].

This effect is due to the spontaneous separation of charge within a particular crystal structure under the right conditions. This phenomenon is called *spontaneous polarization* and is caused by the displacement of electron clouds relative to their atomic centers. It is particularly visible in poly-crystalline ceramics, one of the most active piezoelectric materials [28], which consists of randomly oriented small crystallites. Each of these crystallites is then further divided into *domains*, which simply refers to small regions of the crystallites characterized by having the same dipole arrangement. Typically, the domains' dipoles are randomly oriented, resulting in a macroscopic lack of piezoelectric behavior. In order to get the ceramic to exhibit piezoelectric effect, it is first necessary to induce a *macroscopic polarization* of the material. This is done by subjecting the ceramic to a strong electric field that orients all the dipole domains in the same direction, as can be seen in Figure 3.3. Once polarized, the material will remain so until it is depolarized by the same process with an opposite charge or until it is exposed to a high temperature. This polarization process causes the material to permanently elongate in the direction of the polarization field, also called *polarization axis*, while causing it to contract in the transverse direction. When voltage is then applied to the polarized material in the direction of the polarization axis the piece experiences further elongation along the polar axis and a subsequent transverse contraction, as per the material's Poisson's ratio, instead, if an opposite voltage is applied, the piece will contract along its polarization axis and expand along its transverse direction. When the external voltage is removed the piece reverts back to its original polarized dimensions. This process is summarized in Figure 3.4, where the physical deformation caused by the piezoelectric effect is showed. The application of this materials for the production of vibrational actuators is straightforward, by applying an alternate current of given amplitude, frequency, and waveform, it is possible to cause the reciprocal expansion and contraction of the piezoelectric component along its polarization axis.

Piezoelectric transducers, which convert electrical energy to mechanical energy acting as a motor, can come in a wide variety of shapes and sizes with different characteristics in terms of force-displacement relationships, from really stiff transducers to highly compliant ones. The most common piezoelectric actuator is the *bending motor*. It is typically composed of two layers of

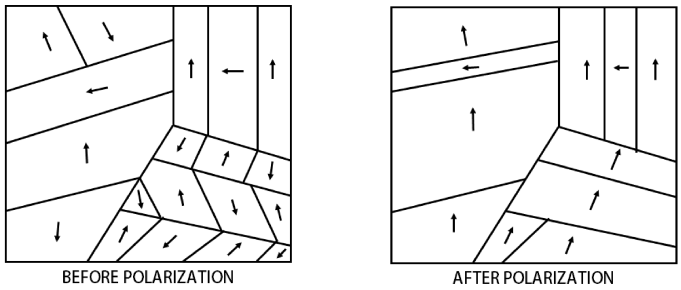

Figure 3.3: Polarization process for poly-crystalline piezoceramics. A strong magnetic field was used to align all the randomly oriented polar domains

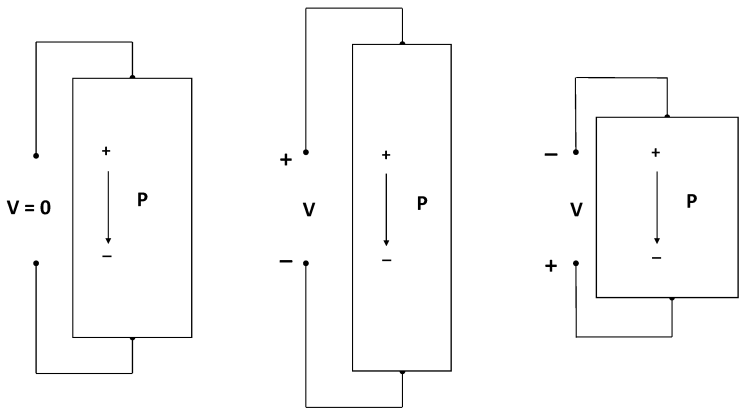

Figure 3.4: Example of physical deformation of a rectangular body made from piezoelectric material, with polarization $\boldsymbol{P}$, under the influence of different electric fields $\boldsymbol{V}$

piezoceramic that is then bonded to a thin metal shim sandwiched in the middle [28]. The application of voltage on the piezoelectric elements makes the whole component to behave like a bimetallic strip when subjected to heat. One layer expands while the other contracts resulting in a strong curvature of the component. A nice property of this kind of motors is that they can be energized proportionately to the desired curvature and can be held in that position with negligible consumption of energy and generation of heat. The combination of this simple components can be used to obtain different kind of actuation movement. Furthermore since piezoelectric actuators are solid state devices, they lend themselves to high vacuum operations making them an ideal choice for ISRU applications.

3.3 Movement of a bulk solid in a vibrating trough

This chapter presents a simple analytical procedure for theoretically estimating the average conveying velocity, and thus the mass flow rate, of a given material in a vibratory conveyor. The analysis presented here is based on the work of Woodcock and Mason [12], and Gaberson [30], who developed this approach for industrial application. Since the study and development of an analytical method is not the main scope of this thesis, this chapter aims to provide a brief overview of these methods to give the reader a basic understanding of the phenomenon of bulk solids transport. However, it is important to treat the results obtained with these analytical models with caution, as the extreme complexity of the bulk material evolution in a vibrating conveyor means that only limited confidence can be placed in such analysis. It will however prove to be useful as another method of comparison to be used in conjunction with both simulation and experimental data presented in the following sections.

3.3.1 Motion of the trough

The first step in studying the motion of the particles that make up the bulk material is to understand the motion of the trough in which the material resides. The most typical arrangement for the trough of a vibratory conveyor, and the one adopted in the experimental setup used in this thesis, is the *directionally constrained trough*, such as the ones shown in Figure 3.2. In this configuration, the trough can only move in a direction perpendicular to the springs that hold it to the base. The angle β formed by the *line of motion* s_T and the horizontal is called the *angle of oscillation* or *drive angle* [12]. This angle has a really strong influence on the transport capabilities of the setup, since it determines the force components to be transmitted to the particles along the x and y directions. For sinusoidal excitation it usually has a value in the range of 20-30°, since as demonstrated by Chen et al. [3], excitation parallel to the axis of the conveyor trough, corresponding to $\beta = 0°$, is only possible with non-sinusoidal vibrations (shocks) or with the help of a specially designed surface structure, such as a saw-tooth profile.

Since the trough follows a harmonic motion of frequency f and amplitude λ, the position and acceleration of the trough at a given time t can be expressed as

$$s_T = \lambda(1 - \cos 2\pi f t) \tag{3.1}$$

$$\ddot{s}_T = \frac{d^2 s_T}{dt^2} = \lambda(2\pi f)^2 \cos(2\pi f t) \tag{3.2}$$

It is now possible to compute the horizontal and vertical displacement component of the trough by simply projecting s_T and $\ddot{s}_T$ along the x and y axis using the drive angle β. The position

components become then:

$$x_T = \lambda(1 - \cos(2\pi f t))\cos\beta \tag{3.3}$$
$$y_T = \lambda(1 - \cos(2\pi f t))\sin\beta \tag{3.4}$$

While the acceleration component along x and y will be equal to:

$$\ddot{x}_T = \lambda(2\pi f)^2\cos(2\pi f t)\cos\beta \tag{3.5}$$
$$\ddot{y}_T = \lambda(2\pi f)^2\cos(2\pi f t)\sin\beta \tag{3.6}$$

The bulk material that is conveyed on the trough will lift off the surface the moment when the acceleration of the trough, in the downward vertical direction, becomes equal to the gravitational acceleration g. By imposing $\ddot{y}_T = -g$ it is possible to use Equation 3.6 to compute the lift off time t_1:

$$t_1 = \frac{1}{2\pi f}\cos^-1\left[\frac{-g}{\lambda(2\pi f)^2\sin\beta}\right] \tag{3.7}$$

Once the particles are in the air they will follow a parabolic trajectory until the next impact point, where the cycle will repeat with the particles being carried forward and upward before being thrown again as the trough decelerates along its harmonic cycle. This form of transport, the one where the particles are launched in the air along the transport direction before falling back to the trough, is called *oblique hopping* or *micro throw*, and is characterized by a really small contact time between particles and the trough's surface. In order to achieve maximum efficiency in the operation of the conveyor, it is essential to ensure that particles do not move backward during any part of the cycle. To achieve this, the impact point should align with the beginning of the subsequent flight phase.

It is now clear the importance of the ratio between the vertical acceleration of the trough and the gravitational acceleration of the environment on which the conveyor is working for the modeling of this mechanisms. The maximum value of this parameter in a given motion cycle is called *dynamic material coefficient* or, more simply, *throw factor*:

$$\Gamma = \frac{\ddot{y}_{T,max}}{g} = \frac{\lambda(2\pi f)^2\sin\beta}{g} \tag{3.8}$$

It's easy to see that at the start of the flight phase, as defined previously, $y_T/g = -1$ thus, if the maximum positive value of Γ is less than one, the bulk solid will not leave the surface of the conveyor's trough resulting in limited forward motion. By substituting the definition of the throw factor into Equation 3.7 it is possible to express the time at which the flight phase begins as a function of Γ:

$$t_1 = \frac{1}{2\pi f}\cos^{-1}\frac{1}{\Gamma} \tag{3.9}$$

Once the start of the flight phase is known, the next problem becomes the determination of the time of impact, at which the particles goes back in contact with the trough. This second part of the problem is definitely more difficult and must be considered as an important part of the conveyor tuning process, as to maximize the efficiency of the transport process. In general the conveyor's vibration pattern must be designed to match the particle's trajectories with the vibration of the trough itself.

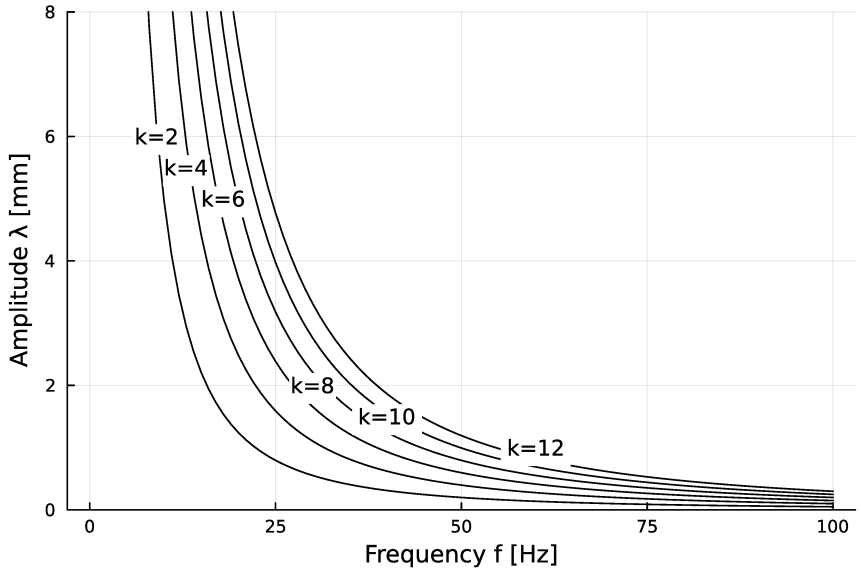

Figure 3.5: Relationship between amplitude, frequency and dynamic machine coefficient K

The other important parameters defining the motion of the trough are the frequency and amplitude of its vibration cycle. As a general consideration, the higher the frequency of the vibration motion, the smaller the amplitude must be [12]. It is possible to express this relationship by considering the ratio between the maximum trough acceleration and the gravitational acceleration:

$$\lambda = \frac{\ddot{s}_{T,max}}{(2\pi f)^2} = \frac{Kg}{(2\pi f)^2} \tag{3.10}$$

$$K = \frac{\ddot{s}_{T,max}}{g} = \frac{\Gamma}{\sin\beta} \tag{3.11}$$

Where K is often referred as the *dynamic machine coefficient*, or simply *machine number*. This relationship is expressed, for frequencies between 0 and 100 Hz, and for $g = 9.81\ m/s^2$, in Figure 3.5, where Equation 3.10 is plotted for different values of K. It is interesting to see how at high frequencies the influence of K becomes very small and all the different lines tend to converge to zero. This is due to the fact that in order to satisfy the condition necessary for the micro throw model, the maximum acceleration of the trough must be greater than g. Since the acceleration of the trough depends on both the amplitude λ and the frequency f^2, the influence of the frequency becomes increasingly important, hence the diminishing effect of K at high frequencies. In practical applications vibratory conveyors are usually designed to work with K between 1 and 4 but, for smaller units, the value of K can be as high as 12, since the inertial effects due to the structure being vibrated back and forth are less of a problem.

3.3.2 Motion of the bulk material in the trough

As previously explained, in the hypothesis of material transport through the micro-throw mode, the particles in the trough will lift off the surface once the downward acceleration of the trough exceeds the gravitational acceleration continuing their movement along what can be modeled as a parabolic trajectory. After a certain time the particle will come back down and impact the trough that will have moved too. The reciprocal position of the impact point between the particle and

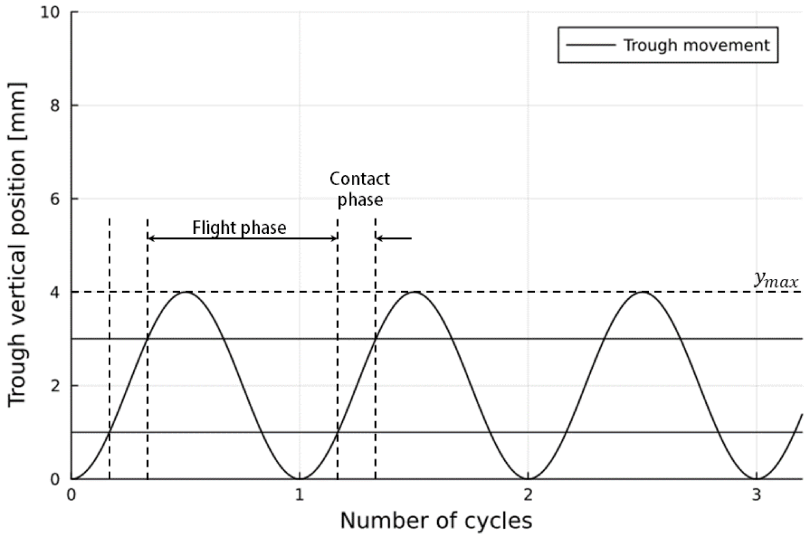

Figure 3.6: Description of the ideal motion of particles in a vibrating trough

the trough bottom surface can be adjusted by varying frequency and amplitude of the trough's oscillation. To make the conveyor operate at its maximum efficiency it will be necessary to ensure that the impact point occurs just before the lift off point of the next cycle, resulting in a short contact time, as can be seen in Figure 3.6. This small jumps are what enables the material to proceed along the trough at an almost steady horizontal velocity.

To further simplify the characterization of the vibratory conveyor setup it is useful to introduce a dimensionless parameter called *fligth ratio*, indicated by n, as the ratio between the time of flight and the period of the trough vibrations:

$$n = \frac{t_1 - t_2}{T_T} = \frac{T_F}{T_T} \tag{3.12}$$

By analyzing the particle trajectory it is possible to obtain an expression of the flight time T_F in terms of the vibrations amplitude, frequency and drive angle β. This relationship can then be further modified to include the effect of the dynamic material coefficient Γ and the flight ratio n, providing a high level design equation:

$$\Gamma = \left[\left(\frac{2\pi^2 n^2 + \cos(2\pi n) - 1}{2\pi n - \sin(2\pi n)} \right)^2 + 1 \right]^{1/2} \tag{3.13}$$

This equation has been plotted for n up to 3 in Figure 3.7, where it is easy to see how large values of n corresponds to large values of Γ. Remembering that the dynamic material coefficient Γ (see Equation 3.8) express the ratio between the maximum acceleration of the trough and the gravitational acceleration, it is clear that a high values of his coefficient means that the trough must be subject to high accelerations. Since the system must be built to withstand this kind of strains, some practical limits on the inertia effect must be taken into consideration. It is thus usual

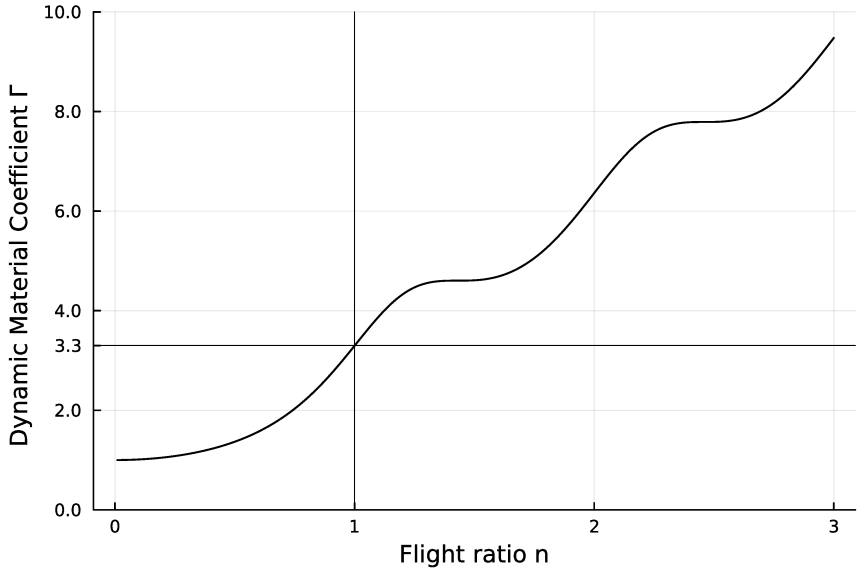

Figure 3.7: Relationship between the dynamic material coefficient Γ and flight ratio n, as expressed by Equation 3.13

practice to design and operate vibratory conveyors with a value of n less than unity. This means that the flight phase of the particles takes place within a single period of the trough vibration. From Figure 3.7 it is possible to see that imposing a maximum value of $n = 1$ corresponds to a practical upper limit on the dynamic material coefficient of $\Gamma = 3.3$. While $\Gamma = 3.3$ can be seen as the maximum practical value, in order to keep the inertia forces within acceptable limits it is common practice to design vibratory conveyors with Γ in the range of $1.5 - 2.0$ resulting in lower accelerations of the trough.

3.3.3 Average conveying velocity

Having presented the main parameters describing the operation regime of a vibratory conveyor, namely Γ, β and n, the main problem is now the determination of their optimal values as to guarantee the desired transport rate of a specified bulk material along the trough. Since all of the particle will move in different direction along a cycle, it is the *average conveying velocity* that is of interest for this type of analysis.

Starting from the trough movement, it is possible to express its horizontal displacement x_T and horizontal velocity $\dot{x}_T$ as:

$$x_T = \lambda(1 - \cos 2\pi f t)\cos\beta \tag{3.14}$$

$$\dot{x}_T = \lambda 2\pi f \sin(2\pi f t)\cos\beta \tag{3.15}$$

From the velocity equation it is easy to to obtain the maximum horizontal velocity of the trough as:

$$\dot{x}_{T,max} = \lambda 2\pi f \cos\beta \tag{3.16}$$

The average transport velocity can be expressed in terms of this maximum as [12]:

$$u_s = \eta_u \dot{x}_{T,max} = \eta_u \lambda 2\pi f \cos\beta \tag{3.17}$$

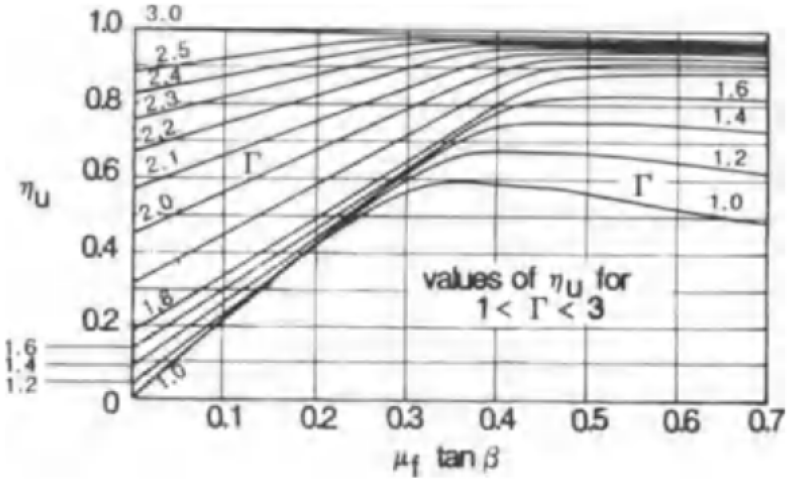

Figure 3.8: Values of transport efficiency η_u as a function of dynamic material coefficient Γ, drive angle β and coefficient of friction μ - from Woodcock and Mason [12]

where η_u is a coefficient that can be thought as an indicator of the "efficiency of transport", which is a function of the previously defined coefficients: the dynamic material coefficient Γ, the vibration angle β and the coefficient of friction μ between the bulk solid and the surface of the trough. The equation linking these different quantities together is very complex and is still subject of many open research topics. The efficiency of transport will furthermore depend on many other variables, such as the depth of the bulk layer, the inclinationα of the trough with respect to the horizontal, and the flow properties of the bulk solids being transported along the trough. These effects are usually taken into account with the use of empirical factors F_e, used to correct the "ideal" average transport velocity obtained with Equation 3.17. Figure 3.8, from Woodcock and Mason [12], presents a graphical way to determine the transport efficiency η_u to be used in Equation 3.17 to predict the transport velocity. It is important to note that, to use the graph, the coefficient of friction between particles and surfaces, the dynamic material factor and the drive angle, must be known for the examined case.

Putting everything together, it is possible to specify some ranges for the coefficient where the maximum average transport velocity usually lies. By linking the drive angle β and the dynamic material coefficient Γ, with usual values between 1.5 and 2.0, it is possible to obtain that the optimal β is usually in the range of 30° to 50° with a dynamic machine coefficient K in the range of 2 to 4. It is easy to understand how the angle of oscillation β will have e direct influence on the conveying velocity. Since it defines the angle of the force acting on the particles with respect to the horizontal, a small value of β will results in a low vertical acceleration imposed to the particles, resulting in little variation in friction between particle and trough. Using instead a high value of β will generate a small component of forward motion, resulting in a overall slower conveying speed.

The empirical factors, used to correct the predicted velocity, can be unified in a simple multiplying factor F_e that take into account:

- The different material characteristics, with a coefficient F_m that goes from 0.1 to 0.9 based

on the size distribution of the particles in the bulk material

- The depth of the bulk bed on the trough, with a coefficient F_h that varies from unity for small depth up to about 0.75 for depths of around 300 mm

- The slope of the trough, with a coefficient F_j that shows a values around unity for upward angles smaller than 15°, and then decreases rapidly with greater angles. For downward angles, F_j is greater than unity, reaching values of around 1.8 for a 15° downward slope. It is important to keep in mind that this parameter is greatly affected by friction between the bulk solid and the trough surfaces.

Given all of these considerations it is possible to express the transport velocity of the bulk solid on the trough with a new expression including all of empirical factors:

$$u_s = \eta_u F_m F_h F_j \lambda 2\pi f \cos\beta = \eta_u F_e \lambda 2\pi f \cos\beta \tag{3.18}$$

Once the transport velocity is known, the determination of the mass flow rate of the conveyor becomes trivial. It is sufficient to introduce the cross-sectional area A of the bulk material bed in the trough and its bulk density ρ_b, obtaining:

$$\dot{m}_s = \rho_b A u_s \tag{3.19}$$

Chapter 4

Numerical Simulation

In this section, the description of the DEM simulation code will be presented in detail. After an introduction explaining the importance of a simulation tool, the whole algorithm will be presented in great detail giving appropriate importance to the various aspects that come in to play while describing interactions between small solid particles. To help reduce the computation time required to complete the simulation a simple neighborhood algorithm was implemented producing a noticeable reduction in the computation time, given the same starting condition. An important section will be dedicated to the choice of an appropriate integration scheme used to evolve the simulation in time while also presenting a preliminary method to evaluate the integration time step needed to correctly compute all of the interactions.

4.1 Introduction

The creation of a digital twin of an experimental setup can be an important tool for researchers and engineers to test and optimize their designs before conducting expensive and time-consuming real-world experiments. In many cases, experimental setups can be complex and involve a range of variables that may be difficult to control or replicate. Thus, by creating an appropriate simulation tool, it is possible to simulate different scenarios and conditions in a controlled environment, allowing to explore the behavior of the system and identifying potential problems or areas for improvement. Furthermore, physical experiments are often constrained by the limitations of the experimental setup, so the use of a simulation setup can be particularly useful to simulate conditions that are impossible to create in a physical experiment, such as the one contemplated here, where the testing of a vibrational conveyor in lunar of martian environment is not yet possible. Given that the behavior of bulk materials is still an open research field, simulations offer an invaluable tool to study and understand this kind of discontinuous solids.

The simulation of discontinuous system such as bulk materials is a research area that has been in active development since the 70' with the progressive implementation of numerous different approaches. From the many numerical models available to simulate the behavior of these kind of systems, the Discrete Element Methods, chosen for this work, are characterized by having the following properties: they must allow finite displacements and rotations of discrete bodies, including a total detachment, and it must be able to recognize new contact automatically as the

simulation progresses [9]. In the case of the Distinct Element Method here presented, we refer to a particular implementation of those methods, which uses an explicit scheme to evolve the equations of motion of discrete bodies directly. This meshfree method finds a widespread application in various research topics such as rock mechanics, mining sciences, and the study of the stability of underground structures [9]. In this particular implementation the Distinct Element Model will be used to describe the mechanical behavior of an assembly of discs evolving inside of a virtual vibrational conveyor.

The whole simulation and data analysis algorithm was written in *Julia programming language* [31]. Julia is a high-performance and high-level programming language that is well-suited for scientific computing and simulation. Its Just-In-Time (JIT) compiler makes it fast, often comparable to or faster than statically-typed languages like C or Fortran while the simple, familiar syntax and large library of packages, including many specifically designed for scientific computing and simulation, make it accessible and easy to use for scientists and engineers. Julia also offers built-in support for GPU computing, making it possible to perform high-performance simulations resulting in significant performance gains or certain types of problems. It also offers straightforward parallel computing capabilities, making it easy to perform simulations in parallel on a single machine or across a cluster of machines thanks to its ability to automatically manage the shared memory. Additionally, Julia can easily interface with other programming languages, including C and Python, allowing for the leveraging of existing code and libraries. Given the ease of use, together with the speed, and the vast library of packages available, Julia was selected as the language of choice for the development of the simulation algorithm.

4.2 Simulation domain and particles

As for a lot of mechanical simulations, the Discrete Element Model is based on the simulation of physical bodies evolving inside of a well defined virtual domain, which represents the "world" in which the they are able to move and interact with each other. In order to accurately replicate real-world phenomena, it would seem logical for the simulation domain to be three-dimensional, mirroring the tridimensional reality in which the transport phenomena takes place. However, due to specific constraints that will be clarified shortly, this thesis work has opted for a two-dimensional simulation domain, which proves to be a more suitable choice in this particular application.

In particular, using a 2D simulation domain has a series of advantages for this kind of preliminary analysis tool. For one, the numerical implementation is generally easier, since there are fewer variables at play and less complex calculation, furthermore the collision's mechanics are much easier to analyze and implement due to the lower number of collision's modes. Moreover, 2D simulations are generally faster to run than their 3D counterpart, due to a lower number of particles needed, as will be explained in Chapter 5.2.1, making them a particularly useful instrument to quickly analyze large-scale systems. Running a 3D simulation can prove to be much more computationally intensive, and even small increases in the simulation domain size or particle number can significantly increase the total computational time required to complete the simulation. As for the results, Chapter 6 will show that the 2D simulation can provide a reasonable approximation of the physical behavior of the system studied, while allowing for faster simulation times than what would be offered by an equivalent 3D simulation model.

It is however important to note that reducing the number of dimensions from 3 to 2, introduces some important limitations. First of all the interactions between particles in a bidimensional domain are reduced. In particular, this type of simulation cannot capture certain physical phenomena that are inherently three-dimensional, such as rotations along the three axis or transversal movement of the particle on the trough. Furthermore there is one less dimension for the particle shape to evolve, limiting the shape description of the particles while, as said before, reducing the number of possible collisions and thus changing the overall energy distribution. It is therefore important to always consider the specific requirements of the simulation when choosing between a 2D and 3D domain. Given that this work will focus on developing a simple model for preliminary studies, a bidimensional simulation domain, calibrated and validated through the use of experimental data, is deemed acceptable.

As is common for this kind of DEM simulations, the interaction between the particles inside of the domain are purely mechanical, meaning that this model will not introduce long range forces such as electromagnetic effects due, for example, to tribocharging or to external fields. These kind of effects would still be easy to implement in the future, given the modularity of the produced code. Another simplification that is quite common in the field of Discrete Element Model simulations is the assumption of absence of air in the simulated domain. This make it so that the particles are free to move without any kind of aerodynamic drag and are not affected by air viscosity, humidity or other atmospheric effects. Even if there are available models that are able to simulate this kind of coupled phenomena, they are used for much more precise applications were even this small disturbances could have an important effect.

Following the same approach as before at simplifying the numerical model, all the simulated particles are assumed to be perfectly circular. This is an obvious simplification of the reality of all the naturally occurring bulk materials, since all of the particles composing this types of solids are characterized by at least some asphericity in their geometrical shape. As presented by Matuttis and Chen in their work "Understanding the Discrete Element Method" [32], this kind of assumption leads to peculiar particle's behavior, making it more difficult for the numerical model to be used as predictive tool. As it will be seen in the Chapter 6, this kind of simplification could be to blame for the higher discrepancies between simulation and experimental transport data that will be observed when studying the upward transport capabilities of the setup.

4.3 Calculation cycle

The DEM approach proposed in this work allows the description of the evolution of an assembly of discs of arbitrary dimension. The behavior is derived by computing and tracing the movements of every single particle over time, including their interactions with each other and with the boundaries of the simulation domain.

The heart of the whole system is the calculation cycle. Its purpose is to numerically and dynamically describe the state of every particle, and its evolution at each time step. The discrete element method, as it is described in this work, is based on the assumption that the time step chosen for the integration is so small that disturbances cannot propagate from any disc further than its immediate neighbors therefore, at each time step, the forces acting on any of the discs are determined exclusively by their interaction with the other disc with which it is in contact. These forces are used to compute the acceleration acting on the particles which is, in turn, employed

by the cinematic solver to compute the new positions of all of the particles at the next time step, evolving the simulation in time.

The most fundamental part of the whole simulation is the mechanical description of the interactions between different particles: the collision code. The numerical description of these interactions must be able to correctly describe the main characteristics of a collision between what are considered to be rigid bodies, which are:

- Elastic response
- Damping
- Friction

All of these mechanical interactions are modeled in the collision algorithm and will be described in the following chapters.

A big computational advantage of DEM is the fact that the deformation of individual particles is usually really small in comparison with the deformation of the whole granular assembly, since the total bulk deformation is due primarily to the relative movement of the single particles acting as rigid bodies [2]. This observation makes it clear how it is possible to completely neglect particle deformation in the simulation while still being able to obtain a good approximation of the macroscopic mechanical behavior of the bulk. Since all the simulated particles are assumed to be rigid bodies, their shape is considered to be invariant, removing the additional computational load that would be necessary to also compute this deformation. However, in the method, when a collision is observed, the two particles are allowed to overlap each other. The overlap in the simulation takes the place of the deformation observed in real particles. The magnitude of the overlap is then used as the main collision descriptor to compute the elastic forces acting on the particles as a response to the collision. The use of a finite overlap prevents the need of detecting the point of contact in a "numerically exact" way, with the precision necessary for a ideal rigid body simulation, while at the same time enabling the use of a rigid body set of coordinates, comprised of only a few kinematic variables.

4.3.1 Force-Displacement Law

To model the physical interactions between different particles and with the walls, the work by Cundall and Strack [2] makes use of a *force-displacement law* computed only at contact points. As the name implies, the force-displacement law is used to compute the forces on the particles, generated by the collision, using their respective positions and velocities as input. In this chapter both the "linear law", proposed initially in Cundall and Strack [2], and its non-linear evolution will be presented. The basic construction is based on a simple spring-dashpot model modeled by a set of appropriate coefficients.

The linear law proposed by Cundall and Strack [2] is used to compute the forces acting between two discs in contact, called disc *1* and *2* in Figure 4.1, respectively of radius R_1 and R_2 and mass m_1 and m_2. The centers of the discs are indicated as $\vec{P}_1 = (x_1,\ y_1)$ and $\vec{P}_2 = (x_2,\ y_2)$ where x and y refer to the coordinate axis of a Cartesian system. The movement of the discs is described by

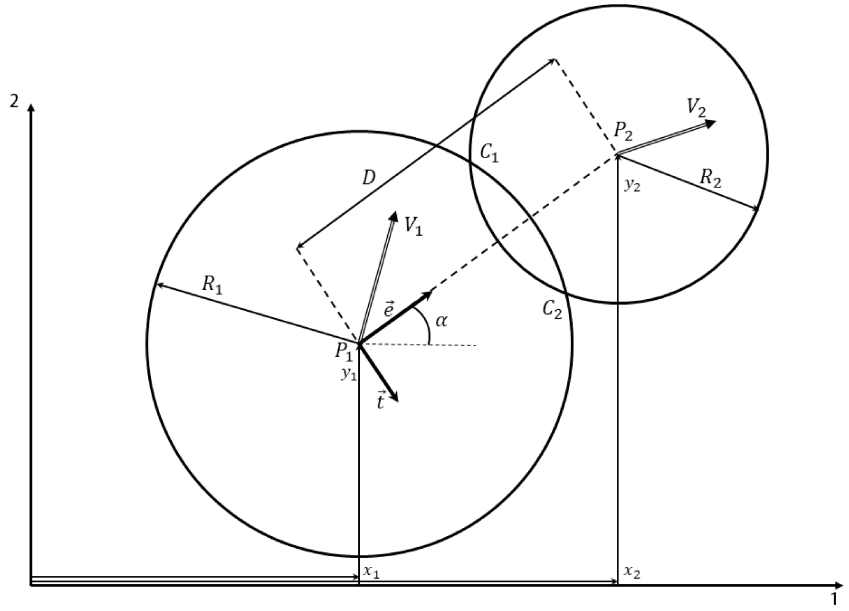

Figure 4.1: Interaction between two discs following Cundall's force-displacement law

the velocity vectors $V_1 = (\dot{x}_1,\ \dot{y}_1)$ and $V_2 = (\dot{x}_2,\ \dot{y}_2)$, while their angular velocities are indicated as $\dot{\theta}_1$ and $\dot{\theta}_2$.

The two particles can be considered in contact only if the distance $D = |\vec{P}_1 - \vec{P}_2|$ between their centers is less than the sum of their radii:

$$D = |\vec{P}_1 - \vec{P}_2| < R_1 + R_2 \tag{4.1}$$

If this condition is met, it is possible to evaluate the magnitude of the overlap between the two discs by means of a subtraction:

$$\Delta n = |D - (R_1 + R_2)| \tag{4.2}$$

If the two particles are colliding it is also possible to define a "collision line" that goes through the two intersection points C_1 and C_2 observed at the intersection between the boundaries of the discs.

It is useful to define the unit vector $\vec{e}$, pointing from the center of disc 1 to the one of disc 2, and its perpendicular unit vector $\vec{t}$ as follows:

$$\vec{e} = \frac{\vec{P}_1 - \vec{P}_2}{D} = (\cos\alpha,\ \sin\alpha) \tag{4.3}$$

$$\vec{t} = (e_2,\ -e_1) \tag{4.4}$$

It is now possible to use this two newly defined unit vectors to compute the relative speed of the two discs in the normal and tangential directions with respect to the collision line. These relative speeds, indicated as $\dot{n}$ and $\dot{t}$ respectively, will be useful for the computation of damping

and friction.

$$\dot{V}_n = (\vec{V}_1 - \vec{V}_2) \cdot \vec{e} \tag{4.5}$$

$$\dot{V}_t = (\vec{V}_1 - \vec{V}_2) \cdot \vec{t} - (\dot{\theta}_1 R_1 + \dot{\theta}_2 R_2) \tag{4.6}$$

In the case of a perfectly elastic response, the forces acting on the two particles are only due to the *elastic coefficient* k_n. In the case of a linear force-displacement relation the normal force acting on particle 1 will be computed as follows:

$$\vec{F}_{1,n} = \vec{F}_e = k_n \Delta V_n \cdot \vec{e} \tag{4.7}$$

$$\vec{F}_{2,n} = -\vec{F}_1 \tag{4.8}$$

The force acting on particle 2 will be the same in magnitude but along the opposite direction as per Newton's third law. By adjusting the value of the elastic constant k_n it is possible to make the system response more or less "rigid". Meaning that an increase of the elastic constant will decrease both the penetration length and the contact time, while a lower value of the coefficient will result in bigger penetrations and longer contact times between particle and floor. As showed by Woodcock and Mason [12], for an increase of the elastic constant of two orders of magnitude, a reduction of penetration depth and contact of about one order of magnitude should be expected.

4.3.2 Friction

Another important mechanical interaction between different particles and with the walls of the simulation is friction. Since the coefficient of friction is of order 1, this phenomenon cannot be considered a small perturbation to the system and thus ignored, but must be modeled and simulated in all of the interactions. In a calibrated DEM simulation, a heap of particles should be able to be created on a flat surface only thanks to the effect of friction between the particles and the floor since this is a typical behavior observed in granular materials in real life. Since there is currently no analytical computation method available for many-particle friction, it is necessary to use some kind of modelization to describe this phenomenon.

Just as for the elastic force computation, friction can be modeled using the model proposed by Cundall and Strack [2]. Assuming that the relative tangential speed v_t at the contact point is known, then the tangential force $\vec{F}_f$ can be incremented from the previous time step while there is still sliding:

$$\vec{F}_f(t) = \vec{F}_f(t - \tau) - \mu v_t \cdot \vec{t} \tag{4.9}$$

Where μ is the coefficient of friction and $\vec{t}$ is the tangential vector between the two colliding particles. To represent the real behavior of friction it is important to impose a limit on the total tangential force generated by friction, since it cannot exceed the total static friction, obtained as the product of the normal force with the static friction coefficient. If F_f happens to exceed this limit value, in a given time step, it will be truncated by the numerical model to $\mu_S \|\vec{F}_n\|$:

$$\vec{F}_f(t) = \text{sgn}(\vec{F}_f(t)) \cdot \mu_s \|\vec{F}_n\| \quad \text{if} \quad \|\vec{F}_f\| > \mu_s \|\vec{F}_n\| \tag{4.10}$$

As observed by Matuttis and Chen [32] the behavior of this model is oscillatory, as it behaves essentially as an harmonic oscillator. This poses a problem since it could happen that, due to the inertia of this fictional "harmonic oscillator", friction may act *in* the direction of the velocity of the

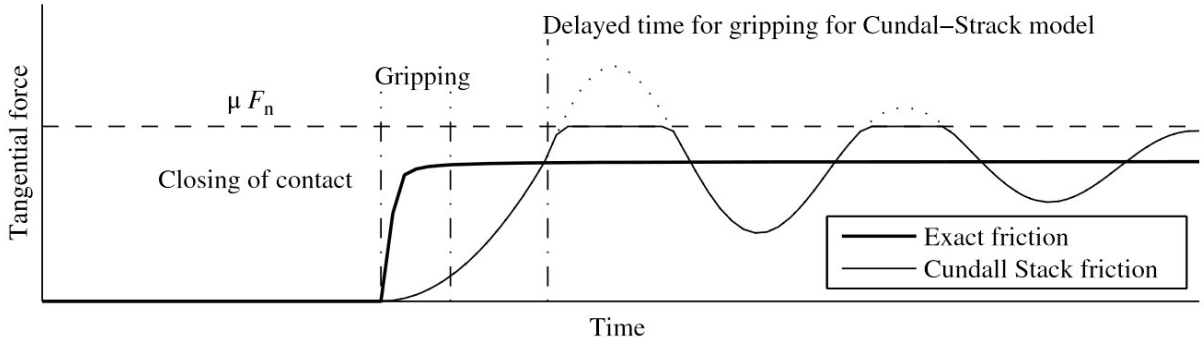

Figure 4.2: Static friction computed with the Cundall-Strack model against the behavior of exact friction. The gripping is delayed for the Cundall-Strack model - from Matuttis and Chen [32]

particles. To prevent this from happening, it is necessary to introduce a damping term also to the tangential forces with its magnitude proportional to the relative velocity. The mathematical description and implementation of damping in the code will be presented in the next chapters. The absence of this damping term has some intereeting side effects, as it causes the particle to accelerate along their direction of motion. In the presence of hundreds or thousands of particles interacting with each other this peculiar behavior might cause the whole simulation to become deeply unstable, with the whole set of particles just accelerating out of the simulation's boundary in an explosion-like evolution.

But, as it is known, while the damping effect in an oscillator might help to reduce the oscillations it also introduces a certain amount of delay between the excitation and the response of the system. This phenomenon can be observed in Figure 4.2, taken from the work of Matuttis and Chen "Understanding the Discrete Element Method" [32], where it can be seen how the modeled friction acts with a sliht delay when compared to the ideal "exact friction" model. Nevertheless, going beyond the time scale of these little oscillations, the results obtained by using the Cundall-Strack model are overall satisfying.

The introduction of friction makes the presence of tangential forces possible. In turn, these forces causes the particles to turn around their center which makes it essential to introduce another kind of friction in the model: *rolling friction*.

4.3.3 Rolling Friction

To accurately depict the behavior of rolling particles, it is essential to consider the influence of rolling friction. Rolling friction is a common phenomenon observed when objects are in a rolling motion. It is responsible for causing a rolling ball to gradually slow down and eventually come to a stop, even when the force of sliding friction between the ball and the surface is absent.

In the case of perfectly rigid bodies engaged in pure rolling, the relative velocity at the contact point between the particle and the surface is zero, resulting in zero sliding friction. However, in reality, rolling friction is observed due to the deformation of the material at the contact point. It is to say that rolling friction is a characteristic of elastic bodies [32] In DEM simulations, where the deformation of both the particle and the surface is not calculated, the action of rolling friction

can only be analytically modeled using parameters. This approach allows for the incorporation of rolling friction effects into the simulations, despite the absence of detailed deformation computations.

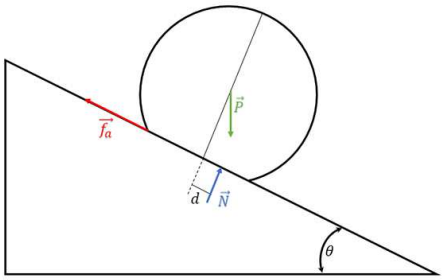

Figure 4.3: Force decomposition for a disc rolling down an incline with rolling friction. Disc's deformation is here emphasized for clarity

As presented in the work by Maslova et al. [33], the rolling friction effect due to the deformation of the material can be analytically described by the generation of a torque acting in the opposite direction to the rotational movement. The only way of generating this torque, for a ball rolling on a plane, is through a component of the surface reaction force that is acting orthogonally to the surface itself but is not directed to the center of mass of the particle. In this configuration the surface reaction force is applied at a distance d, with respect to the center of mass, along the direction of the translational motion resulting in the generation of torque. In the bidimensional case considered in this work, the shifted reaction force of a ball rolling down an incline can be decomposed in two components, as shown in Figure 4.3: one component that runs parallel to the surface and determines the effective static friction, and another component that runs orthogonal to the surface and represents the normal force.

Given that F_s is the effective static friction, d is the shift of the normal from the center of mass of the particle, R is the sphere's radius and $I = \gamma m R^2$ is the moment of inertia, it is possible to write the equations of motion of a rolling round particle as follows:

$$mg\sin\theta - f = ma \tag{4.11}$$

$$N = mg\cos\theta \tag{4.12}$$

$$-fR \pm Nd = -I\frac{a}{R} \tag{4.13}$$

where θ is the incline angle. The sign of the second term of Equation 4.13 should be positive in the case of a particle rolling downward, since the normal force gets shifted to the right of the center of mass, while it should be negative when the particle is rolling upward, given that the normal force is shifted to the left of the center of mass.

By means of substitution it is then easy to obtain that:

$$f = -\frac{\gamma mg}{\gamma+1}\sin\theta \mp \frac{1}{(\gamma+1)}\frac{d}{R}mg\cos\theta \tag{4.14}$$

$$a = \frac{g}{\gamma+1}\sin\theta \mp \frac{1}{(\gamma+1)}\frac{d}{R}g\cos\theta \tag{4.15}$$

Where it is possible to isolate the *rolling friction coefficient* μ_R that will be equal to:

$$\mu_R = \frac{1}{\gamma+1}\frac{d}{R} \tag{4.16}$$

It is interesting to note that the coefficient of rolling friction does not depend on the inclined plane's angle. This is in accordance with the findings of various authors who, validated by experimental results, concluded that for small angles and velocities the rolling friction coefficient should remain constant, such as Cross [34], Mungan [35], and Doménech et al. [36].

As will be shown in Chapter 5.2, a simple experiment was carried out to estimate the rolling friction coefficient μ_R of the glass particles used in the transport experiments. From this data it was possible to obtain a value of μ_R to be used in the computation cycle where, firstly, the displacement d is computed using the known radius of the particle and then, in the next step, the rolling friction torque is determined as follows:

$$d = \mu_R(1+\gamma)R \tag{4.17}$$

$$M_R = -|F_n|\,\mathrm{sgn}(\dot{\theta})d \tag{4.18}$$

where F_n is the normal reaction force between the surface and the particle and $\dot{\theta}$ is the rotational speed of the particle. The same approach is used in the case of two colliding particles, but $\dot{\theta}$ will simply become the relative rotational speed and F_n the elastic force between the two. The computed torque M_R is then added to the total torque acting on that particular particle, and the total is then used for the motion computation, which will be presented in Section 4.3.5.

4.3.4 Damping

When attempting to depict the behavior of real materials, a basic elastic collision response falls short, as collisions between real materials typically involve a dampened response, even under ideal conditions. In such collisions, a portion of the kinetic energy is inevitably dissipated as heat, sound, or plastic deformation of the objects involved. To account for this phenomenon, a "damping factor" D is introduced into the force-displacement relationship.

In the context of linear force-displacement laws, the damping force is directly proportional to the relative velocity in both the normal and tangential directions.

$$F_{D,n} = -D_n\dot{n}\cdot\vec{e} \tag{4.19}$$

$$F_{D,t} = -D_s\dot{t}\cdot\vec{t} \tag{4.20}$$

Where D_n and D_s represent the damping factor in the normal and tangential directions respectively. It is possible to sum this newly computed *damping force* to all the other forces acting on the particle to obtain the final equation of the force. This equation, comprising all the different

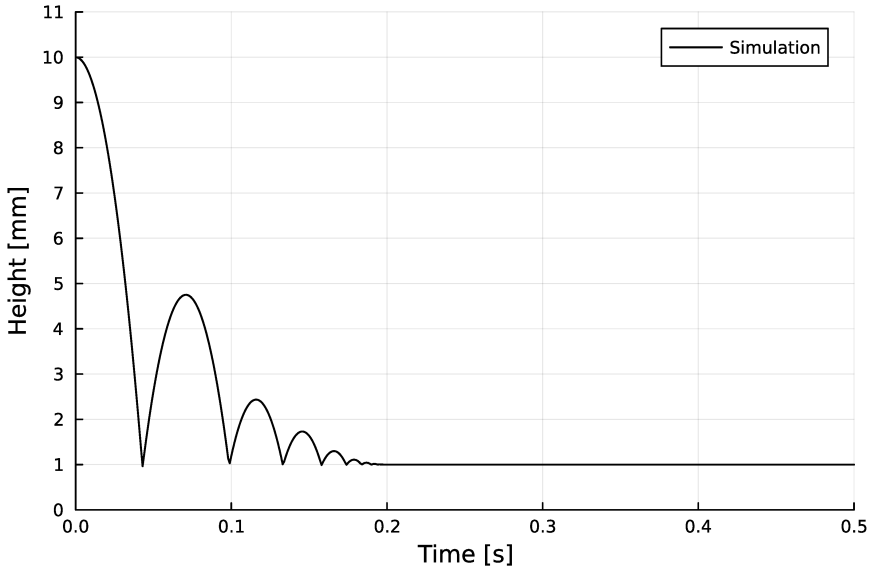

Figure 4.4: Bouncing ball simulation with damping, the maximum altitude gets reduced at each bounce

actions, will contain the elastic response F_E, the friction F_f and damping F_D, both in the normal n and tangential t directions with respect to the collision plane:

$$\vec{F}_n = \vec{F}_{E,n} - \vec{F}_{f,n} - \vec{F}_{D,n} \tag{4.21}$$

$$\vec{F}_t = \vec{F}_{E,t} - \vec{F}_{f,t} - \vec{F}_{D,t} \tag{4.22}$$

The results of the application of this law can be seen in Figure 4.4 where a single ball bouncing on a virtual floor placed at $y = 0$ is simulated. As can be easily seen the amplitude of each bounce is progressively decreasing due to the effect of damping.

It must however be noted that a straightforward implementation of the numerical description of damping as proposed in the previous paragraph presents an important problem regarding the integration time step during the approach and separation from contact. As can be seen from Figure 4.5 the force response to a dampened collision between two particles turns out to be *non-smooth*. If the elastic force can be assumed to take a sine-like shape from 0 to π, then the damping response will correspond to a cosine-like wave on the same interval presenting a jump both at approach and separation. Both of these jumps are not present in the simple linear elastic response, where the progressive approach phase guarantees a smooth evolution of the force. For dry granular materials, as the ones used in this work, we have to impose that the forces be only repulsive or zero since it would be nonphysical to accept a cohesion effect that is due to damping. While the jump in the total force at the approach can be somewhat justified as impacts are non-smooth phenomenons that dissipate energy through the generation of sound, heat and damage at the surface, the attractive force at separation resulting from the algebraic sum of elastic and damping forces, visible in Figure 4.5(a), is completely nonphysical and must be eliminated. The resulting jump in the force requires really small time steps to keep the integrator from diverging and the allowing of this kind of nonphysical behavior could cause "explosions" in particle clusters where multiple contact can be observed and there is a high probability of an unfavorable separation between two particles.

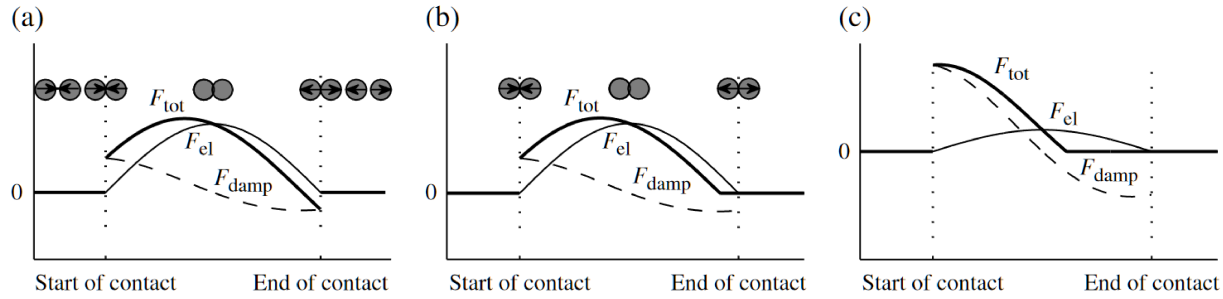

Figure 4.5: Force evolution for an elastic force with velocity-proportional damping: (a) direct addition of the elastic force (with sine-like time evolution) and the damping (with cosine-like time evolution); (b) regularization to avoid spurious cohesive (attractive) behavior at separation; (c) the force resulting from too-large impact velocities, which is difficult to integrate numerically - from Matuttis and Chen [32])

This "exploding" behavior is due to the generation of the aforementioned nonphysical attraction force where the two colliding particles instead of bouncing away from each other start to be attracted to each other. This attraction causes the overlap between the particles to progressively increase until the elastic force overcomes the damping. Once this critical threshold is reached the two particles start accelerating away from each other at high speed causing the whole simulation to diverge.

An easy way to eliminate the jump in total force during separation is to ensure that when damping is added to the elastic force it does not change the overall sign of the force. This can be accomplished by resetting the total force to zero in such cases [37]. This simple solution has been implemented in the simulation to both normal and tangential damping solving all the problems observed with "exploding" simulations since it completely removes the problem of spurious attraction. The application of this solution to the example proposed in the previous paragraph is visible in Figure 4.5 (b): during separation the total force is set to 0 when the damping would have made it negative in sign.

The evaluation of the damping factor D is not straightforward and is often relegated to the use of empirical formulas developed by different authors for various situations. An example of this formulation is the one proposed by Ting and Corkum [38] and by Ting et al. [8], based on the mass of the particles, the normal elastic coefficient, and the so called *coefficient of restitution* e:

$$C_n = -2\ln(e)\sqrt{\frac{k_n m}{\ln^2 e + \pi^2}} \tag{4.23}$$

This particular formulation was chosen for this thesis work being particularly suited to spherical collisions. The coefficient of restitution, often denoted by e, is defined as the ratio of the final and initial relative speed between two objects after their collision:

$$e = \frac{|v_b - v_a|}{|u_a - u_b|} \tag{4.24}$$

In the equation u and v are the speed of the two objects and the subscripts a and b denotes the speed before and after the collision respectively. This parameter typically varies from 0 to 1,

where $e = 1$ would indicate a perfectly elastic collision, but it can take values higher than one in the case of an energy gain during the collision from a chemical reaction or a reduction in rotational energy. In general, the coefficient of restitution is to be intended as a property of a *pair* of objects in a collision, not of a single one, and presents dependence on particle materials, angle of collision and impact speed, being really difficult to characterize in a standardized manner [39] [40].

If nonlinear powers of the penetration depth are instead considered, the overall picture of the discussion remains unchanged. Many studies make use of the Hertzian force law ($\propto x^{3/2}$) and the corresponding Kuwabara–Kono force law ($\propto v^{3/2}$) for damping [41], however, if these forces are added together without proper precautions, the same problem in the damping computation discussed earlier will occur.

4.3.5 Motion computation

The last step in the calculation cycle is the computation of the motion of all the particles during that time step caused by the forces computed in the previous steps. The end result will be the position of all the particles to be used in the force-displacement law on the next time step.

The computation of the motion is pretty straightforward and is made using Newton's second law of motion. Considering disc i on which are acting a certain number of forces F_j and torques M_j it is possible to express the following laws of motion:

$$m_i \ddot{x}_i = \Sigma \vec{F} \tag{4.25a}$$

$$I_i \ddot{\theta}_i = \Sigma \vec{M} \tag{4.25b}$$

Where m_i and I_i represent respectively the mass and the inertia of disc i. Keeping the assumption of $\ddot{x}_i$ and $\ddot{\theta}_i$ constant over a single time step Δt it is possible to rewrite Equations 4.25a and 4.25b to obtain the linear and rotational accelerations:

$$\ddot{x}_i = \frac{\Sigma \vec{F}}{m_i} \tag{4.26}$$

$$\ddot{\theta}_i = \frac{\Sigma \vec{M}}{I_i} \tag{4.27}$$

To consider the influence of gravitation force a term $m_i \ g$ is included in the force sum ΣF_i in Equation 4.26. The term $g = (g_x, g_y)$ represents the components of the gravitational acceleration vector with respect to the chosen coordinate axis of reference. The computed acceleration are then used by the chosen integrator to compute position and velocities at the subsequent time step.

4.3.6 Nearest Neighbors Algorithm

Building upon the force-displacement law explanation presented in Chapter 4.3.1, it becomes evident that the entire physical interaction algorithm relies on knowledge of the relative positions of the particles. In each calculation cycle, every particle needs to assess its position in relation to all other particles to determine if a collision has occurred. However, as the number of particles increases, this process becomes exponentially more demanding. Furthermore, since these calculations must be performed at every integration step, it significantly decreases the overall speed of the simulation. Given that the simulation will involve in the order of thousands of particles,

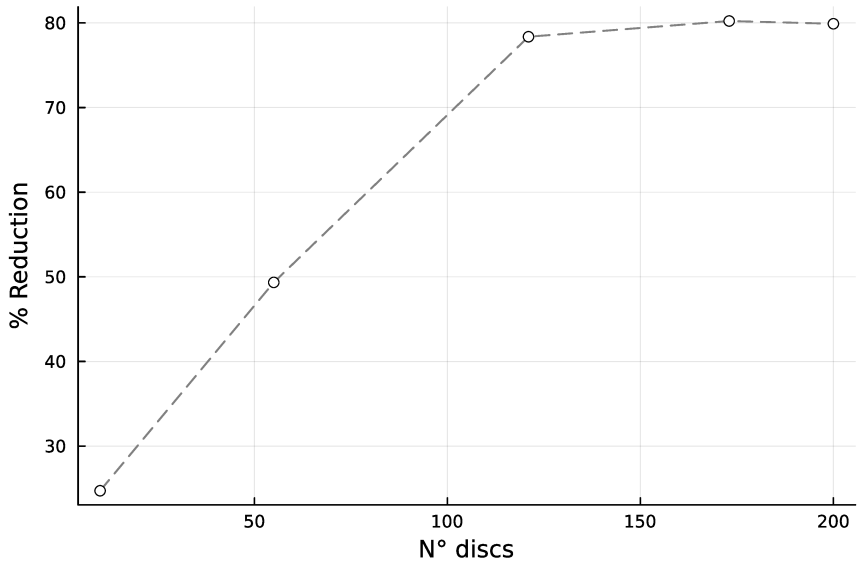

Figure 4.6: Percentual reduction of computational time with neighborhood algorithm

it becomes crucial to reduce the computational burden associated with these checks. This is why the introduction of an optimization algorithm was considered.

A naive implementation of a simple collision control code, for a simulation of N particles, would yield $N(N-1)$ possible interactions that must be computed and assessed every time step, since every particle must check its position against the one of all the others. A first step in the optimization process would be to consider Newton's third law, the "*action = reaction*" principle. It's easy to see that, given two particles i and j interacting with each other in a collision, the force F_{ji} created by the action of particle i on particle j will be the opposite of F_{ij}, the one generated by particle j on particle i, yielding $\vec{F}_{ji} = -\vec{F}_{ij}$. The interaction forces between two particles can then be computed only once and added, with different signs, to the respective force vectors. This small change introduces a factor of $1/2$ to the number of interactions but it doesn't lower the complexity order from the original $\boldsymbol{O}(N^2)$.

To further reduce the computational effort it is useful to remind that the DEM particles considered in this work can only interact with each other through mechanical contacts. It is reasonable to assume that in two dimensions there will hardly ever be more that 6 contacts on average so, theoretically, this should lower the complexity factor to a much more manageable $\boldsymbol{O}(3N)$ [32]. The methods that are used to reduce the number of comparisons needed for interaction description are generically called *Neighborhood Algorithms*. The main focus of these algorithms is the elimination of comparisons made between particles that cannot possibly overlap due to geometric constraints.

The Julia package *NearestNeighbors.jl* [42], developed by Kristoffer Carlsson, offers optimized implementation of different neighborhood algorithms, making it easy to add this kind of functionality to a preexisting problem formulation. The package offer a set of algorithms that can work on different metrics. Given the characteristics of the DEM simulation, composed of particles moving in a 2D euclidean space, the `KDTree` construction algorithm was chosen. This algorithm creates

a binary tree structure where the particles, defined by their position on the 2D plane, are recursively spit into different groups using hyper-planes [42]. By applying the function `inrange()` to the previously built particle tree, it is possible to obtain a list of all of the particles within a given range r from a given point. This procedure is made for all of the particles in the simulation thus obtaining a matrix composed by the IDs of all of the particles within a given range from all of the others.

The problem now becomes how to estimate an appropriate search range r given the distribution of different particles' dimensions inside of a generic simulation. A simple approach was followed in this regard: given the maximum particle radius present in a given simulation, the search range was be set to:

$$R_{search} = 2R_{max} + 0.4R_{max} = 2.4R_{max} \tag{4.28}$$

This radius ensures that the scanning area is big enough to include all of the possible colliding particles while being small enough to not impact the computation time. A series of tests was carried out to check for the validity of this choice and, given the chosen integration time step and the typical velocities of the particles, the algorithm managed to correctly detect and compute all of the collisions.

Furthermore a set of simulation was run to observe the effect of this optimization technique on the total number of comparisons carried out inside of a simulation and the total computation time by running the simulation on a single core for repeatability. The results can be seen in Figure 4.7, where it is obvious how the introduction of the neighborhood algorithm grants a large decrease in both number of comparisons and total simulation time. It is interesting also to see how this positive effect gets more and more prominent as the number of total particles in the simulation gets higher, as is to be expected given the differences in computational complexity between the original and the optimized algorithm. Another interesting result is presented in Figure 4.6 where the percentage reduction of computation time is plotted against the increasing number of discs in the simulation. The reduction increases rapidly with the number of discs up until around 120, where it settles to a reduction of around 80 % of the computational time. This is already a great results which, together with the multithreading capabilities of Julia, makes the simulation of a much higher number of particles possible in shorter time span.

4.3.7 Boundaries

As far as the simulation has been presented, the walls, or boundaries, of the simulation domain were often referred to without giving a clear explanation of their role in the computation cycle. The boundaries of the domain are defined as hard limits that surrounds the area in which the particles are free to move, making sure that no particle will just fly away from the central part of the simulation domain itself. In this particular case they define a rectangular central region described by four sides. The interaction between particles and walls are described in the same way as the interaction between two particles, with the use of a spring-dampener system as explained previously. In the case of the particle-wall interaction, however, the reaction forces are only applied to the colliding particle since the walls are considered to be unaffected by the collisions.

Apart from establishing the fixed boundaries of the simulation domain, it is also possible to introduce moving boundaries that can generate inputs within the simulation through their motion. This dynamic boundary feature proves to be particularly valuable in the context of the considered

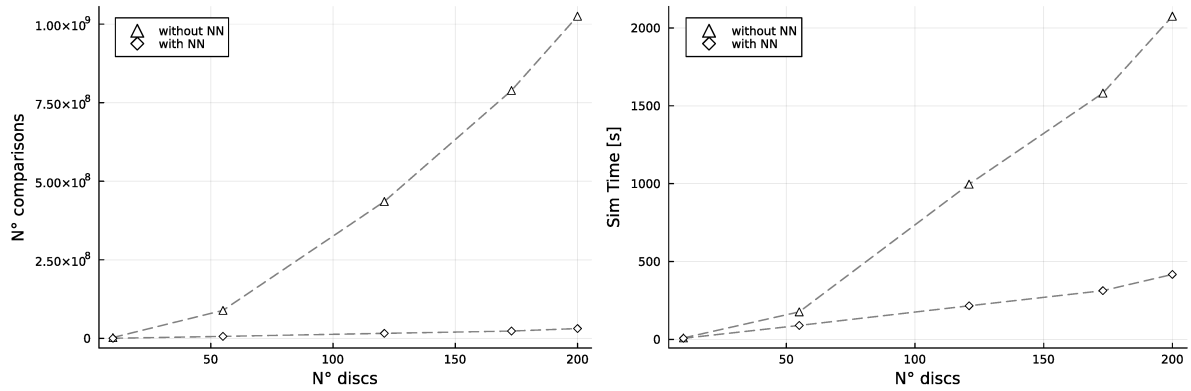

(a) Total number of comparisons

(b) Total simulation time

Figure 4.7: Total number of comparisons and simulation time obtained with and without neighborhood algorithm (NN) with different amounts of discs

case, as it enables the simulation of vibrations in a vibratory conveyor. By repeatedly moving the bottom boundary condition up and down, the simulation can emulate the vibratory motion. As a result, particles in contact with this bottom wall will experience forces generated by the movement of the boundary, and theoretically, they should initiate motion along the x-axis. The position over time of the bottom wall along the y-axis $y_B(t)$ is described as follows:

$$y_B(t) = A \cdot \cos(2\pi f t) \tag{4.29}$$

where A is the amplitude of the desired vibration in millimeters, f is the frequency in Hertz, and t is the time in seconds. By knowing the vibrational parameters of the real experiment it is possible to simulate the same conditions by imposing this boundary to the simulation domain.

4.4 Choice of integrator

Given that DEM simulations require the modeling of individual particles and their interaction with each other and with their surroundings over time, it is necessary to couple the impact model with an appropriate numerical integration scheme that deals with solving the equations of motions for every single particles at each time step. There are a number of different integrators available, and each one is suited for a particular set of problems, and the choice of an inappropriate method could lead to numerical artifacts such as energy drifts, which can cause the simulation to diverge.

It is important to note that, in numerical analysis, ordinary differential equations (ODEs) can be classified as either *stiff* or *non-stiff*. This classification is based on the behavior of the solution of the ODE and the properties of the numerical methods used to solve them. A non-stiff ODE is one where the solution varies slowly and smoothly over time. In other words, the rate of change of the solution is relatively constant and does not change abruptly. Numerical methods for non-stiff ODEs can be simple and efficient, and generally, do not require a small time step to obtain accurate results. On the other hand, a stiff ODE is one where the solution varies rapidly and changes abruptly over time. In other words, the rate of change of the solution can vary greatly,

and the solution can exhibit sharp peaks or valleys. Numerical methods for stiff ODEs need to be carefully designed, and often require a small time step to obtain accurate results.

Based on the work by Kruggel-Emden et al. [43], it was decided to proceed with an explicit numerical integration scheme for their good performances within the discrete element method. Referencing to the documentation of the high number of integration schemes available in the `DifferentialEquations.jl` Julia package, it was decided to implement the `AutoTsit5()` algorithm. This particular implementation of the Runge-Kutta 5/4 order algorithm, based on the work by Tsitouras [44], has the ability to handle both stiff and non-stiff differential equations with a special auto-switching algorithm. According to the documentation this kind of solvers allow for efficient solution of both this types of problems with minimal added computational cost when compared with more "classic" integration schemes.

The chosen integrator was compared to two other common integration schemes, the normal `Tsit5()` and the `Vern7()`. When simulating the simple case of a ball bouncing in a perfectly elastic manner on the floor by imposing the same absolute and relative tolerance and the same integration timestep, it was noted that the `AutoTsit5()` provided similar results, with maximum energy variation lower than 1 %, with a computation time about 5 to 10 % lower than the other two methods. This difference could be explained by the ability of the integrator to better handle the impacts since they are described by discontinuous events that could prove to be difficult to numerically describe for pure non-stiff solvers.

4.4.1 Determination of integration time step

Another important aspect of the integration process and thus, of the whole simulation, is the choice of an appropriate *timestep* for the integrator. This parameter can significantly influence the accuracy and stability of the simulation results. The timestep represent the size of the *discrete time steps* that are used to numerically integrate the equations of motion that describes the evolution of the simulated system over time.

Its importance is reflected in 3 main aspects of the solution process:

Accuracy The choice of a too large timestep can lead to inaccurate simulation results since the integrator may miss important dynamic changes or collisions that might occur during that time interval. Conversely, a too small of a timestep will cause unnecessarily long simulation times and an high computational expense.

Stability The stability of the whole solution process is also strongly influenced by the chosen timestep. A large timestep could lead to unstable simulations due to accumulated numerical errors and divergent results. At the same time using a smaller timestep could help improve the stability of the simulation.

Computational Efficiency It is easy to see how the timestep is directly linked to the computational efficiency of the whole simulation process. By using a smaller timestep the time needed to complete the simulation will increase drastically, whereas using a larger timestep length can help reduce the computational cost but, as said before, could result in less accurate or unstable results.

The problem of the choice of the right timestep is shared between all the numerical solution schemes and must be solved by trying to find a balance between these 3 aspects. It is often necessary to perform some kind of sensitivity analysis to determine the optimal timestep for a particular simulation scenario.

To get a rough idea of the timestep to be used in DEM simulation, it is useful to refer to the *critical timestep* Δt_c as defined in the original paper by Cundall and Strack [2]. This critical time step is estimated using the single degree of freedom system composed by a mass m that is connected to the ground by a spring of stiffness k. For this type of system the critical time step is equal to:

$$\Delta t_c = 2\sqrt{\frac{m}{k}} \tag{4.30}$$

Where the mass m is the mass of the smallest particle in the simulation while the stiffness k will take the value of the higher elastic constants used in the collisions. By choosing a simulation timestep that is smaller than the critical one it should be possible to obtain a stable and accurate simulation. It is up to the user to define the fraction of the critical timestep to be taken as the simulation timestep. To do that, a simple sensitivity analysis was carried out on the simplest setup composed of a particle bouncing on the floor. It was noted how, with timestep shorter than $\Delta t_c/5$ there are no more important precision advantages when compared to analytical results. That is why all of the simulation results that will be presented were computed using this particular timestep.

Chapter 5

Experimental Phase

Another important part of this work was the study and characterization of an existing vibratory conveyor regarding its ability to transport materials under different actuation conditions and orientations. This process has a dual purpose: primarily to better understand the transport mechanics of a real vibratory conveyor while, at the same time, obtaining important reference data to be used for the calibration and validation of the numerical DEM simulation.

This chapter will present all the results obtained during the experimental campaign. Starting from a description of the experimental setup and measuring instruments, the following chapter will then delve in to the set of calibration experiments used to obtain estimates for the values of the mechanical parameters to be implemented in the simulation code. Following that, an important chapter will be dedicated to a set of experiments aimed at characterizing the vibrational amplitude response of the conveyor setup when actuated with different frequencies, revealing a strong relationship between these two quantities that will have to be considered in the simulation process to correctly model the behavior of the experimental setup. The last section will instead present the bulk of the experimental results, focusing on the parametric study of the transport behavior of the vibratory conveyor. The actuation parameters and the sample mass have been varied within a certain range to study the effect of different parameters on the transport behavior.

5.1 Experimental Apparatus

Before presenting the experiments and their results, it is important to provide a comprehensive overview of the experimental apparatus and setup used to perform the experiments. This chapter will focus on a detailed description of the experimental equipment, including dimensions and operational capabilities.

The main scope of this work will be to analyze and understand the behavior of vibratory conveyors for material transport through both experimental and simulation work. Since there is a need to have experimental results to calibrate the simulation, a scaled down version of a vibratory conveyor system was required to perform all the experiments. An existing rig, designed at the Chair of Astronautics as part of previous research effort [27] was used for the entire experimental

phase.

The experimental setup used for this work presents all the characteristics of vibratory conveyors described in Section 3. The setup is equipped with a rectangular trough made of sheet steel. This planar design helps to facilitate visual inspection, both in real time and with video post-processing, of the material transported along the conveyor. The conveyor trough has an overall length of 250 mm and an internal rectangular cross section of 50 x 40 mm. The trough is supported by two plate springs mounted on an aluminum profile that acts as a base plate and is clamped to the workbench. The leaf springs that support the trough, form an articulated quadrilateral with the trough, allowing it to move slightly back and forth at a certain angle that can be set through a set of nuts and bolts. The plates used for the leaf springs are made of 0.5 mm thick steel, with a width of 50 mm and a length of 105 mm. The flexibility of the plates, which act as springs, is the main factor that allows the conveyor trough to vibrate, bringing it back to a central resting position with each vibrating cycle.

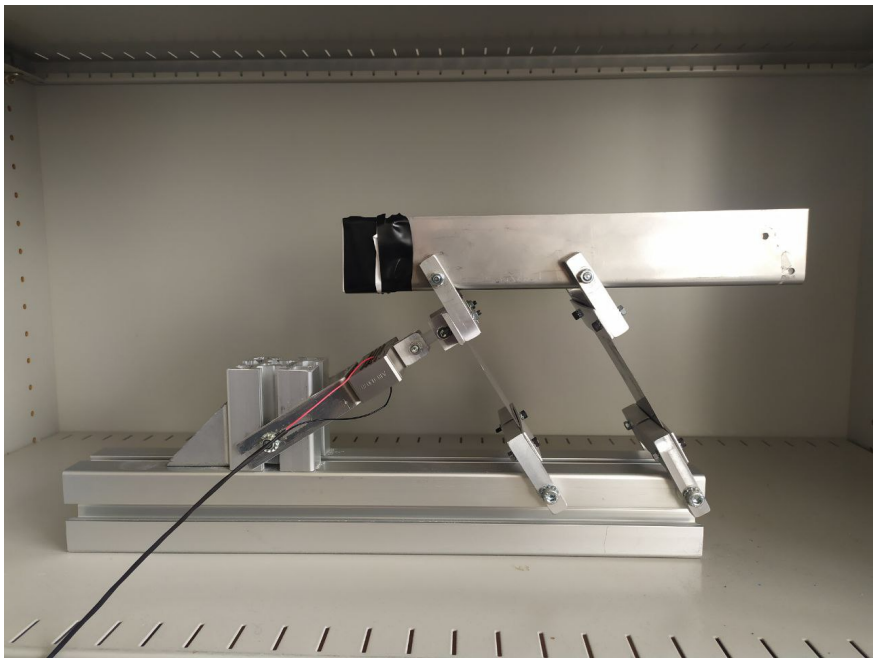

Figure 5.1: Photo of the conveyor experimental setup

The vibrations are generated by a piezoelectric actuator attached to the back of the conveyor trough. The actuator used in this setup is the FPA-1000E-P-1054-150-SS-1M4 FlexFrame PiezoActuator™ from Dynamic Structures & Materials, LLC. The completed experimental setup is shown in Figure 5.1, where it is possible to observe all the main components: the steel trough, the two plate springs, and, in the center, the piezoelectric actuator. The actuator is controlled by a wave generator that sends a control wave of a given frequency and amplitude to an amplifier that boosts it to the correct magnitude before sending it to the piezoelectric drive. The actuator operating settings have been set to a voltage of 0 ± 2 V - 100 ± 5 V on an analog sine wave, resulting in a stroke of about 0.3 mm, while the frequency can be freely varied from 0 Hz to about 70 Hz on the wave generator.

The angle β between the actuator and the base of the conveyor can be easily adjusted mechani-

cally by means of two screws that slide in the grooves of another aluminum profile that serves as the actuator support. The angle α of the whole assembly with respect to the horizontal, useful for testing the upward transport capabilities of the system, can be changed using some specially made 3D-printed supports that can be easily mounted on the conveyor assembly to impose an angle of 5 and 10 degrees respectively. A rendering of the entire conveyor setup tilted at a 5° angle using these 3D printed supports can be seen in Figure 5.6.

The main sensor used in the experimental campaign was the high precision GRAM XTREM-F scale, a fully digital and modular scale offering a resolution of 0.1 g with a sampling frequency of 5 Hz. The scale offers the ability to be connected to a computer running a specific software called PC-XTREM to record and save the data in specifically formatted CSV files. The scale is positioned on the desk, right below the discharge side of the conveyor and is used to measure the amount of material discharged over time.

5.2 Calibration Experiments

When using numerical simulations, it is necessary to consider the various factors that can affect the the results of the simulation in relation to the expected output in the case of known problems. Such factors can be the choice of different numerical methods, the quality of the input data and, ultimately, the values of the model parameters. In particular, the parameters used in a numerical simulation are used to represent various aspects of the simulation domain, such as material properties, boundary conditions, and geometric dimensions, and are therefore critical in determining the predictive power of the calculations. To ensure that the simulation produces results that reflects reality, within unavoidable error margins, it is necessary to introduce appropriate parameters into the simulation code, as emphasized in Section 4. These parameters have a strong influence in the result of the simulations so, any change in their values could yield totally different results leading to inaccurate or completely incorrect predictions.

This discrepancy becomes apparent when comparing simulation and experimental data. If simulations are run with parameters that do not match the appropriate values that ensure correspondence with reality, then the results will most likely not match the experimental data, thereby defeating the purpose of the simulation as a predictive tool. It is therefore of great importance to correctly evaluate and implement in the numerical simulation the appropriate values for the mechanical parameters to ensure that the simulation remains a useful tool.

In order to estimate the main parameters to be used in the simulation routine, a series of experiments were performed. First, to account for the differences between the sample mass used in the experiments and the equivalent number of 2D particles to be simulated, a first-order approximation of the number of simulated particles corresponding to a given sample mass is presented in Chapter 5.2.1. Subsequently, Chapters 5.2.2 and 5.2.3 present two experiments that were used to evaluate the shear and rolling friction coefficients, respectively. The results of the presented experiments can only be considered as preliminary estimates of the real values of the coefficients, since the measurements were performed with simple equipment and a simple methodology, with the limited scope of providing approximate values for the coefficients used in the DEM analysis. Nevertheless, the simulation results obtained with the parameter values discussed in this Chapter will be examined in Chapter 6, where a comparison of the experimental results with analytical predictions and with the results of actual transport experiments conducted on the experimental

setup will be presented, allowing an assessment of the accuracy of the code.

5.2.1 Determination of the number of simulated particles

One of the main limitations of the simulation presented in Chapter 4 is its restriction to a two-dimensional domain. This simplification of real-world phenomena, which evolve in a typical three-dimensional fashion, introduces an error into the model results since, for example, the simulated particles have less degrees of freedom to move along, the collision between particles are limited to a 2D plane and, the interaction with the lateral walls of the trough are completely absent in the simulation domain. However this simplification has the great advantage of making the entire simulation structure easier to build and faster to run. This is due to the fact that in a 2D simulations the collisions of the particles are much easier to compute and model, and, as will be soon explained, it requires the simulation of much less particles than the equivalent 3D configuration. In fact, when trying to reproduce or predict the result of an experiment, or the performance of an operational setup that must be designed to meet certain criteria, one of the main problems that must be considered when moving from real life to simulation is the conversion between the number of expected real 3D particles moving on the conveyor belt and the number of simulated particles that must be used in the simulation to represent the "corresponding" real life problem. It is easy to see that since the 2D simulation can be considered as a longitudinal slice of the experimental setup, the number of simulated particles should be less than the number of real particles. The conversion factor between these two quantities is the main unknown that needs to be discussed before proceeding with the simulation work.

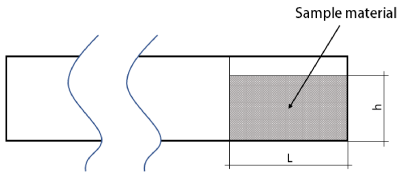

Figure 5.2: Side view of the initial configuration for the experimental setup. The powder bed has a fixed length $L = 50\,\text{mm}$ and variable height h based on the sample mass

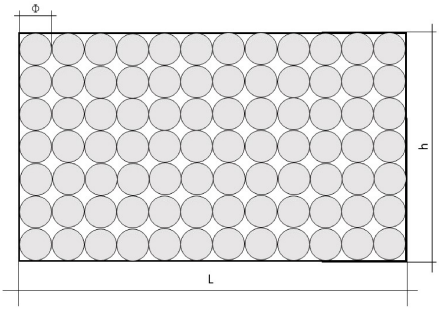

Figure 5.3: Disposition example for the simulation particles. The particles of diameter Φ are arranged in a rectangular fashion

Given the preliminary approach of this work and for simplicity of the model, a first order approximation was used. The initial configuration of the experimental sample mass was kept constant throughout the various run of the experiments with a total length of the initial powder bed of $L = 50\,\text{mm}$, as can be seen in Figure 5.2. This particular length was chosen since it proved to be enough to contain the whole range of sample masses used during the course of the experimental campaign while being small enough to give the bulk material enough length of trough to travel through. Given this constant length, different masses of bulk material will produce different heights h for the powder bed. By measuring this height for different sample masses, a linear relationship was found between mass and bed height, as can be expected. Given that the 2D sim-

ulation can be considered a "slice" of the real 3D experiment, the number of simulated particles to be used in the simulation environment was simply determined by computing the number of particles of known radius r that could fit inside a rectangle of dimensions L and h in a simple rectangular arrangement, as in Figure 5.3.

Table 5.1: Conversion between experimental mass and number of simulated particle

Mass [g]	h [mm]	N° Simulated Particles
5	1.5	1875
10	3	3750
20	7	8750
40	12	15000
60	17,5	21875
80	24,5	30625
100	30	37500

Given this assumption it is possible to compute the number of simulated particle to be used inside of the simulation environment given a certain "real" sample mass whose behavior must be studied.

$$N_p = \frac{Lh}{r^2} \tag{5.1}$$

The measured bed powder height and the computed total simulation particles for each sample mass are presented in Table 5.1 where it can be easily seen how the number of particles to be used in the simulation changes drastically from one mass to another. From the lower tested mass of 5 g and the highest of 100 g the number of simulated particles changes of more than one order of magnitude going from around 1900 up to 37 500 particles.

5.2.2 Estimation of shear friction coefficient

One of the main parameters to be evaluated is the *shear friction coefficient*. This coefficient is used in the simple linear model that was used to numerically describe the effect of friction on every single simulated particle as presented in Section 4. Following this numerical implementation, a linear relationship is constructed between the normal force F_N, pressing a particle against some kind of surface, and the shear force S that is required to cause the material to start sliding along that surface. This relationship takes the form of:

$$S = \mu F_N + C \tag{5.2}$$

where μ is the aforementioned coefficient of friction and the constant C is the *cohesion parameter* describing the adhesion between the particle and the surface with which it is colliding. Equation 5.2, when plotted, defines a line whose angle $\tan^{-1}\mu$ is called *angle of friction*. This linear model, while being analytically simple to understand and implement in a numerical form, is found to be a reliable representation of the behavior of bulk solids [12].

To experimentally evaluate the friction coefficient of the glass spheres used as reference material the *Tilting plate method* is employed. This simple procedure, presented in the book by Woodcock and Mason [12], requires: a thin layer of sample material, a tilting surface made of the same material as the conveyor's walls, and a way to measure the tilt angle. The sample material used in this experiment was composed of glass spheres, sieved to ensure a diameter $> 200\,\mu m$. The

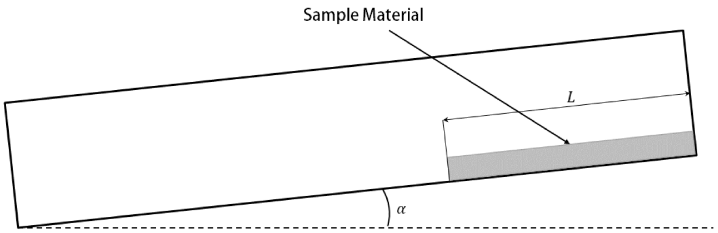

Figure 5.4: Experimental setup for the evaluation of the friction coefficient through the use of the tilting plate method

tilting plate was the conveyor itself since, given its small dimensions and low weight, it was easy to tilt it by hand to a desired angle. The readings of the tilting angle were provided by an accelerometer, fixed to the main structure of the conveyor, with an error of $\pm 1^{\circ}$.

The procedure of the experiment is simple: first a thin layer of the bulk material is placed on the conveyor positioned in an horizontal position, then the whole setup is slowly tilted, increasing α, until the angle at which the sample layer slides off is measured. By rewriting the equation 5.2 it is possible to obtain:

$$\frac{mg}{A}\sin\alpha = \mu\frac{mg}{A}\cos\alpha + C \tag{5.3}$$

Where m is the mass of the bulk solid on the plate, A is the nominal contact area between the bulk solid and the plate, and α is the angle at which sliding is observed. By repeating this process for different masses m of glass spheres, and different lengths L of the powder bed, it is possible to plot $(mg/A)\cos\alpha (= F_n)$ against $(mg/A)\sin\alpha (= S)$, where the area A is computed as the product between the length L of the powder bed and the fixed width of the conveyor belt b. This plot should give a *straight line* of slope μ and intercept C. It is furthermore possible to compute the *angle of friction* $\Phi = \tan^{-1}\mu$.

The results obtained using the tilting plate method are summarized in Table A.3 in Appendix A, where it is possible to observe the different masses and contact areas used for the multiple runs of the experiment. The two rightmost columns are computed using the known mass and contact area with the recorded angle α, at which sliding occurs, using the two sides of Equation 5.3. For the acceleration of gravity g, the known Earth's surface value of $9.807\,\mathrm{m\,s^{-2}}$ was used [45]. As said before, it is necessary to plot the data from the last two columns against each other. The results can be seen in the scatter plot in Figure 5.5, where the data computed with $(mg/A)\cos\alpha$ was plotted against $(mg/A)\sin\alpha$ with the errors computed using the known rules of error propagation starting from the known measurement errors. In the figure it is also possible to see the trend line computed with a simple linear regression model resulting in a line with equation:

$$y = 0.1126x + 5.8269 \tag{5.4}$$

This trend line provides all the information needed to estimate the coefficients that describe friction in the model. In particular, as explained before it is possible to find the value of the coefficient

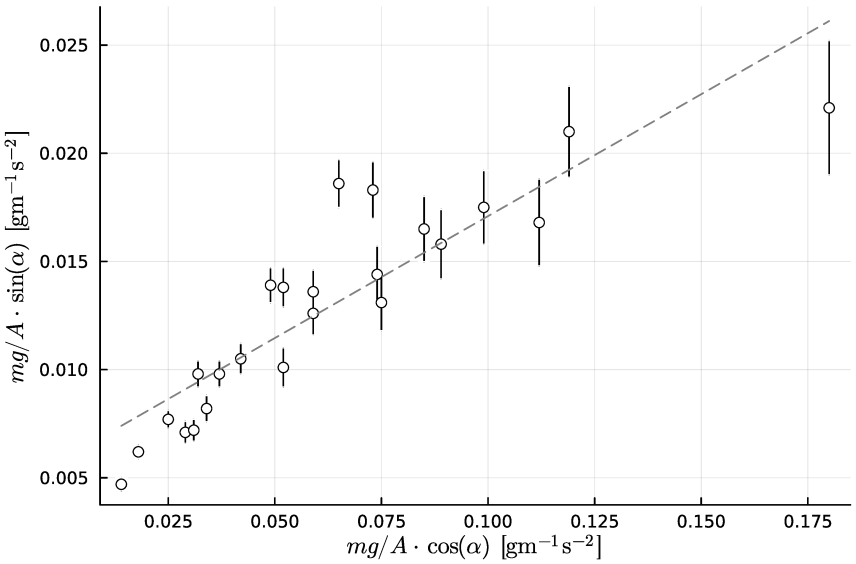

Figure 5.5: Scatter plot obtained by plotting $(mg/A)\cos\alpha$ against $(mg/A)\sin\alpha$, the trend line was computed with a linear regression scheme

of friction μ, the cohesion parameter C and the angle of friction Φ:

$$\mu = 0.1126 \tag{5.5}$$

$$C = 0.005\,83\,\mathrm{kg\,m^{-1}\,s^{2}} \tag{5.6}$$

$$\Phi = \tan^{-1}\mu = 6.426^{\circ} \tag{5.7}$$

These values are obviously characterized by a certain error that is not easy to estimate due to the experimental procedure and the computations that led to the extraction of the results from the plot. Due to that, an exact estimation of the error will no be given but the reader must keep in mind that the values here presented are to be used as a preliminary estimation of these parameters and are offered without warranty of their precision. This results, as presented, were then employed to evaluate friction forces in the simulation. To validate the simulation results obtained with these values, a set of simple simulations was completed and the results are presented in Chapter 6.

5.2.3 Estimation of rolling friction coefficient

Another coefficient that can be estimated with a simple and relatively quick experiment is the *rolling friction coefficient*. This parameter is used to describe the natural slowing down of a rolling particle due to the reciprocal interaction between the particle and the surface on which it is rolling. The analytical and numerical model used in the simulation to describe this behavior have been previously presented in Chapter 4.3.3 where Equations 4.16, 4.17 and 4.18 were derived. These

equation are written here again for ease of reference:

$$\mu_R = \frac{1}{\gamma + 1}\frac{d}{R}$$
$$d = \mu_R(1+\gamma)R$$
$$M_R = -|F_n|\,\mathrm{sgn}(\dot{\theta})d$$

Since rolling friction is a phenomenon that, as the name implies, affects rolling objects, it is necessary to put the glass spheres used in the experimental setup into some kind of controlled rolling motion. To do this, a set of 3D printed brackets were designed to be easily mounted on the entire conveyor assembly to keep it at a given angle of inclination with respect to the resting surface. Two different support structures were made, one with an angle of 5° and another with an angle of 10°. In Figure 5.6 it is possible to see a rendering of the inclined conveyor assembly held at a 5° angle with respect to the floor thanks to the 3D printed support (in orange).

Figure 5.6: Rendering of the conveyor assembly kept at a 5° angle thanks to the use of a 3D printed support structure (in orange)

Once the inclination of the whole setup has been fixed, it is possible to proceed with a very simple experimental process. The procedure involves the use of individual glass spheres of known diameter, that are allowed to roll down the whole conveyor one at the time. The experimental aim is to measure the time taken for the spheres to travel from the start to the end of the trough. To ensure a sufficient measuring accuracy the rolling time is measured with both a handheld chronometer and, secondly, analyzing the movement of the spheres on the conveyor through frame by frame analysis of video recording of the experiment process.

As it is known from basic mechanics, an object rolling or sliding down an incline of angle α will be subject to a constant downward acceleration component a, in a direction aligned with the

inclined surface, of magnitude $a = g \sin \alpha$ due to the effect of its own weight. It is reasonable to expect that the particles will behave in a similar fashion, rolling down the inclined conveyor at a constant acceleration that will be smaller than the ideal one due to the effect of rolling friction. Since the length of the conveyor's trough is known, $L = 250\,\text{mm}$, it is easy to compute the average acceleration of the particles knowing the time span Δt that was used to roll from the top to the bottom, assuming that there is no dependence of the forces on the velocity of the particle and, thus, no variation in acceleration:

$$a_{exp} = \frac{2L}{\Delta t^2} \tag{5.8}$$

Remembering the acceleration equation (Equation 4.15) derived in Chapter 4.3.3, it is possible to impose the equality between the acceleration obtained from the experimental measures and the one obtained analytically from the description of the rolling friction phenomena.

$$a_{exp} = \frac{g}{\gamma + 1} \sin\theta - \frac{1}{(\gamma + 1)} \frac{d}{R} g \cos\theta \tag{5.9}$$

$$= \frac{g}{\gamma + 1} \sin\theta - \mu_R g \cos\theta \tag{5.10}$$

Since the experimental acceleration in the formula is known, it is possible to rewrite the equation to obtain the value of the rolling friction coefficient μ_R:

$$\mu_R = \frac{-a_{exp} + [g/(\gamma + 1)] \sin\theta}{g \cos\theta} \tag{5.11}$$

This experiment was repeated for both 5° and 10° inclination using glass spheres with a diameter of 200 µm, resulting in the data gathered in Table A.1 and A.2 in Appendix A.1. In the "Time" column the time measured during the experimental phase in seconds is recorded while the last two column are computed using Equations 5.8 and 5.11 and contain, respectively, the average acceleration and the corresponding estimated value of the rolling friction coefficient μ_R. The last row of both tables contains the average of the respective columns, resulting in a final average value for the friction coefficient. It is interesting to see how the resulting coefficient of rolling friction differs in the two experiments depending on the angle of the whole conveyor setup. With an inclination angle of 5° the corresponding coefficient of rolling friction takes the value of about $\mu_{R,5} = 0.0618$ while, for an angle of 10°, the coefficient is equal to about double the previous one, at around $\mu_{R,10} = 0.1205$. This is in contrast with the results obtained by other authors [34] [35] [36] who observed that the coefficient of rolling friction should be independent of the angle of the surface. This discrepancy is probably due to the simplicity of the instrumentation used for the experiment. In any case the standard deviation of the mean (SEM) was computed using the data from the 14 runs of the experiment by first computing the standard deviation of the data (STD) and dividing it by the square root of the total number of runs:

$$SEM = \frac{STD(\mu_i)}{\sqrt{N_i}} \tag{5.12}$$

where μ_i is the value of the coefficient of rolling friction computed at each run, and N_i is the total number of measurements. Computing this value for both the experimental configuration yields $SEM_5 = 5.59 \times 10^{-5}$ and $SEM_{10} = 3.08 \times 10^{-4}$ that, when compared to the value of the measurements seems to indicate a relative error lower than 0.5 %.

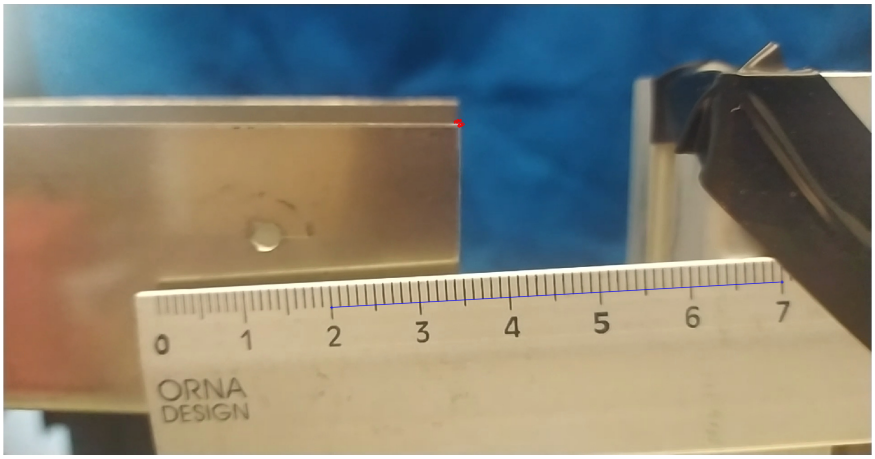

Figure 5.7: Example frame from the video used to extract the vibration amplitude of the trough, it is possible to see the measuring stick and the red marker used in *Tracker* to track the position of the edge over time

These results will be used, together with the others obtained in the previous chapters, as a first rough estimation of the values to be used in the simulation. The results of the simulations ran with this set of parameters will be presented in Section 6, where they will be compared with analytical reference cases and real transport experiments executed on the vibrational conveyor.

5.3 Vibration amplitude measurements

As presented in Chapter 5.1, the piezoelectric actuator is driven by an amplifier that is fed by a wave generator that can generate sinusoidal voltage waves at a desired frequency. While the instrument also enables the modulation of the total amplitude of the voltage wave, it was suggested to keep that setting stable and to work only on the frequency, due to previous calibration work that resulted in an estimated total vibration amplitude of 0.3 mm. During early phases of the experimental campaign, as will be presented in Chapter 5.4.4, it was noted that the whole conveyor setup showed some resonance zones inside the tested frequency domain, making it important to check for variation in amplitude on the trough's vibrations. That is why an experimental procedure was set up to acquire vibration data to analyze with the help of some specially made scripts.

The conveyor setup was fixed on the lab bench in an horizontal position ($\alpha = 0°$) and an high-speed camera was positioned as to get a side view of the trough. In particular, the frame was set as to include one of the edges of the trough so that movements along both the x-axis and y-axis could be appreciated as illustrated in an example shot in Figure 5.7. In the same image it is also possible to appreciate the presence of a measuring stick that is used as a dimensional reference to extract the position, in millimeters, of the edge from the video. The usual frequency range was analyzed, from 30 Hz to 55 Hz with 5 Hz increments, thus obtaining data across the whole range. It was not possible to analyze the last frequency point of 60 Hz due to the limitation of the high-speed camera, that was shooting at only 120 frames per second.

The videos, taken for each actuation frequency, were then analyzed with *Tracker* [46], a powerful

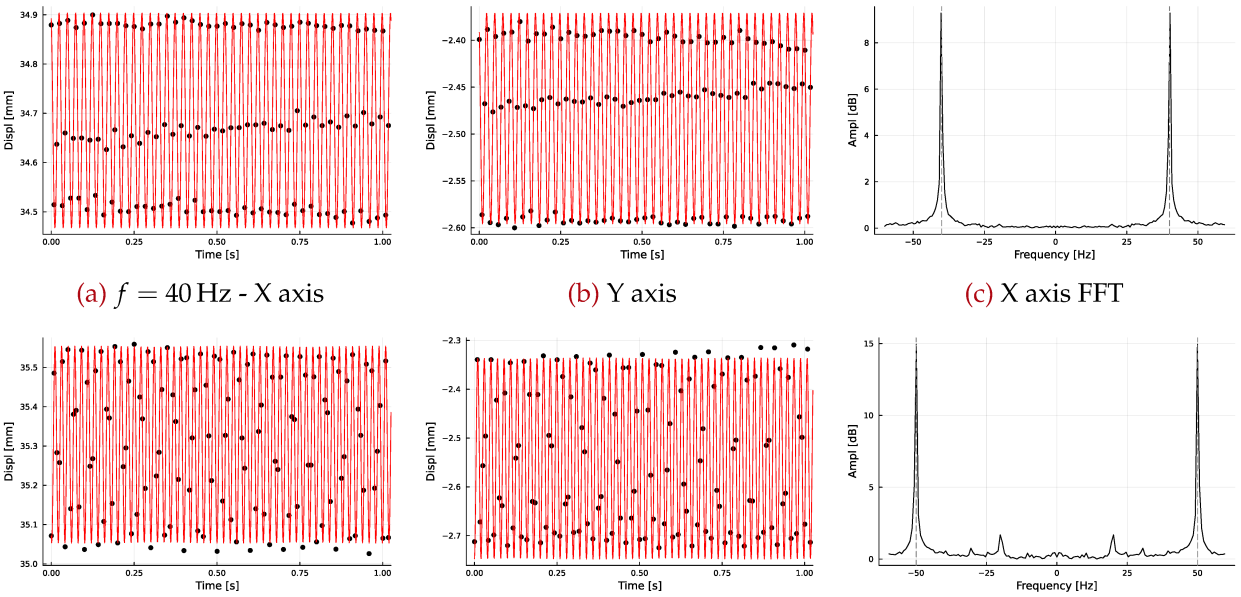

(a) $f = 40\,\text{Hz}$ - X axis (b) Y axis (c) X axis FFT

(d) $f = 50\,\text{Hz}$ - X axis (e) Y axis (f) X axis FFT

Figure 5.8: Data obtained by video analysis, in the top row the results for an excitation frequency of $f = 40\,\text{Hz}$ while in the bottom row for $f = 50\,\text{Hz}$. The first two columns represent the data points (black) and the approximation function for x and y axis (red), the last column present the FFT of the data points

video analysis software, developed by the Open Source Physics Project [47], that allows the extraction and analysis of the movements of objects within a video with a known reference frame. To keep track of the position of the edge of the trough over time the auto-tracking feature of the software was used: it was only necessary to give a first point for the tracking procedure to start advancing frame by frame. The Tracker position extraction algorithm was calibrated using the aforementioned measuring stick present in the shot, and it provided data on the position over time of the edge along the vertical and horizontal axis.

Once all of these data points are available it is possible to proceed with the analysis, trying to find an appropriate approximate function that is able to describe the evolution of these quantities over time. Given the physics of the phenomena, it is reasonable to expect some kind of harmonic function in the generic shape of:

$$x(t) = A \cdot \sin(Bt + C) + D \tag{5.13}$$

These 4 parameters are used to describe a generic harmonic function with given amplitude (A), angular velocity (B), phase (C) and displacement (D). It is then a matter of finding the right parameters to obtain the best approximation possible of the data extracted from the videos. A simple regression scheme was used to obtain the different approximation functions at different frequencies, some of which are presented in Figure 5.8. In this set of figures the results for 40 and 50 Hz are presented in the top and bottom row respectively. The first two columns present the position data points extracted from each frame of the video along the x and y axis as black points while, on the same plot, the red sinusoidal curve is the approximation function computed by finding the right coefficients in Equation 5.13. The last row, instead, presents a graph showing

the frequency response of the system computed from the extracted data point through the use of a Fast Fourier Transform (FFT) algorithm. It is possible to see how, in both cases, the peaks highlighted by the FFT correspond to the expected values of 40 and 50 Hz confirming that the video recordings managed to represent the expected behavior of the system quite closely, resulting in FFT plots with tight peaks and low harmonic noise.

By repeating this process for all the videos taken at different frequencies, twelve sinusoidal approximant functions, in the shape of Equation 5.13, were computed: given the six different frequencies analyzed in the experimental run and the two direction, x and y, for each one of them. Since this analysis is mainly focused on the variation of the vibration amplitude with the frequency the term A of Equation 5.13 was extracted to be used as a measure of the measured vibration amplitude. The obtained amplitudes, for both x and y axis, are plotted in Figure 5.9 and 5.10 respectively where it is possible to appreciate how the amplitude tends to increase in a linear fashion with the frequency. The error bars represent one standard error computed by comparing the data points with the approximant sinusoidal function computed in the last step while the red lines represent the linear approximant of the relationship between amplitude and frequency. By means of a simple vector sum it is possible to compute the total vibration amplitude as:

$$A(f) = \sqrt{A_x^2 + A_y^2} \tag{5.14}$$

which results in a the amplitudes shown in Figure 5.11. These plots seem to suggest the existence, in this particular setup, of a linear relationship between the actuation frequency, set on the wave generator, and the vibration amplitude observed on the trough during the vibration process. This kind of dependence could originate from the different mechanical interactions on the whole experimental setup, starting from the leaf springs and up to the joints between the actuator and the rest of the structure. It will be important, in the following analysis, to remember that each time the experimental frequency will be changed, it will correspond to a change in the amplitude of the excitation waveform.

To make use of all of the acquired data, the linear approximant function was computed for the total amplitude and the single x, y axis amplitudes and implemented in the DEM simulator environment to account for these particular behavior. This should make it possible to describe the evolution of the amplitude with the frequency also in the simulated environment to obtain better fitting data between simulation and experimental results.

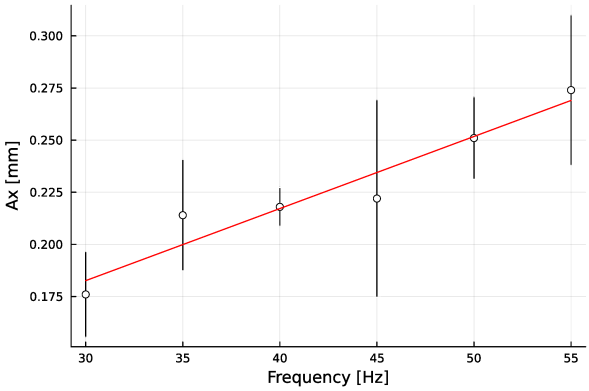

Figure 5.9: Evolution of the extracted vibration amplitude along x-axis. Extracted data points (circles), with error bars and approximant linear function (red)

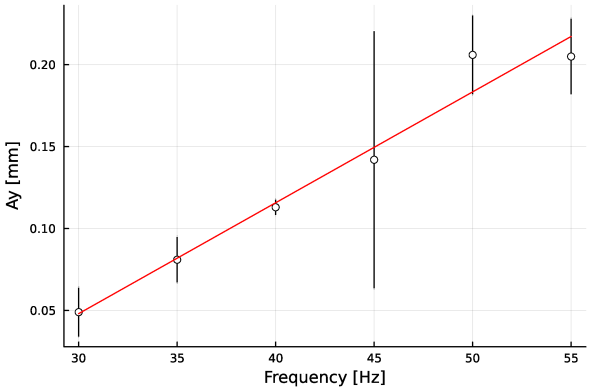

Figure 5.10: Evolution of the extracted vibration amplitude along y-axis. Extracted data points (circles), with error bars and approximant linear function (red)

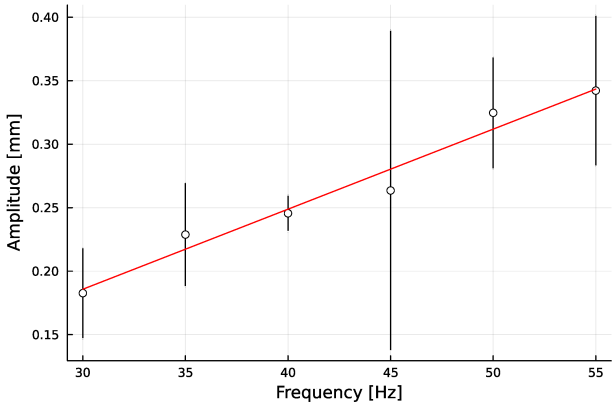

Figure 5.11: Evolution of the measured total vibration amplitude. Extracted data points (circles), with error bars and approximant linear function (red)

5.4 Transport Experiments

After having acquired all of the necessary information regarding the sample particle's coefficients it was possible to begin the main bulk of the experimental work. In this second phase, a parametric study concerning the transport characteristics of the complete system was performed, consisting in a set of experiments that were run on the setup described in Chapter 5.1, with the aim of characterizing the transport capabilities in terms of *vibration frequency*, *sample mass*, and *inclination of the setup*.

The main focus of this experimental phase was to get a deeper understanding of the transport behavior of bulk materials on vibratory conveyors while, at the same time, collecting useful data to be used as a reference for the performance of the DEM simulator. As previously stated, the experiments were run on a preexisting vibratory conveyor setup that was fitted with a precision scale, a GRAM Xtrem F, to record the discharged mass over time. This scale offers a resolution of 0.1 g and an Ethernet interface to send the recorded weight data to a data acquisition system, in this case a personal computer equipped with the X-Trem acquisition software. This particular scale is able to record and send data with a frequency of 5 readings per seconds. This acquisition frequency has proved to be enough for the scope of the work, given that the typical discharge phenomena takes place in the span of some seconds up to two minutes for the sample masses here employed. Having 5 readings per seconds was enough to obtain smooth discharge curves for analysis purposes in all the different cases.

The recordings of the fallen mass over time provided by the scale for each experiments are saved for later analysis. In addition to these numerical data, some experimental runs were recorded with a camera to extract other useful qualitative and quantitative data, such as the shape of the material and its speed during the transport process. The video analysis will be presented in Section 6.3 of the Validation chapter, where a Tracker [46] was used to extract the transport speed of the material on the conveyor's trough.

The experiments here presented make use of glass particles sieved as to ensure a diameter greater than 200 µm. The motivation for this choice are twofold: firstly big particles are faster to simulate in a DEM environment since bigger timestep can be used to ensure the same maximum penetration length, secondly, smaller particles would have proven to be more difficult to handle without specific safety devices such as masks or fume hoods to prevent their inhalation.

The basic parametric study was done with the conveyor set in an horizontal configuration ($\alpha = 0°$) where sample mass and frequency were progressively changed in the following ranges:

$$f = [10, 20, 25, 30, 32.5, 35, 37.5, 40, 45, 50, 55, 60]\text{Hz}$$
$$m = [5, 10, 20, 40, 60, 80, 100]\text{g}$$

Furthermore the whole experimental process was repeated for $\alpha = 5°$ on a slightly different frequency and sample mass range to accommodate for the diverse transport behavior:

$$f = [10, 20, 25, 30, 32.5, 35, 37.5, 40, 45, 50, 55, 60, 65, 70]\text{Hz}$$
$$m = [10, 40, 60]\text{g}$$

All the possible combination of the previous parameters were tested with 6 different runs of the

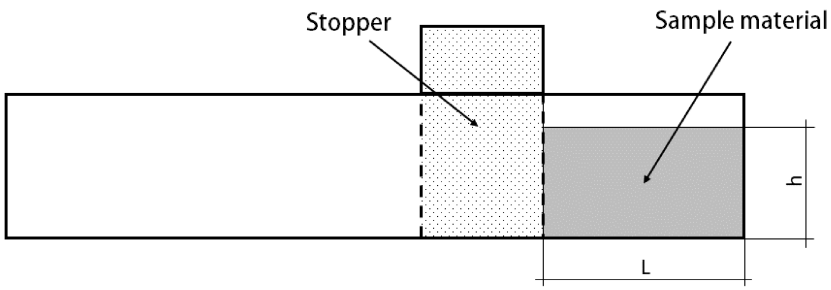

Figure 5.12: Initial configuration for transport experiments

same experiment as to have a statistical basis on which to build all the data analysis process that will be presented in the following chapters.

As previously said, the main scope of the work will be the development of a knowledge base regarding vibratory conveyors of a small size, since the main applications would be the movement of small amount of material for analysis purposes. That is why the chosen mass sample range covers only amounts of bulk materials lower or equal to 100 g. Furthermore, lower amount of material are also easier to simulate with the DEM simulation code, since a lower number of particles entails a drastic decrease in computational time and resources.

5.4.1 Transport experiment procedure

After connecting the scale to the computer, turning on the wave generator that controls the piezoelectric actuator and ensuring the correct connection of the scale with the acquisition software, it is possible to proceed with the experimental runs. All of the transport experiments follow the same experimental procedure to ensure repeatability of the results:

As shown in the example in Figure 5.13, the data collected by the scale for each of these experiments consists of the evolution of the weight of the bulk material on the scale over time. The recorded weight is equal to zero at the beginning of each run of the experiment. As the material is transported along the trough and falls on the scale, the recorded weight increases until all the material is finally unloaded. At the end of each experiment, the final mass on the scale should be equal to the mass of the sample that was placed in the trough at the beginning of the experiment, but this is often not the case because some residue is left in the trough for certain transport configurations.

As previously stated this procedure was repeated 6 times for all the cases considered during the parametric study making it so 6 different discharge curves were available for each configuration. To reduce the effect of random errors in the experimental process, these six runs where used to compute an *average discharge curve* over time for each configuration of frequency and sample mass. Given that the scale was recording at a fixed frequency of 5 measurements per second, the computation of the average curve was done by aligning all of the six runs to the same starting

Step	Description
1	The conveyor setup is set to the desired α angle using the custom-made wedges and supports.
2	The desired amount of sample material is weighed on the scale.
3	The desired vibration frequency is set on the wave generator.
4	With the piezoelectric amplifier turned off, thus with no vibration on the trough, the stopper is placed at a distance of 50 mm from the end of the trough, as shown in Figure 5.12.
5	The sample material is poured into the trough between the spacer and the end of the trough itself.
6	The stopper is slowly removed, allowing the bulk material to settle, and the data recording is enabled on the X-Trem software.
7	The piezoelectric amplifier is turned on, powering up the actuator and initiating vibration on the trough.
8	The sample material is transported along the trough and eventually falls onto the scale inside a pre-placed container.
9	Once all the material has fallen onto the scale, the data recording on X-Trem is turned off, and the amplifier is switched off, ceasing the vibrations.

time and then computing the average at each time interval:

$$\bar{m}(\tau) = \frac{1}{6}\sum_{i=1}^{6} m_i(\tau) \tag{5.15}$$

where τ represent a generic timestep. An example of the six experimental acquisitions and the average computed in this way can be seen in Figure 5.14 where the average run is plotted with a thick black line.

In Figure 5.14 it is possible to distinguish the three main different parts that characterize the behavior of all the recorded discharge data series:

- In the first part of the plot, for times lower than around 8 s for this particular configuration, it is possible to see how the recorded weight is zero. During this period of time the vibratory conveyor is turned on and the material is being transported along the trough but has yet to reach the end of the conveyor;

- In the second part, starting from around 8 s up until 10 s, an initial transient in the mass flow is observed with the first front of the material reaching the end of the trough and starting to fall on the scale;

- The central part of the graph, from around 10 s up to around 22 s, makes up the bulk of the transport time. In this period of time we reach an almost steady state condition with a more or less linear discharge behavior over time;

- In the last seconds, after 22 s from the turning on of the vibration, another transient is observed with the discharge flow slowing down until the total mass has been successfully discharged.

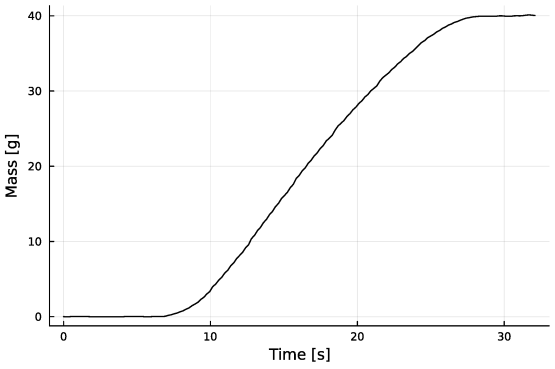

Figure 5.13: Example of the discharged mass measured by the scale over time, for a vibration frequency of 40 Hz and $\alpha = 0°$

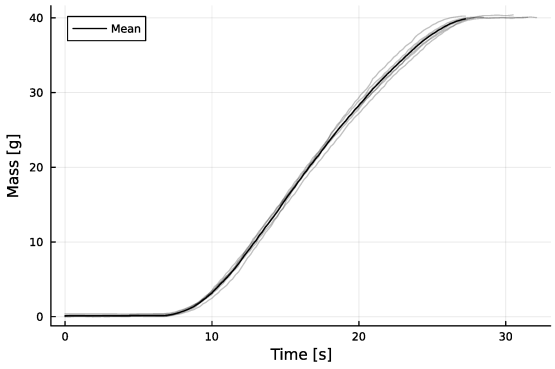

Figure 5.14: Example of the average discharged mass computed as the mean of the 6 runs, for a vibration frequency of 40 Hz and $\alpha = 0°$. It is possible to observe the various typical stages of the discharge pattern

The main focus of this thesis will be the analysis of the central region, characterized by an quasi-steady state behavior since it could be used as a reference condition for typical applications working with this kind of regimes. The exact definition of the borders of this central part of the graph is hard to determine since the extension of the transient zones tends to vary from case to case. In the next chapter, after a normalization process, a possible determination of the values of the edges of this region will be proposed as a way to facilitate the comparison between experimental and simulated data.

5.4.2 Normalized discharge curves

In order to gain insights into the transport behavior of vibratory conveyors, it is important to compare different transport configurations to examine the impact of various parameters through the analysis of the recorded experimental data. To facilitate the comparison of different experiments, this chapter will primarily concentrate on the examination of normalized data along both time and mass. Such an approach allows for highlighting the differences in the shape of the discharge curves with respect to changes in actuation frequency, amplitude, and experimental sample mass.

As outlined in the previous chapter, each experimental configuration was tested six times making it possible to compute the average of the discharged mass over time. This time series serves as a reference for that specific configuration and facilitates the comparison of the experimental data obtained in different conditions. Given these preliminary considerations it is now possible to normalize the data over both time and mass to make it possible to compare different experiments between each other.

The mass was normalized in a range from 0 to 1 in order to make the measurements of the fallen mass independent from the initial sample mass value. To accomplish this, the mass data recorded in a particular experiment was normalized by dividing it by the total sample mass used in that specific configuration. This normalization process can be expressed mathematically as:

$$m_N(\tau) = \frac{1}{m_s} m(\tau) \tag{5.16}$$

Where m_N represents the normalized mass at time τ, m_s is the total sample mass used in the specific configuration, and $m(\tau)$ represents the mass at time τ. By performing this operation, the mass is expressed as a percentage of the discharged mass with respect to the initial sample mass. This ensures that the recorded mass data is comparable between different experiments and configurations.

Once the mass has been normalized it is necessary to find a suitable way to also normalize the time axis. All of the tested configuration exhibit drastically different discharge times, from the slowest ones taking up to two minutes for a complete discharge, to the faster ones managing to discharge the whole sample mass in a couple of seconds. To uniform this high variability of transport times between different starting conditions it was decided to align the different time axis to the same starting time: the instant τ_i at which the scale measured a discharged mass equal to a certain percentage P_i of the initial mass.By changing the value of P_i it is possible to move the starting point to exclude a smaller or bigger part of the initial transient region.

To define a final point that can be shared across all different experimental configurations a similar approach has been followed. Each normalized mass data series has been analyzed to identify the time step τ_f at which a certain percentage P_f of the total mass has been reached. As for the previous case by changing the the desired value of P_f it is possible to fix the extension of the central quasi-steady state zone, making it possible to stop the analysis before the onset of the final transient.

Once this two point have been identified for each one of the average experimental data it is possible to scale the time between τ_i and τ_f using the value of τ_f for each of these timeseries, making it so that the evolution of the mass-normalized discharge curve evolves from a normalized time 0, which corresponds to an initial discharged mass percentage P_i, up to a normalized time 1, when the normalized discharged mass takes the value of P_f.

The results of this normalization process for a particular experiment can be seen in Figure 5.15. In this figure the y-axis represents the normalized mass, as defined in the previous paragraphs, while on the x-axis the normalized time is expressed for a normalization mass percentage corresponding to $P_i = 10\,\%$ and $P_f = 80\,\%$. As explained before, the time step at which the normalized mass reaches the value of 0.1 is aligned at 0 along the time-normalized x-axis, while the time step corresponding to a measured normalized mass of 0.8 is aligned to 1. This implies that all of the data related to initial transient, before τ_i, are placed on negative normalized time values, conversely all the points related to the final transient gets pushed to x-axis values greater than 1.

By changing the two parameters P_i and P_f, it is possible to expand or reduce the amplitude of what is considered to be the central part of the discharge envelope making the whole normalized plot appear more squished or dilated depending on the chosen values. While the main focus of this chapter will be the qualitative analysis of the discharge pattern shape that is not so sensitive upon these limits, in the next chapters it will become clear how the determination of these two values is critical in the computation of the experimental mass flow. That is why, considering the comparison that will be made with the simulation results and presented in Chapter 6.4, it was chosen to use $P_i = 0.1$ and $P_f = 0.8$, as to exclude the long transient tails that will be observed in the simulation data.

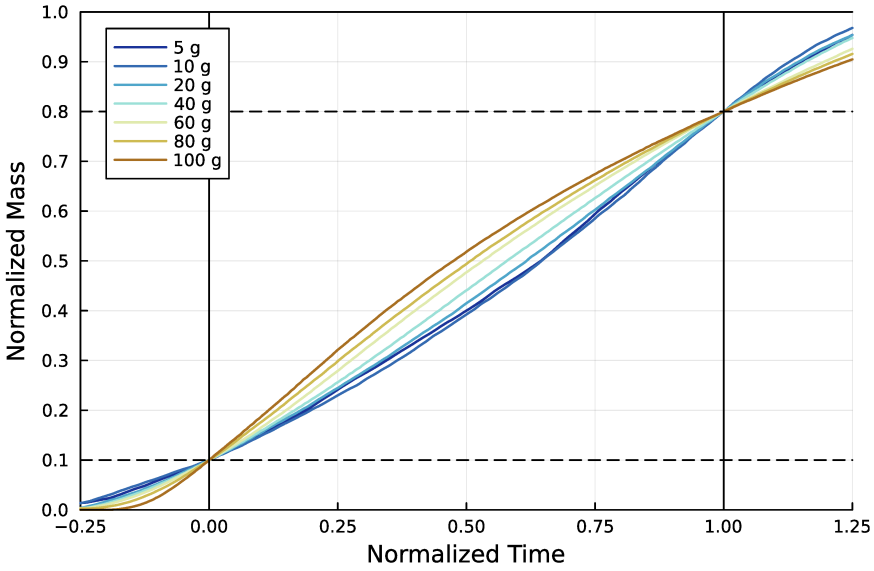

Figure 5.15: Normalized and aligned discharge curves for different sample masses with an actuation frequency of $f = 40\,\text{Hz}$. It is possible to observe how the shape of the discharge pattern changes with the sample mass size.

Once these two values have been decided it is possible to begin the analysis of the data. As can be see in Figure 5.15, it was chosen to compare in the same graph a set of configuration characterized by the same actuation frequency, 40 Hz in the case of this particular figure, but with different initial sample mass. Thanks to the normalization presented in this chapter it is possible to appreciate how different sample mass corresponds to different shapes for the discharge pattern. It is interesting to see how, while the experiments executed with a lower sample mass result in discharge patterns that are really close with each other while, as the mass increases, the difference becomes more important in the shape of the respective patterns, making it possible to understand that the amount of mass that is present on the conveyor during transport has a non negligible effect on the discharge behavior over time.

In particular, for this specific frequency, it is possible to observe how transport experiments executed with a low amount of bulk solid, from 5 to around 20 g, are characterized by a *convex* evolution of the discharge pattern, with a slower initial flow that constantly increases until the final transient. On the other hand the data recorded for experiments with a higher sample mass, for example the one with 100 g of glass spheres, shows a *concave* evolution of the discharge pattern. In this second case then, in the beginning, the transport is characterized by a higher flow of material on the scale that starts to progressively slow down after about half of the normalized time.

The different behavior of these two configuration, the one with a mass of 5 g and the other with 100 g of material, becomes apparent in the central part of the plot. By considering the middle point of the normalized time, $\tau_N = 0.5$, corresponding to the time step at which all of the different configuration were in the middle of their central quasi-linear discharge zone, it is possible to observe how much of the original normalized mass has already been discharged in that moment. For the case of $m_s = 5\,\text{g}$, at $\tau_N = 0.5$ only around 0.4 of the normalized mass has been discharged,

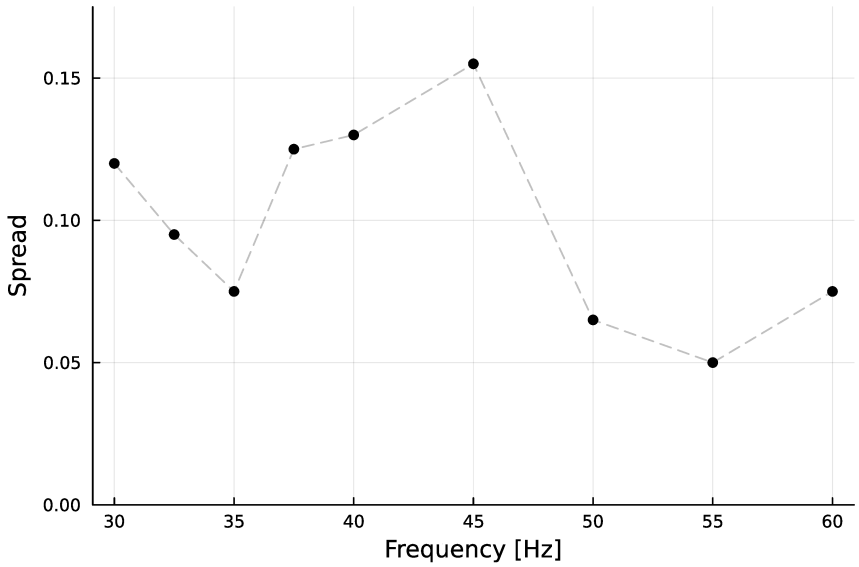

Figure 5.16: Evolution of the discharge pattern spread over different frequencies at a normalized time of 0.5

while the experiment with the higher tested mass of 100 g had already discharged more than 0.5 of the normalized mass resulting in a total difference of more than 0.1. Employing the vibratory conveyor with a higher mass on the trough will lead to a higher initial throughput that will progressively slow down over time, while a conveyor that is running with a lower amount of material on the trough will present a lower discharge rate in the initial part of the envelope that will then gradually increase over time.

An interesting point that is yet to be discussed is the evolution of the maximum spread over the discharge patterns for different actuation frequencies. The maximum spread at the normalized time of 0.5 was computed for data acquired in the whole range of tested frequencies, resulting in the plot presented in Figure 5.16 where each dot represent the spread at a specific frequency while the dashed line is just for ease of interpretation. From the limited range of available data it is difficult to determine a clear evolution of the maximum spread since the data points are highly dispersed without a clearly visible pattern. Nonetheless for frequencies higher than 50 Hz the maximum spread seems to be lower than the one observed with lower frequencies. It is also possible to appreciate the reduction of the spread at higher frequencies by observing the normalized plots computed at these different configurations, presented in Figure 5.17a to 5.17c. At higher frequencies the difference in shape between *convex* and *concave* evolutions becomes noticeably less pronounced. The more uniform and tightly packed patterns at higher frequencies could be due to the higher energy transmission to the bulk, which is observed for this kind of actuation configuration, but more research is needed in exactly determining the origin of this phenomenon.

5.4.3 Vibration frequency normalized discharge curves

Having previously examined the effect of sample mass and frequency on the shape of the discharge patterns, it could be worthwhile investigating the relationship between actuation fre-

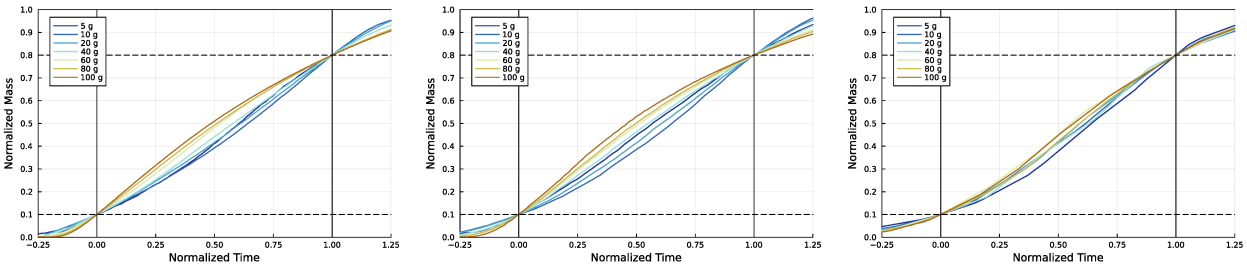

(a) f =30 Hz (b) f =45 Hz (c) f =60 Hz

Figure 5.17: Normalized plot for different actuation frequencies, it is possible to appreciate the reduction of the maximum spread at higher frequencies.

quency and the total duration of material transport. Establishing a relationship between these variables could be useful in managing the mass flow transported by the conveyor in real use case scenarios, as it would allow the bulk flow to be controlled by adjusting the actuation frequency of the piezoelectric actuator through a simple control systems.

As in the previous chapter, for this analysis it is useful to normalize the acquired data to make it easier to compare the experiments carried out with different configurations and to highlight the influence of different parameters on the transport behavior. In this particular scenario, it is still useful to normalize the discharged mass over time recorded by the scale with the initial sample mass of that particular experimental configuration, which implies that, independently of the real value of the sample mass, all the experiments will present a normalized discharged mass that will go from 0 to 1 over the course of the discharging phenomena. Figure 5.18 presents all of the runs in the same plot without any other kind of normalization or scaling on the x-axis. The different discharge curves are color coded based on the experimental actuation frequency, with values going from lower to higher frequencies corresponding to colors going from warm to cold respectively. Given that the time axis in this plot has not been yet scaled or normalized it is possible to appreciate the high variability of the total discharge time observed for various configurations, going from less than a couple of seconds for the faster ones to more than two minutes for the bigger and slower configurations. In general lower frequencies, highlighted by reddish colors, seem to be linked to longer transport time while the opposite is true for high actuation frequency, whose discharge patterns are squashed on the left side of the plot and drawn with colder hues.

In this chapter, however, the time data, acquired in seconds starting from the switching on of the piezoelectric actuator, will not be normalized as in the previous chapter, but will be scaled by multiplying it by the actuation frequency in Hertz (s^{-1}) to obtain a generic dimensionless unit for the time axis. This scaling process will make it so that all of the acquired discharge patterns will be stretched along the x-axis based on their actuation frequency. The ones characterized by a higher vibration frequency will then be stretched more compared to the one with a lower actuation frequency. This kind of plot should make it easier to highlight the influence of the frequency on the material transport speed since, if the frequency will prove to be linearly linked to the total transport time, this scaling process should make all of the different discharge patterns more or less overlap each other.

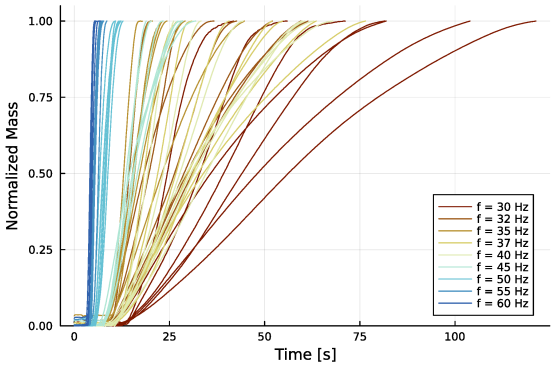

Figure 5.18: All the average experimental mass normalized discharge curves color coded based on the actuation frequency

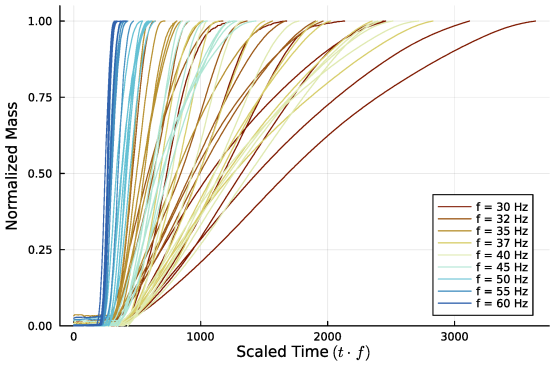

Figure 5.19: All the average experimental mass normalized discharge curves with time scaled with the frequency

Now that all the different runs have been normalized to have a maximum value of 1, we can proceed with the frequency scaling on the time axis. The results are shown in Figure 5.19. As expected from the scaling process, the x-axis range is significantly expanded, and the plots are stretched along this new unit-less time scale based on their actuation frequency. Upon first glance, it is evident that the linear scaling with frequency did not successfully reveal a clear relationship with the transport time. Although the curves obtained with high vibration frequencies have progressed along the x-axis and are approaching the bulk of the other data curves, a simple power scaling of the frequency was insufficient to align all the different discharge curves. This suggests that if there is a relationship between actuation frequency and transport time, it may be associated with a higher power of the frequency or a combination of this parameter with other relevant factors such as the vibration amplitude.

It is indeed important to remember that, as already presented in Chapter 5.3, the experimental setup had a major flow that limited the scope of this parametric analysis, as the trough vibration amplitude was inextricably linked to actuation frequency. It is thus impossible to extrapolate a clear relationship for the frequency from the acquired data, since the vibration amplitude had a strong influence on the transport behavior, as was also presented in the theory in Chapter 3.3).

Based on these observations, it can be concluded that the actuation frequency of the vibrational conveyor has a relationship with the transport time that is higher than linear. In other words, changing the vibrational frequency does not result in a proportional change in the transport time and speed of the bulk material. This finding has implications for the development of control systems for such transport mechanisms and warrants further investigation since it highlights an interesting possibility for future research in this field.

5.4.4 Steady state mass flow

This next chapter will focus on the study of the evolution of the mass flow over various actuation frequency. The mass flow represents the amount of bulk material, in grams, that is discharged by the trough on the scale over each second and is one of the main design parameters in the design of vibratory conveyors, since it is used to determine how much mass is supposed to be transported at any given time, having important repercussion on the sizing, power requirement

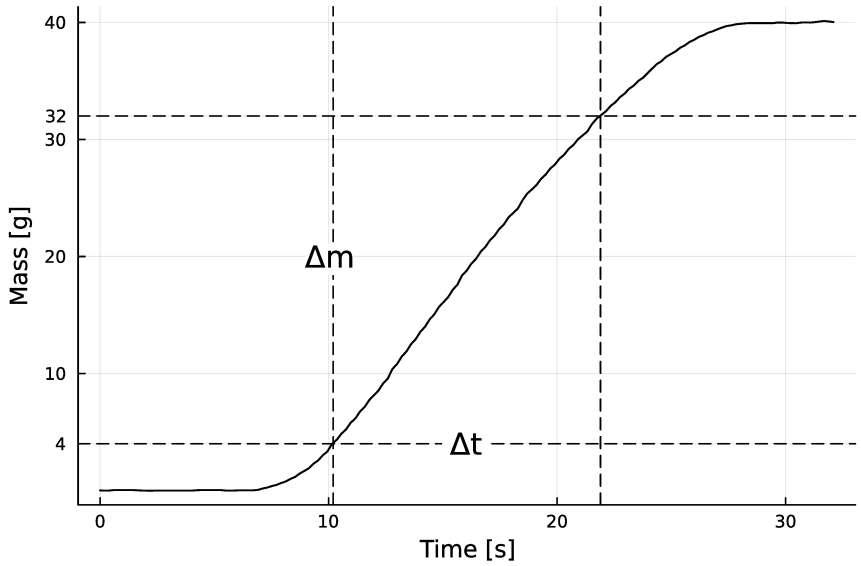

Figure 5.20: Example of a discharge curve, the quantities Δm and Δt are highlighted

and feeding of these systems. To calculate the mass flow, it is possible to utilize the data obtained from the scale, which provides instantaneous measurements of the mass present on the instrument plane at specific time intervals, by computing the discrete first derivative of the recorded mass, representing the change in the amount of material on the scale over time.

$$\dot{m}(\tau) = \frac{dm(\tau)}{d\tau} \tag{5.17}$$

Like previously mentioned, the focus of this work will be the analysis of the central part of the discharge envelope, which can be considered to be representative of a system working in quasi-steady state condition. Thus, this central section is the one that will be considered in the computation of the average mass flow, ignoring the leading and trailing transient tails, as in Figure 5.20.

The upper and lower limits for the central part of the discharge curves to be used in the computation of the average mass flow were chosen as follows: the first 10 % and the last 20 % of the total discharged mass is ignored. These limit values were chosen, a posteriori, in a way to consider the most linear central part of all the wildly different discharge patterns, thus excluding the strongly non linear behaviors observed on the transients. The asymmetry of the position of these two limits is due to the fact that the results obtained by the DEM simulation on a similar configuration presented long tails that had to be excluded to be able to correctly correlate the simulated results with the experimental ones.

With these assumptions in place, it is possible to proceed with the analysis. A script was used to analyze each experimental run, considering all six runs conducted for each configuration. The script calculated the time interval, denoted as Δt, required to discharge the central 70 % of the sample mass, corresponding to Δm grams, as was previously defined. An example of these values can be seen in Figure 5.20 where, for an initial sample mass of 40 g, the time Δt between the data points corresponding to 4 and 32 g respectively, was measured. These two mass values corresponds to 10 and 80 % of the total mass.

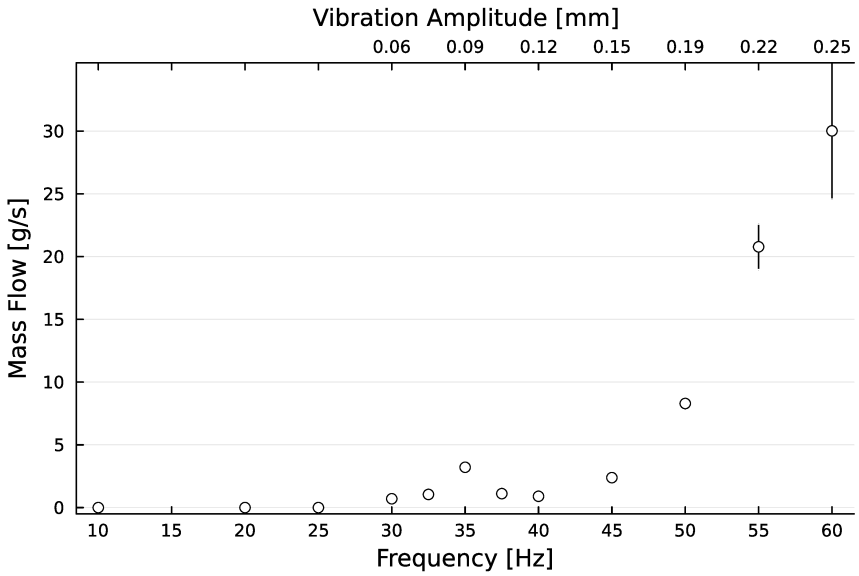

Figure 5.21: Evolution of the average mass flow over the tested range of frequencies for a sample mass of 40 g, the error bars indicate one standard deviation. In some points the error bars are not visible since they happen to be smaller than the marker.

The values here extracted are then used to compute the average mass flow over this central part of the discharge curve by simply dividing the mass discharged Δm by the time Δt:

$$\bar{\dot{m}} = \frac{\Delta m}{\Delta t} \quad [\mathrm{g\,s^{-1}}] \tag{5.18}$$

This process was repeated for all of the runs resulting in a comprehensive dataset of mass flows, one for each experimental configuration tested during the parametric study. Since the main driver of the transport phenomena in this analysis is the actuation frequency, being the parameter that is more easily changeable at a control level, it was chosen to study the evolution of the average mass flow over different frequencies, while keeping the sample mass the same.

The results for a sample mass of 40 g are presented in Figure 5.21, where the mass flow is expressed as a function of both frequency and amplitude. It is important to note again here, that these two variables are intrinsically linked due to a flaw in the experimental setup that makes it impossible to change one without the other. The mass flow values obtained from the six runs of each experimental configuration were used to calculate the mean and the standard error. These statistical measures are presented in the plot shown in Figure 5.21, with circles for the mean data points with their respective error bars.

A first important consideration is the fact that not all of the tested frequencies led to successful transportation of the material up to the end of the trough. For all the tested frequencies lower than 30 Hz no transport was observed. In particular, with these low frequencies, the bulk material was observed to only distribute across the trough without ever reaching the edge of the conveyor. The first data point at which some kind of transport, albeit slow, was observed, was at around 30 Hz for all of the tested sample masses. It would be interesting to further experiment with this particular excitation regime to fine tune the particular frequency at which transport starts to happen.

It is now possible to focus on the more interesting part of the graph, were transport was indeed observed. While it is easy to see a definite upward trend for the average mass flow, which tends to increase more than linearly with the frequency, it is also important to notice the peak located at around 35 Hz. This peak was noticed early on in the experimental phase and was one of the first clues that led to the discovery of the amplitude-frequency relationship in the experimental setup. This particular frequency region corresponds to higher mass flows than all the other around it, so it was assumed that it could correspond to a mechanical resonance frequency of the conveyor setup. This hypothesis could explain the increased throughput of the conveyor, since energy transmission is higher near resonance zones. This make this particular excitation regime a common choice for vibratory conveyors, as presented by Rade et al. [26]. The mechanical resonance hypothesis was further consolidated by some qualitative observation that were made during the experimental campaign. In particular, while working in this specific frequency range, the typical vibration sounds became much louder and the desk, acting as a fixing point for the experimental setup, was subjected to much stronger vibrations.

Considering that the observed peak in the mass flow plot is likely caused by a mechanical resonance of the setup, it is reasonable to expect a second peak at approximately double that frequency. However, further investigation of this second resonance peak was not possible within the experimental range, as vibrations became too strong at frequencies beyond that point which could, indeed, confirm the presence of another resonance zone. The presence of this resonance peak could also help to explain the strong correlation between actuation frequency and vibration amplitude since the mechanical interaction between the leaf springs, trough body, and actuator may result in different vibrational responses of the system at various frequencies. That is why the vibrational amplitude analysis was conducted, with the help of a high speed camera, as presented in Chapter 5.3.

To proceed and compare the same results presented in Figure 5.21 with the ones obtained with different sample masses, all the experimental data was once again normalized by dividing the mass flow by the initial sample mass of each experiment. This process produces a "dimensionless mass flow" that can be interpreted as a *mass fraction* flow. In other words, the new normalized data points indicates the fraction of the total initial mass is lost per each second of discharge. This simple scaling process makes it possible to plot and compare all of the results in the same graph. Furthermore it should help to highlight if the total sample mass plays an important role on the transport behavior or if its effect is negligible up until a certain threshold. All the results thus obtained are presented in Figure 5.22.

It is interesting to see how all of the different lines tend to follow the same trend, with all of them having a more or less pronounced local maxima at around 35 Hz and then following a strong increase in the mass fraction flow as the frequency increases. This seems to indicate that the effect of the sample mass is indeed negligible, at least for the values tested in this experimental campaign, since experimental lines with different total masses follows more or less the same path. From the graph it can also be noted that the smallest tested sample mass, of only 5 g, seems to be diverging from the other ones at higher frequencies maybe indicating the start of a new "low-mass" regime where the behavior could be different. It is however important to remember that all of these measurements have an error that has not been presented in the graph as to not overcrowd it. As could be seen in the previous example of Figure 5.21, the error tends to increase at higher frequencies and it would be reasonable to expect the same from the other configurations, making

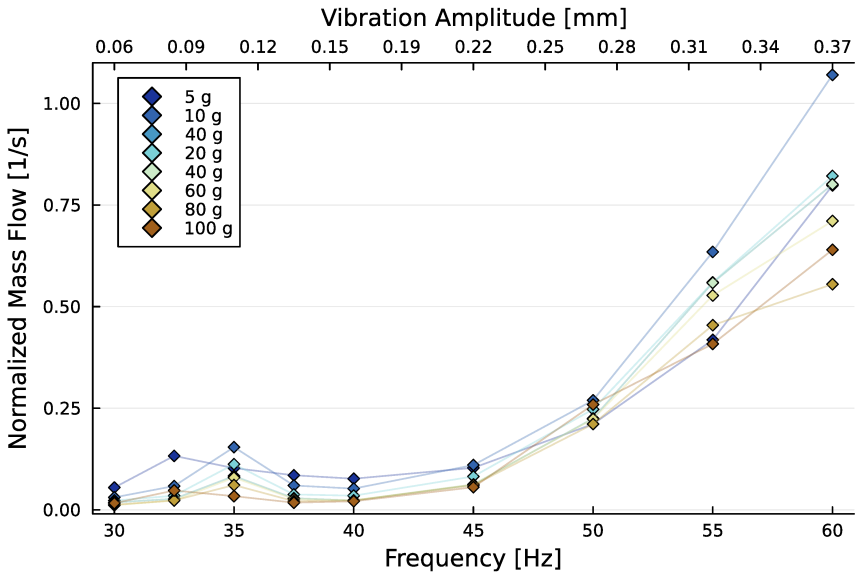

Figure 5.22: Comparison of the different scaled mass flows over the experimental frequency range

it more difficult to determine exact differences between the runs. The standard errors, from the original 6 runs of each experiment, are presented in Figure 5.23 were, as expected, it is possible to appreciate a strong increase in the error at higher frequencies. At the same time, it is reassuring to see really small errors on the lower actuation regimes confirming the quality of the presented data, that will provide a good reference point for the simulations.

5.4.5 Upward transport capabilities

In addition to all of the previous analysis, an interesting topic that was considered during the parametric experimental study was the upward transport capabilities of the vibratory conveyor. Meaning the ability of the setup to transport material against gravity along an incline, determined by the angle α. The setup was prepared using the previously presented 3D printed supports (see Figure 5.6) that were mounted on the conveyor as to ensure an angle of 5° with respect to the horizontal desk. With this inclined setup the transport experiments were conducted following the same procedure presented in Chapter 5.4.1, with the desired amount of material being placed on the last 50 mm of the trough.

Early tests showed the need of a higher frequency range to ensure transport, that is why the parametric study for the inclined setup was carried out on the following configuration points:

$$f = [10, 20, 25, 30, 32.5, 35, 37.5, 40, 45, 50, 55, 60, 65, 70]\text{Hz}$$
$$m = [10, 40, 60]\text{g}$$

The data has been gathered and analyzed using the same methods presented in the previous chapter but the focus, here, will be the analysis of the measured mass flow, since it is of primary importance in the design of logistical systems that must operate against gravity. The mass flow was measured from the discharge curves following the same procedure applied on the horizontal setup. The central part of the discharge patter, between the 10 % and the 80 % of the total mass, was considered for the computation and Equation 5.18 was employed again to obtain a numeric

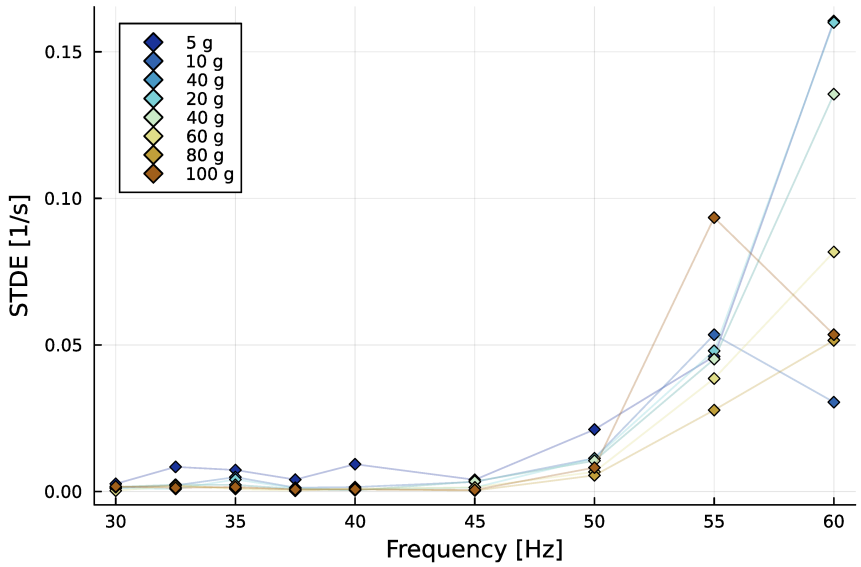

Figure 5.23: Evolution of one standard deviation for different sample masses over the range of experimental frequencies

value for the average mass flow. For ease of comparison the mass flow was, also in this case, scaled by the initial sample mass of each particular experiment obtaining, again, an indication of the mass fraction flow.

The results of these analysis are presented in Figure 5.24 and 5.25, for the normal and scaled mass flow respectively. Contrary to what had been observed in the experiments conducted with the horizontal setup, the first occurrence of material transport appears at around 35 Hz. Furthermore it is interesting to see how the mass flow stays really low up until 45 to 50 Hz, after which it starts increasing rapidly. From Figure 5.25 where the scaled mass flows are presented, it is interesting to note how, also in this case, all of the lines seems to follow pretty much the same trend up until 65 Hz after which the configuration with the biggest sample mass, of 60 g, shows a noticeable dip in scaled mass flow. Apart from the last important dip, the curves shows a good agreement between each other confirming the low effect of the total mass on the conveyed mass flow. During the experimental campaign, visual inspection of the material flow confirmed that there was a noticeable difference in mass flow for larger amounts of material. Specifically, when a larger mass was present in the trough, it became more challenging for the conveyor to transport the material to the edge. It seemed as though the weight of the bulk material on top produced pressure on the material below, likely due to the increased powder bed height in this configuration, limiting its movement. On the other hand, the 10 g configuration, despite having the lowest absolute mass flow, consistently exhibited one of the highest scaled mass flows across the entire frequency range. This can be attributed to the fact that the bulk material had more freedom to distribute itself along the trough, limiting particle interactions and the accumulation of material.

From these considerations it is possible to deduce some useful information about the parameters that influence the vertical transport capabilities of a vibratory conveyor. Firstly to achieve the same mass flow as in the horizontal configuration it is necessary to actuate the conveyor with a higher vibration frequency. It was in fact noted that, in general, to achieve the same scaled

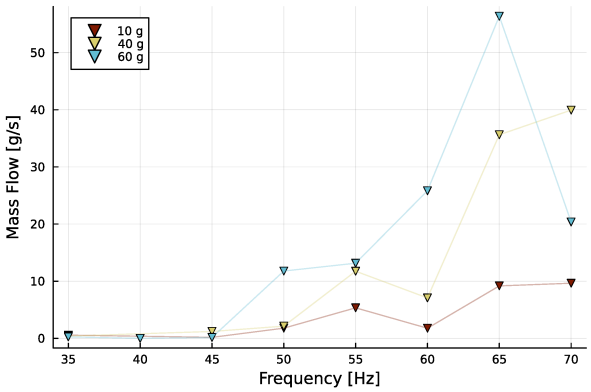

Figure 5.24: Measured mass flow at different frequencies for α =5°

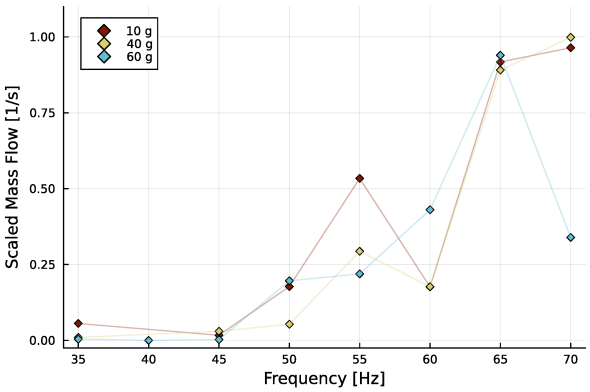

Figure 5.25: Scaled mass flow at different frequencies for α =5°

mass flow as the one observed in the horizontal configuration the actuation frequency should have been increased of around 5 to 10 Hz. Moreover, it was observed that the mass present in the trough during transport had a significant impact on the behavior of the material. When there was a larger amount of material, the weight produced on the particles positioned lower along the trough became substantial, making it challenging for them to move forward. This resulted in a noticeable decrease in mass flow, particularly for the highest mass configuration of 60 g at the frequency of 70 Hz. It is also important to note that for this second case of the inclined conveyor the vibration amplitude, that was observed to be linked to the actuation frequency in the horizontal configuration, was not measured experimentally. It is not known if the new inclination of the setup has any influence on the amplitude of the oscillations with the changing frequency but, considering the inertia forces at play, some differences to the horizontal case are to be expected due the newly added effect of gravity along another component of the vibration motion.

Another interesting thing to analyze is the influence of the β angle on the upward transport capabilities. This angle is described as the angle between the actuator direction and the horizontal and is changed, in the experimental setup, by modifying the inclination of the piezoelectric actuator through the use of some nuts and bolts. The angle between the actuator and the leaf spring was kept at a constant 90° to ensure the best possible movement transmission, as to not overload the actuator. To ensure this alignment, the leaf springs were also loosened up and set to the new angle for each configuration.

As presented in the theory of vibrational conveyors, the angle β influence the magnitude of the vibration components that are transmitted to the particles in the trough. While usual values of this parameter are between 30 and 40° it is possible to use higher or lower values for this angle, meaning that the particles will receive a more or less vertical force during the vibrating motion. In general, it is necessary to find the right angle for each specific application, that is why this parametric study was conducted. The experimental procedure was the same as in the previous cases, the range of parameters covered were:

$$f = [10, 20, 30, 35, 40, 45, 50, 55, 60, 65, 70]$$
$$\beta = [20, 30, 35, 40, 50]$$

obtaining the results presented in the heatmap of Figure 5.26 were the color is based on the mass

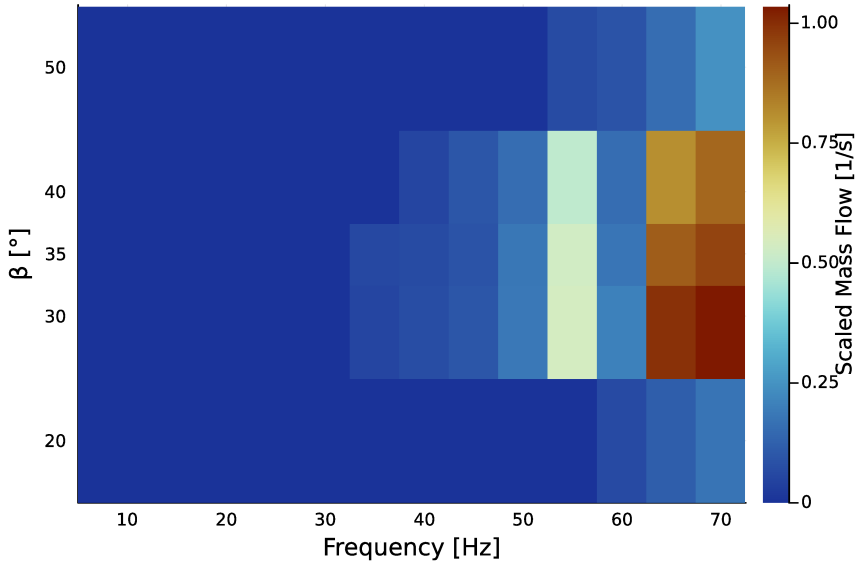

Figure 5.26: Heatmap of the mass flow obtained for different β and frequencies

flow computed as before. All of the runs were made with a sample mass of 10 g.

As expected, the highest mass flows are obtained for higher frequencies and in what is considered to be the optimal range for β, between 30 and 40°. When testing with a too high, or too low, β angle the mass flow is greatly reduced even at really high frequencies, not being able to reach even half of what is achieved with β =35°. It is also possible to appreciate a peak in the mass flow for a frequency of 55 Hz which is present in the central values of β but is lost for the most extreme ones, probably due to noticeable changes in the overall vibratory response of the structure.

Chapter 6

Validation of the model

This chapter will be focused on showing a series of comparison between simulated, experimental, and analytical results, to evaluate the performance of the numerical model in predicting what is observed in a real experimental setting. This validation process is a crucial step in ensuring that the numerical model that had been developed so far can actually be used as a predictive tool, producing results with a close match with reality. These comparisons will be useful to understand what are the main problems and limitations of the DEM model, providing a way to evaluate the uncertainties ranges that should be expected when using this new numeric instrument to predict the performance of real vibratory conveyors.

The performance evaluation of the DEM code will be conducted in several stages. Firstly, the simulation results will be compared with analytical results obtained from simple configurations, including scenarios such as a bouncing ball or a disc rolling down an incline. This will serve as an initial benchmark for assessing the accuracy and reliability of the simulation in reproducing known scenarios. Next, the focus will shift to a more experimental approach by comparing the measured transport speed with the simulated results. This analysis will provide valuable insights into the ability of the DEM code to accurately capture the dynamics of many-particle movement and transport within the system. Finally, the most crucial aspect of the evaluation will involve comparing the discharge curves and mass flows obtained from both the experimental measurements and the simulation.

6.1 Comparison with simple analytical cases

The first step in validating the whole discrete element simulation model is to make sure that the underlying numerical solution is correct and stable within acceptable margins. To do so it is useful to simulate some simple cases such a simple bouncing ball, with and without damping, or a ball rolling down an inclined plane. This initial study cases present a simple analytical model that can be used as a reference to evaluate the predictive performance of the numerical solution developed in Section 4.

6.1.1 Perfectly elastic bouncing ball

The simplest discrete system that can be considered as a test of the reliability of the numerical method is a simple bouncing ball that is falling without air resistance due to gravity acceleration. This system can be even considered as a one dimensional problem, if we assume that the ball is bouncing in place. From simple kinematics it is known that the vertical falling motion of the ball z, plotted against time t, will result in a parabola. The bounce on the floor will happen when the condition $z - R = 0$ is met, where R is the radius of the ball in question. For this example a perfectly elastic response has been considered, with the ball conserving its total energy, and thus speed, upon collision with the floor. It is easy to see how the ball should reach, at every bounce, the same maximum height due to the lack of dissipation terms.

Given the analytical example, a simple simulation was ran with a particle of radius $R = 1\,\text{mm}$ bouncing on the bottom boundary of the simulation domain without any damping, starting from a height of 10 mm. Following the considerations in Chapter 4.4.1, the integration time step was set at $\Delta t_{sim} = 0.730\,\text{ms}$, and the simulation was evolved for a time length of 1 second, using an elastic constant of $k_n = 3330\,\text{N m}^{-1}$. The result for a perfectly elastic response are presented in Figure 6.1 where the trajectory of the ball computed by the DEM simulation and by the analytical model are compared. There is a good agreement between the two trajectories, indicating that the numerical model can predict, with good accuracy, the trajectory that is expected from an ideal ball bouncing in a perfectly elastic manner on a fixed surface. The comparison between the trajectory obtained with the DEM simulation and the analytical one as a reference, offers a RMSE (Root Mean Squared Error) of:

$$RMSE = \sqrt{\frac{1}{n_{ts}} \sum_{t=0}^{t=1} (z_{DEM} - z_{an})^2} = 0.122\,\text{mm} \tag{6.1}$$

Another observable quantity that can be used as a reference of the goodness of the simulation's results is the *total mechanical energy* of the system. In this simple case, the system is composed of a single non-rotating particle, so its total energy should be constant throughout the simulation evolution, and equal to the sum of its potential and kinetic energy components:

$$E_{tot} = E_{kin} + E_{pot} = \frac{1}{2} m v^2 + mgh = 1.0889 \times 10^{-6}\,\text{J} \tag{6.2}$$

The evolution of the energy is showed in Figure 6.2 where it is possible to see some slight variations as time passes. The graph of the energy shows some steps where the energy changes in a discontinuous way. These discrete steps corresponds to each collision of the particle with the floor. The slight variations in total energy are due to the intrinsic numeric approach of the method, since collisions are really fast phenomena it is difficult for the integrator to precisely analyze them using discrete time steps. It is possible to observe some straight lines going down at the beginning of some steps in the graph. Those are the timestep at which the the integrator analyzed the particle near its maximum penetration depth, when the particle is almost still and is starting to be accelerated out of the floor. Nonetheless the variations of the energy are still really small in comparison to the initial value and they definitely lie inside the uncertainty due to other limitations of this simulation approach. In fact, it is possible to see that the maximum energy variation, in this example, has a value of $1.04 \times 10^{-8}\,\text{J}$ resulting in a relative error of 0.952 %.

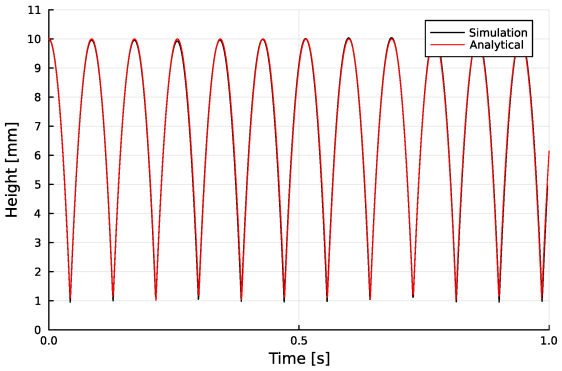

Figure 6.1: Comparison between DEM results and analytical description of a purely elastic bouncing ball. The model offers good accuracy in the prediction of the motion

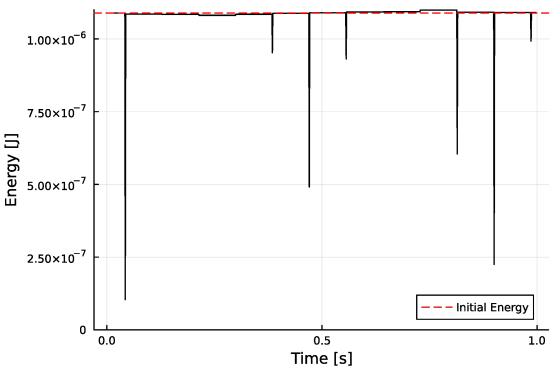

Figure 6.2: Evolution of the energy during the simulation of a bouncing ball

6.1.2 Partially inelastic bouncing ball

The next logical progression from the previous simple scenario involves the inclusion of a *normal damping*, proportional to the impact velocity of the particle. It would be beneficial at this point to refer to Chapter 4.3.4 for a mathematical explanation and numerical implementation of this technique. The fundamental concept is to introduce an additional force, independent of the elastic response, that acts during the collision. This supplementary force, known as damping, will cause the particle to decelerate and lose a proportion of its energy, resulting in a decrease in the height attained by each successive bounce. The magnitude of this damping force is computed using the *normal damping coefficient* denoted by D. This coefficient is typically computed using empirical formulas [8] [48] [38] that are typically based on the mass of the particles m, the normal elastic coefficient k_n, and the coefficient of restitution e. The formula proposed by Ting et al. [38] was chosen for this model:

$$C_n = -2\ln(e)\sqrt{\frac{k_n m}{\ln^2 e + \pi^2}} \tag{6.3}$$

The values for normal elastic coefficient and the mass of the particle were kept the same as the ones used in the previous chapter for the perfectly elastic bounces, while the newly introduce coefficient of restitution is yet to be evaluated. This coefficient, as previously said in Chapter 4.3.4, is defined as the ratio of the final to initial relative speed between two object in a collision and, for typical inelastic collision, it ranges from 0 to 1, where 1 would be a perfectly elastic response. This coefficient proves to be difficult to evaluate, and typically depends on many factors such as material pair, shape of the objects, impact velocity and direction. For the purpose of this simulations a value of 0.6 was used, following the results of previous simulations and measurements by Mishra et al. [49] done on quartz particles of similar dimensions to the one considered here.

The results of the simulation are presented in Figure 6.3 and 6.4 where it is possible to observe both the evolution of the trajectory and of the energy of the system over time. The DEM simulation was run using $e = 0.6$ resulting in a normal damping coefficient of $C_n = 33.82 \times 10^{-3}\,\mathrm{N\,s\,m^{-1}}$ computed using Equation 6.3. In both these graphs the results of the simulation are compared with an analytical solution derived from the use of the coefficient of restitution in its ideal form:

the ratio of the particle speed before and after the impact. As with the previous case, the results confirms the predictive performance of the model, with the two trajectories being pretty much equal. The differences that occurs in the evolution over time can be caused by both the use of the empirical equation for the determination of the damping coefficient, and due to the numerical implementation errors. In any case the results can be considered satisfactory since the maximum deviation from the analytical result has a value of 0.28 mm resulting in a root mean squared error of:

$$RMSE_{z,damp} = \sqrt{\frac{1}{n_{ts}} \sum_{t=0}^{t=1} (z_{DEM} - z_{an})^2} = 0.0386\,\text{mm} \tag{6.4}$$

As for the total mechanical energy of the system, in this case it is possible to observe that it reduces at each bounce due to the effect of damping. It is possible to observe some differences between experimental and analytical results also in this quantity, resulting in a root mean squared error of:

$$RMSE_{En,damp} = \sqrt{\frac{1}{n_{ts}} \sum_{t=0}^{t=1} (E_{DEM} - E_{an})^2} = 1.39 \times 10^{-8}\,\text{J} \tag{6.5}$$

As previously mentioned this variations can be attributed to the discretization of the impacts and to a slightly erroneous evaluation of the damping coefficient due to the use of an empirical formulation.

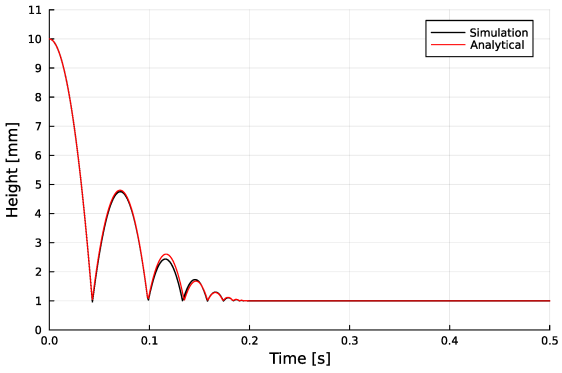

Figure 6.3: Comparison between DEM results and analytical description of a inelastic bouncing ball with a restitution coefficient of $e = 0.6$

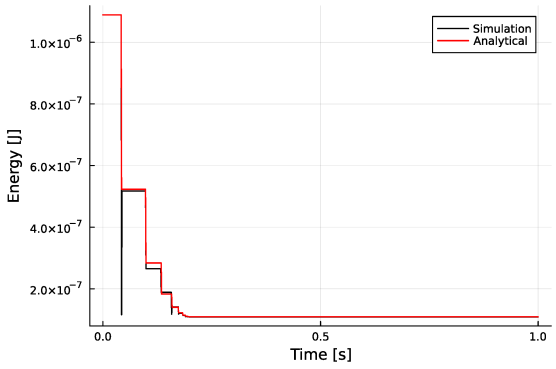

Figure 6.4: Evolution of the energy during the simulation of a bouncing ball with a restitution coefficient of $e = 0.6$

6.1.3 Pure rolling on an inclined plane

The last analytical case, presented in this chapter, will be the case of a particle rolling down an inclined plane in a pure rolling regime. This system is still simple enough to be analyzed analytically while, at the same time, providing another reference for the validation of the rolling behavior of the simulated particles. The dynamics of this example have been already explained in Chapter 2.2, but the main formulas are here recalled for an easier reference. An important quantity describing the rotational motion of any rigid object is its *moment of inertia* I. For the case in question, a rolling sphere with mass m and radius R has its moment of inertia equal to:

$$I_{sph} = \frac{2}{5} m R^2 \tag{6.6}$$

If the ball is considered to be rolling down an incline of angle α, following the mathematical description of Chapter 2.2, it is possible to determine the acceleration of the sphere in a pure rolling regime as:

$$a_{PR} = \frac{5}{7} g \sin \alpha = 610.71 \,\mathrm{mm\,s^{-2}} \tag{6.7}$$

This general formula was used applied to the case in question that considers a sphere rolling down an incline of $\alpha = 5°$ under a constant gravitational acceleration g of $9810\,\mathrm{mm\,s^{-2}}$ resulting in a predicted ideal value of $610.71\,\mathrm{mm\,s^{-2}}$ of downward acceleration.

The simulation was run with the same mechanical parameters of the previous ones but with the addition of a *coefficient of shear friction*, that is necessary to enable the pure rolling motion of the sphere. The value for the coefficient of shear friction was chosen with a high enough value as to ensure a regime of pure rolling, resulting in a final value of $\mu = 0.112\,63$. Obviously, the simulation is evolved in a 2D environment where the sphere is represented by a disc. To make up for the difference, the disc was initialized with a mass and inertia equal to the ones of the sphere, making it completely identical to its 3D counterpart by all mechanical means. It would clearly be possible to use the inertia of a disc, but the result would need to be compared with a different values of analytical acceleration, obtained by updating Equations 6.6 and 6.7 with the new inertia.

Nonetheless, the results of the DEM simulation, presented in Figures 6.5a to 6.5c, show a really good agreement between the analytical acceleration and the simulated one. In the figure it is possible to see how, after an initial zone of high acceleration when the particle is starting to make contact with the floor, the acceleration value rapidly converges to the one predicted by Equation 6.7 showing that the simulation is able to correctly predict the motion of rotating particles. The graphs of position and velocity, being computed by integration of the acceleration values over time, show some slight differences from the predicted values due to the initial simulated high acceleration peak. This is simply due to the couple of initial time steps that are necessary for the simulated particle to penetrate the floor for a sufficient amount. This behavior can be considered to be an intrinsic characteristic of the force-displacement law implemented in the DEM code. It could be possible to get better results by decreasing the penetration depth. This can be achieved by both increasing the elastic coefficient, as shown in Chapter 6.1.1, and by reducing the integrator time steps, producing a longer computation time for the same simulation.

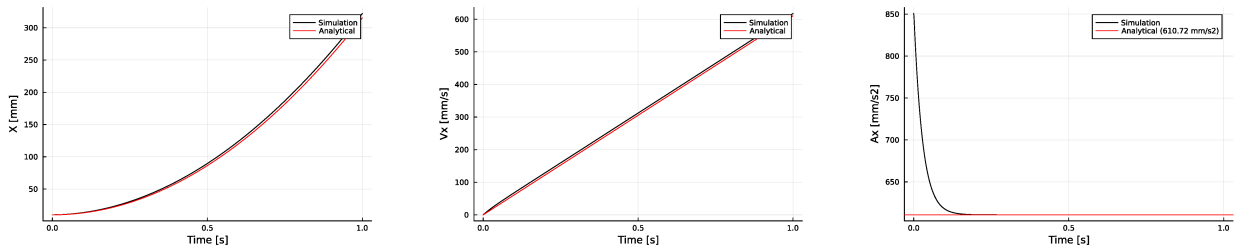

(a) Position (b) Velocity (c) Acceleration

Figure 6.5: Comparison over time for a ball rolling down an incline, DEM results (black) and analytical prediction (red)

6.2 Inclined plane experiment

Once established that the simulation and its numerical model are working as intended, as demonstrated by the comparison with known analytical problem, it is possible to start comparing the results of the simulations with real life data acquired through the experimental setup presented in Chapter 5.1. Following the same approach as in the previous chapter, it is useful to start analyzing simple system with just one particle. In particular, this chapter will focus on the comparison between the results of the DEM simulation and experimental data of a single particle rolling down the inclined trough of the experimental setup.

The experimental reference data was the same obtained in Chapter 5.2.3 where single particles were made to roll down the inclined trough to evaluate the rolling friction coefficient to be implemented in the simulation, available in Table A.1 and A.2. The scope of this chapter is to compare the time it takes for the particles to roll down the whole incline in the DEM simulation with the data acquired on the experimental setup.

Now that is necessary to show the comparison between simulation and experimental data it is necessary to employ all of the coefficients found through the calibration experiments showed in Chapter 5.2. In particular, the values used are presented in Table 6.1. The density was chosen based on a known value for the density of quartz, while the diameter of the sphere was set to the same as the ones used during the experimental phase, 200 µm. The normal elastic coefficient was chosen as to grant a penetration length between the particle and the surface that is less than 1 % of the particle diameter, in this case resulting in about 2 µm of maximum penetration. The shear friction and rolling friction coefficients values are the ones obtained during the experimental phase, while the normal and shear damping coefficients were derived using the empirical formula presented in Equation 6.3, derived from papers by Ting and Corkum [38] and Ting et al. [8].

Table 6.1: Coefficients used in the validation simulations

Parameter	Value	Unit
Sphere diameter (D)	200	µm
Density (ρ)	0.002 65	$\mathrm{g\,mm^{-3}}$
Normal elastic coefficient (k_n)	3300	$\mathrm{g\,s^{-2}}$
Shear friction coefficient (μ)	0.1126	$\mathrm{g\,s^{-2}}$
Cohesion (C)	5.83	$\mathrm{g\,mm\,s^{-2}}$
Shear angle (Φ)	6.43	°
Rolling friction coefficient (μ_R)	0.618 53	-
Restitution coefficient (e)	0.6	-
Normal damping (D_n)	0.012 23	$\mathrm{g\,mm^{-2}\,s^{-1}}$
Shear damping (D_s)	0.012 23	$\mathrm{g\,mm^{-2}\,s^{-1}}$

The simulation's initial condition were set with a single particle generated right above the bottom surface, without any initial velocity, with a trough downward inclination of respectively 5 and 10 degrees. The particle is left free to roll down the incline, under the influence of gravity, until it reaches the edge of the trough where the total travel time is recorded. just like for the real experimental setup, the length of the trough in the simulation was set to 250 mm. The simulation was run numerous times to prevent possible numerical deviations from one run to the others, obtaining some really stable results that seemed to perfectly overlap within the expected error

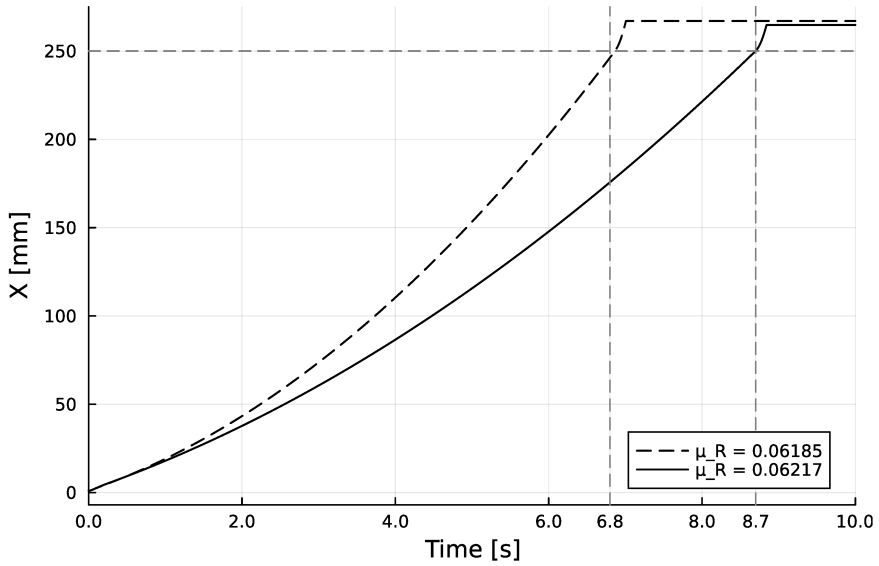

Figure 6.6: Comparison of the results of the tilted plate simulation. The time to discharge with the corrected coefficient of rolling friction is the same as the one observed experimentally

bands (deviations $<1 \times 10^{-3}$ mm).In the experiments the glass particles travel along the whole length of the trough in around 8.7 s for a downward inclination of 5°. On the other hand the simulation data, obtained for the same conditions and plotted with a solid line in Figure 6.6, resulted in an average travel time of 6.8 s, highlighting a difference of 1.9 s between the experimental and simulated results. To account for this difference, the rolling friction coefficient was progressively increased through a multiplicative factor until the simulated travel time matched the one obtained in the experiments. The final value of the rolling friction coefficient that granted the same travel time turned out to be $\mu_R = 0.062\,16$, corresponding in an increase of around 0.5 % with respect to the original value. The results of an example run computed using the newly found coefficient can be seen in Figure 6.6 in a solid black line, where it is possible to appreciate how the simulated travel time corresponds quite exactly to the 8.7 s measured during the experimental phase.

This initial comparison between the simulation and experimental results was a key step in the correction of this parameter and provided a first assessment of the real predictive performances of the model. Once the corrected coefficient was implemented, the simulation's results perfectly aligns with the experimental times confirming that the model can be trusted for the analysis of this kind of problems. Furthermore, this comparison shows how even a seemingly simple experiment, such as the one presented in Section 5.2.3 for the evaluation of the rolling friction coefficient, was able to provide a value that deviated of only 0.5 % from the one that had to be used to correctly calibrate the simulation.

6.3 Transport speed comparison

In order to further validate the simulation results with experimental data, a set of simulations with a high number of particles was performed to create a benchmark for the evaluation of the simulated transport behavior. The first analysis of the results, here presented, has been done through the comparison of the mean transport speed of the bulk material at a given vibration

frequency with the one measured experimentally.

As previously mentioned in Section 5.4, all the transport experiments were also captured with the help of a camera placed directly above the experiment so as to frame the entire length of the trough. This setup made it possible to acquire video footage of the sample material being transported along the trough for different vibration frequencies. As for the data extraction itself, *Tracker* [46] was again used to analyze the movement, over time, of the forward front of the moving sample mass. For this particular setup the X-axis of the software's internal system of reference was aligned to the center line of the conveyor's trough while a measuring stick, previously aligned to the trough and visible in the video, provided a reference distance to calibrate the position extraction process. The tracking of the forward front of the sample material was completed employing the autotracking feature of the software that made it possible to automate this process for each of the analyzed video sources. From the position data, it was then possible to extract the movement speed of the bulk material along the trough axis, through the application of a simple finite differences algorithm.

Since simulating a lower number of particles proved to be easier in terms of time and computational resources, the speed comparison were made with the lower experimental mass possible. During the video analysis it was noted that sample masses lower than 20 g were difficult to track with the software, given that they evolved in an elongated and dispersed shape along the trough. That is why the experiments with a sample mass of 20 g were used as reference for the evaluation of the transport speed, given that they provided the minimum possible mass while ensuring a stable tracking procedure. An example of the position tracking along the trough can be seen in Figure 6.7, the red diamond markers highlight the position of the forward front of the bulk material over time. In the same image it is also possible to note the presence of the measuring stick used as a dimension reference. Given the chosen mass of bulk material, the transport experiment was repeated for the usual set of experimental frequencies presented in Chapter 5:

$$f = [30, 32.5, 35, 37.5, 40, 45, 50, 55, 60]\text{Hz}$$

A velocity plot was obtained for each one of these cases describing the evolution of the transport speed overtime. Given the low contrast of the video frames, the vibrations of the trough, and the dispersion of the bulk material during transport, the position extraction and the subsequent speed computation presents high oscillations as can be seen in Figure 6.8. To obtain a more useful value the average value of each sample set was computed, as can be seen in the same figure, indicated with a red line. This process was repeated for all of the frequencies, obtaining the evolution of the average transport speed as the frequency, and amplitude, of the vibration changes. It is indeed important to remember again, as noted in Chapter 5.3, that this particular experimental setup presented a strong dependence of the vibration amplitude with the actuation frequency, so all of the measured quantities depends on the evolution of both these parameters.

Figure 6.9 illustrates the variations in the experimental average transport speed values, as black circles, in response to changes in frequency and amplitude. This figure provides a clear visual understanding of how the transport speed is affected by changes in the oscillatory motion parameters. It is possible to observe a visible peak at about 32.5 Hz followed by a segment of almost constant transport velocity of about 20 mm s^{-1}. A final zone is observed, for actuation frequencies higher than 40 Hz, where the transport velocity continues to increase, reaching values above 100 mm s^{-1}. This behavior may be related to the mechanical resonance frequencies of the ex-

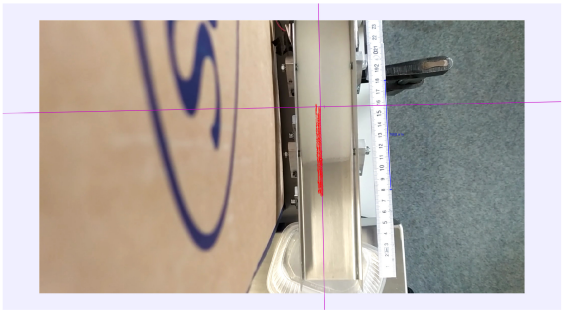

Figure 6.7: Example of the video analysis process in Tracker, the red diamond markers highlight the position of the bulk material's front over time

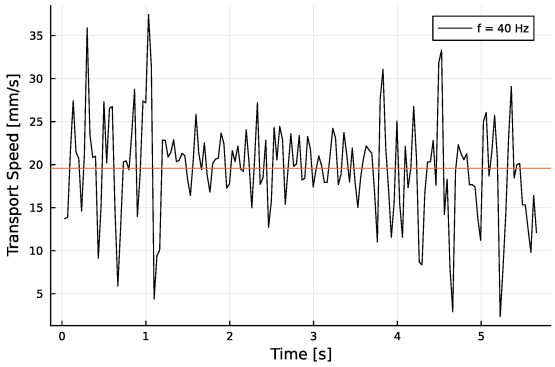

Figure 6.8: Transport speed of the bulk material in the trough, extracted with Tracker, with a vibration frequency of 40 Hz. In red the mean value of the sample

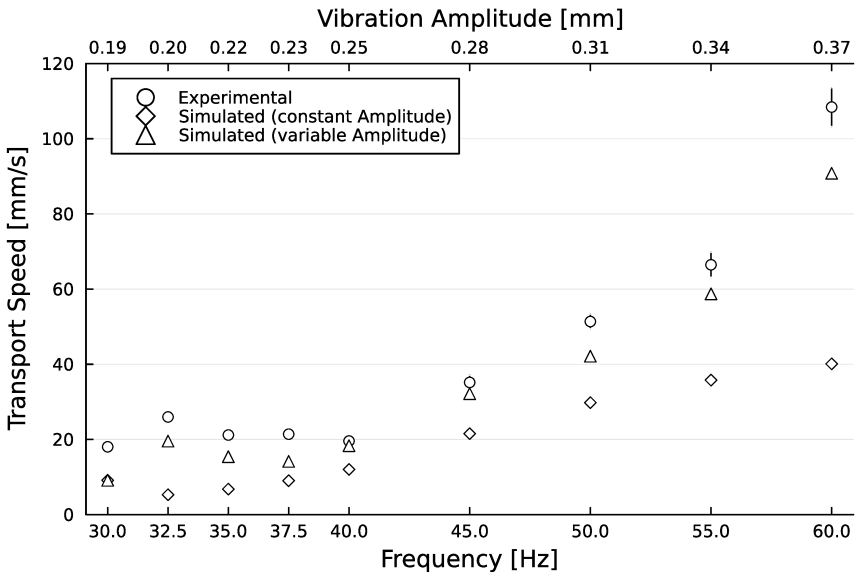

Figure 6.9: Comparison of experimental and simulated transport speed over different frequencies (and amplitudes)

perimental setup when excited with sinusoidal waves. To further support this assumption, it is useful to note that the first peak for the transport velocity occurs at about 32.5 Hz, so it would be reasonable to expect another peak at twice that frequency which could be confirmed by the evolution of the transport velocity with higher frequency. The strong increase of the velocity, visible in Figure 6.9 for frequencies higher than 45 Hz, could be linked to another peak in the range of 65 to 70 Hz, which has not been studied experimentally, precisely because of the too intense vibrations that occur on the whole setup in this actuation regime. It then seems justified to associate these peaks with the presence of mechanical resonance frequencies in the experimental frequency range.

The experimental values also present an error bar that was computed from the data acquired on Tracker. For each set of measurements, each one at a different frequency, the 95 % confidence interval CI was computed from the standard error SE as:

$$CI = SE \times 1.96 \tag{6.8}$$

Where the standard error SE was computed from using the definition:

$$SE = \frac{\sigma_x}{\sqrt{N}} \tag{6.9}$$

$$\sigma_x = \sqrt{\frac{1}{N}\sum_{i=1}^{N}(x_i - \bar{x})^2} \tag{6.10}$$

Where N is the total number of measurement for each data set, $\bar{x}$ is the mean value of the transport speed for each data set, and x_i is a generic measurement of the data set. As can be expected the amplitude of the confidence interval increases with the transport speed, possibly due to the use of a low frequency camera as the video recording instrument. Fast moving objects in a low framerate video are difficult to track correctly, increasing the overall error of the measurement itself.

Figure 6.9 also contains the results of two simulation sets: the first one was run with variable frequency and fixed vibration amplitude of 0.321 mm, using the value originally measured on the system, while the second set was run with bothe the variable frequency and vibration amplitude, using the data obtained in Chapter 5.3. From the figure, it is clear how the simulations conducted with a constant amplitude fail to reproduce both the first peak and the second part of the experimental curve, where the measured transport speed increases drastically. These simulation results still show a rising pattern for the transport speed at higher frequencies but with a much lower slope than what was observed experimentally, reaching a maximum of about 40 mm s^{-1} for the last actuation frequency of 60 Hz. This erroneous behavior prediction was to be expected since the increase in amplitude with the frequency has a strong influence in the conveyor's transport speed, as was presented in the theory in Chapter 3.3. Using a constant amplitude, will thus result in a high discrepancy between simulated and experimental results.

On the other hand, after the implementation of the variable amplitude, the simulations provided results that were able to match the measured ones much more closely, confirming that this parameter has a high influence in the calibration of the numerical simulation. This new set of simulation's results, indicated by a triangle in Figure 6.9, are able to correctly predict the transport speed peak at around 32.5 Hz, while being also able to describe the strong increase in transport speed for higher frequencies with a much lower error when compared to the reference experimental data.

To compare the two series of data with the experimental one the Root Mean Squared Deviation $RMSD$ was computed between the two:

$$RMSD_{const} = \sqrt{\frac{1}{N}\sum(u_{exp} - u_{sim_{A,cost}})^2} = 28.26\,\mathrm{mm\,s^{-1}} \tag{6.11}$$

$$RMSD_{var} = \sqrt{\frac{1}{N}\sum(u_{exp} - u_{sim_{A,var}})^2} = 8.64\,\mathrm{mm\,s^{-1}} \tag{6.12}$$

In this particular equation, N denotes the total number of measurements to be compared with the reference, which corresponds to the 9 simulations conducted at different frequencies. Additionally, the variable u represents the transport speed that is obtained from either the simulation (u_{sim}) or from experimental measurement (u_{exp}). The $RMSD$ is utilized as a metric to compare the agreement between the simulated and experimental data, where lower values indicates a closer match. The comparison between this two parameters shows how, the simulations with variations on both frequency and amplitude, provide results that are much more similar to the ones observed experimentally presenting a reduction of about 70 % in RMSD. This observations acts as a further point of confirmation and quantification of the importance of accounting for amplitude variations in the calibration process of the model.

6.4 Comparison of transport behavior

The last chapter of this section will be focused on the comparison between the results of complete transport simulations with the observations obtained during the experimental campaign and previously presented in Chapter 5.4. This kind of comparison proves to be really useful in evaluating the performance of the numerical model since it is the only way to really assess the the accuracy of the simulation in predicting the transport capabilities of an equivalent real vibratory conveyor setup. In this specific scenario, the focus will be given to the discharge curves and the discharged mass flow. It is important to note that these analyses take into account the considerations discussed earlier regarding the conversion between the total number of simulated particles in a 2D domain and the actual 3D experimental setup.

By examining the discharge curves, it is possible to assess the ability of the simulation to accurately replicate the behavior of many particles as they are transported along the conveyor. This involves comparing the shape, trend, and overall characteristics of the discharge curves obtained from the simulation and the experimental measurements. Additionally, the discharged mass flow will be the other key metric for evaluating the performance of the DEM code. As previously explained, this parameter represents the amount of material that is successfully transported by the conveyor system over a given time period. Comparing the simulated discharged mass flow with the experimental data will provide insights into the accuracy and reliability of the simulation in capturing the real-world transport phenomena.

The simulations were run with two different amounts of simulated 2D particles, a smaller amount of around 1900 particles and a bigger simulation setup with 3750 discs. Keeping as a reference the conversion presented in Chapter 5.2.1, the two amounts are considered to be the equivalent to a real life quantity of sample material of 5 and 10 g respectively. Since the bulk material used in the experiments was composed of glass spheres of around 200 µm of diameter, the same dimension was used to generate a distribution of mono-sized circular particles in the simulation. Given the

need to simulate a conveyor under Earth's gravity condition, the gravitational acceleration constant in the code was set to 9.807 $\mathrm{m\,s^{-2}}$ [45] oriented along a downward direction. The various mechanical interactions are described using the same values for the coefficients presented in the previous chapter. As previously explained, some of those values were evaluated experimentally, such as the friction coefficient, others were chosen as to grant some kind of expected behavior, such as the the elastic coefficient, while others were estimated using empirical formulas, such as the damping coefficient. The elastic coefficient, in particular, was chosen as to insure a compenetration between particles during impacts that is always lower than 0.1 % of the particles diameter in the typical speed regime observed in the simulation. At the same time, the specific value of the elastic coefficient was used to set the required time step, as seen in Chapter 4.4.1. A review of all the important parameters used in the simulation is shown in Table 6.2. The frequency range was chosen to be the same as the one tested experimentally, from 30 Hz to 60 Hz, while the vibration amplitude was set following the measurements taken on the experimental setup and presented in Chapter 5.3, as a way to achieve a better match between simulation and experiment.

Table 6.2: Coefficients used in the validation simulations

Parameter	Value	Unit
Sphere diameter (D)	200	µm
Density (ρ)	0.002 65	$\mathrm{g\,mm^{-3}}$
Normal elastic coefficient (k_n)	3300	$\mathrm{g\,s^{-2}}$
Shear friction coefficient (μ)	0.1126	$\mathrm{g\,s^{-2}}$
Cohesion (C)	5.83	$\mathrm{g\,mm\,s^{-2}}$
Shear angle (Φ)	6.43	°
Rolling friction coefficient (μ_R)	0.618 53	-
Restitution coefficient (e)	0.6	-
Normal damping (D_n)	0.012 23	$\mathrm{g\,mm^{-2}\,s^{-1}}$
Shear damping (D_s)	0.012 23	$\mathrm{g\,mm^{-2}\,s^{-1}}$
Gravitational acceleration (g)	9807	$\mathrm{mm\,s^{-2}}$
Simulation time step (t_s)	0.232	ms

Some results are shown in Figure 6.10 where the discharge curves are presented for both experimental (in red) and simulated data (in blue). To be able to compare the two results, it was again necessary to scale them. The scaling on the experimental discharged mass was done by dividing the recorded mass by the initial sample mass, as in the previous analysis. On the other hand the simulation data was scaled by dividing the number of fallen particles at any given moment by the total number of particles in the simulation. This different approach was needed due to the intrinsic discrete approach of the DEM model. With this particular normalization both of the dataseries will reach a value of 1 when the totality of the particles have been discharged.

The first row of Figure 6.10 shows three comparisons at different actuation frequencies between the results obtained with an experimental sample mass of 5 g and the equivalent simulations run with 1900 particles. In the second row, the discharge curves obtained with 10 g are compared with the simulation results with 3750 particles. An interesting point to note is that, while the inclination of the discharge curve might vary between experiment and simulation, the point in time from the start of the vibration at which the first particles are discharged is pretty much coincident between the two. Across various frequencies and for both of the tested masses, the

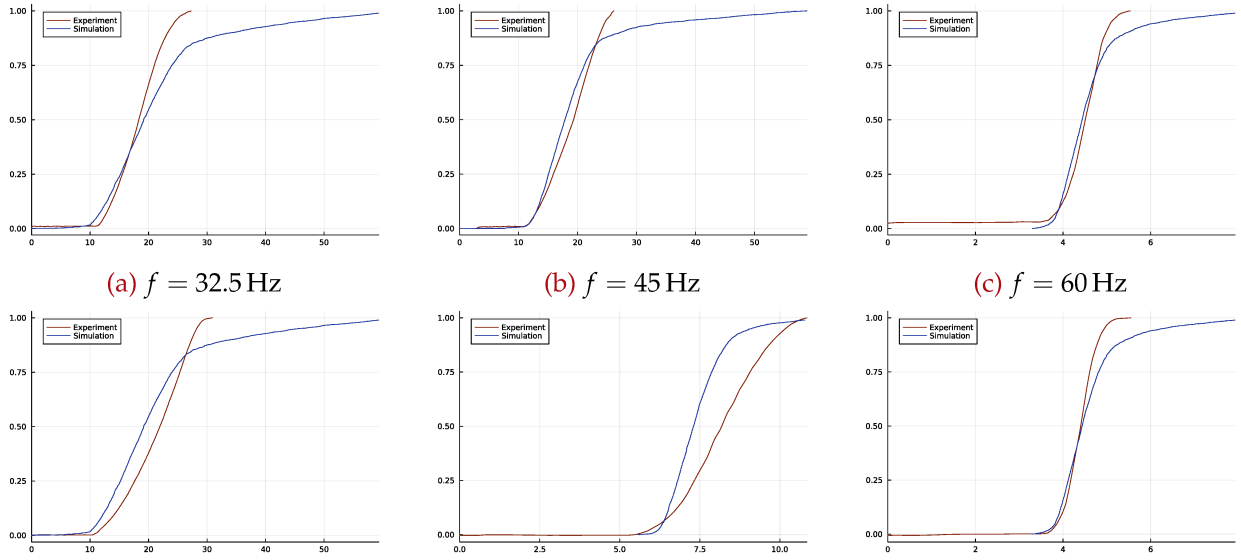

(a) $f = 32.5\,\text{Hz}$ (b) $f = 45\,\text{Hz}$ (c) $f = 60\,\text{Hz}$

(d) $f = 32.5\,\text{Hz}$ (e) $f = 45\,\text{Hz}$ (f) $f = 60\,\text{Hz}$

Figure 6.10: Comparison between experimental and simulated discharge curves for different frequencies and sample masses (and simulated particles). Top row $m = 5\,\text{g}$ and $N_p = 1900$; bottom row $m = 10\,\text{g}$ and $N_p = 3750$

time it takes for the material to travel across the trough is thus simulated with a high accuracy, with maximum differences in the order of a couple of seconds over the span of about a minute.

As mentioned earlier, the simulated discharge curves exhibit a distinct characteristic: a prolonged tail following the central quasi-linear zone. This indicates that a significant amount of time is required for the last 20 % of the total number of simulated particles to reach the edge of the trough. The reason behind this peculiarity can be attributed to the perfectly round shape of the simulated particles. In the simulation, these particles have the freedom to rotate without any limitations. As a result, they are unable to stack on top of each other, leading to a more dispersed distribution along the length of the trough compared to what is observed in the actual experiments. Furthermore, the perfectly round geometry makes it more difficult for the conveyor's vibrational motion to be converted in forward hops for the particles, since the movement along the x-axis of the trough is partially converted to rotation instead of translational velocity, for a factor much higher than what observed in asymmetric particles. This is a common problem in DEM simulations that make use of this kind of geometry [12], and the only way to counteract it would be to increase the rolling friction to unnatural levels or to lock the ability of the particles to rotate altogether, thus introducing a new set of problems in the overall behavior of the simulation. The optimal way would be the simulation of particles with a more complex geometry, but that would require a complete rewrite of the simulation code. Knowing the limitation of the model here implemented, it was chosen to consider only the central part of the discharge curve, in a way to reduce the impact of the long tails. in the mass flow computation By considering only the central 70 % of the curve it is possible to partially compensate the tail problem in the majority of the simulated results and to make the comparison with the experimental results more fair.

The mass flow was then computed, for both experiment and simulation, considering the dis-

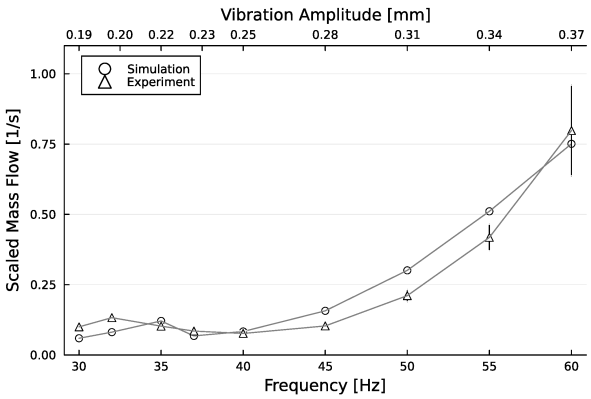

Figure 6.11: Comparison between the experimental and simulated evolution of the scaled mass flow for a 5 g sample mass

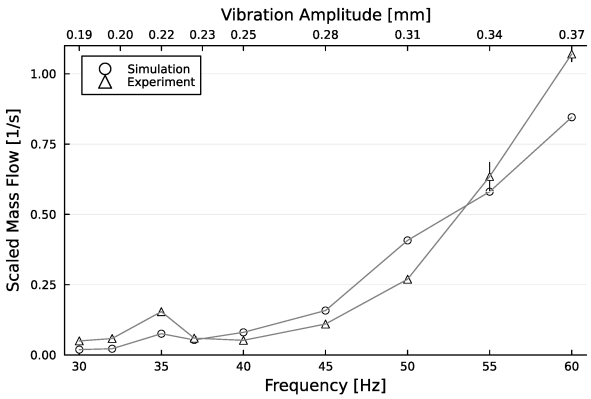

Figure 6.12: Comparison between the experimental and simulated evolution of the scaled mass flow for a 10 g sample mass

charge time between the first 10 % and the last 80 % of the total mass, or number of particles, in a way similar to what already presented in Chapter 5.4.4, obtaining the results in Figure 6.11 and 6.12. The error bars indicate one standard deviation computed from the original 6 experimental runs made for each experimental configuration. The simulated results show, at a first analysis, a good agreement with the experimental ones, at least regarding the evolution of the scaled mass flow with the frequency. The simulation was found to be able to predict the increase in discharged mass flow with the frequency for both the tested sample masses. In both cases the results are within what can be considered limited deviations from the experimental values, considering the rough estimation of the mechanical parameters and the simplicity of the 2D model.

In particular the percentage deviation of the simulated curves from the average experimental results, taken as reference, was computed, obtaining the data in Figure 6.13 and 6.14. These two figures offer a clearer visualization of the deviation between simulation and experiment highlighting how, across all tested frequency, the two curve differ at most of 50 %, in the case of a 5 g sample mass, and of 60 % in the case of 10 g of material. Some data points show some really good agreement with respect to percentage deviation, showing less than 10 % of difference. In both cases the percentage deviation between the two curves seem to reduce at higher frequency, also thanks to the fact that the reference experimental values are increasing while the absolute difference between the two stays within the same order of magnitude.

6.4.1 Upward transport capabilities

In this last section the comparison of the upward transport capabilities will be discussed. Since this is an important characteristic of a vibratory conveyor, it is relevant to compare the performance predicted by the simulation with the real data acquired on the experimental setup. The experimental reference data is the one presented in Chapter 5.4.5, regarding a sample mass of 10 g of glass spheres with a diameter of 200 µm transported along the conveyor set at an upward inclination of 5° with respect to the horizontal desk. The simulations were run with the all the same mechanical parameters as the one presented before, with the only exception of an inclined bottom boundary to simulate the inclination of the setup.

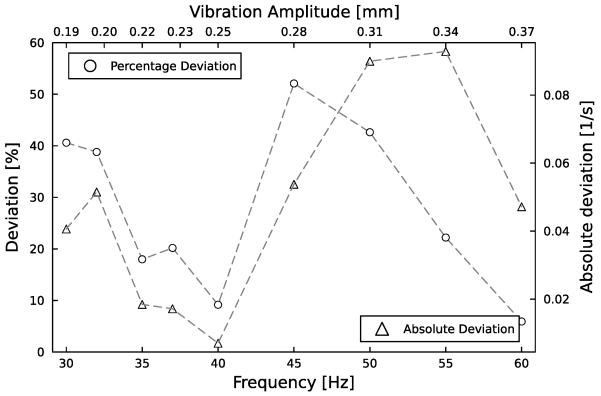

Figure 6.13: Percentage deviation between experimental and simulated mass flow curves (5 g - 1900 particle)

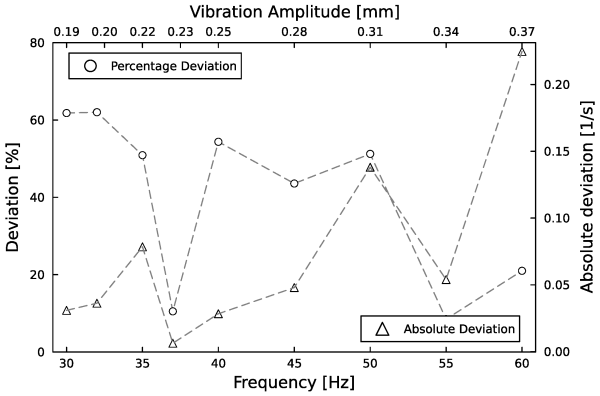

Figure 6.14: Percentage deviation between experimental and simulated mass flow curves (10 g - 3750 particle)

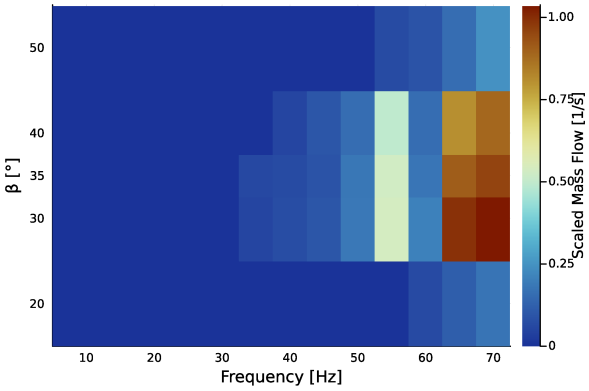

Figure 6.15: Heatmap of the experimental scaled mass flow for different frequencies and β angles ($\alpha = 5°$)

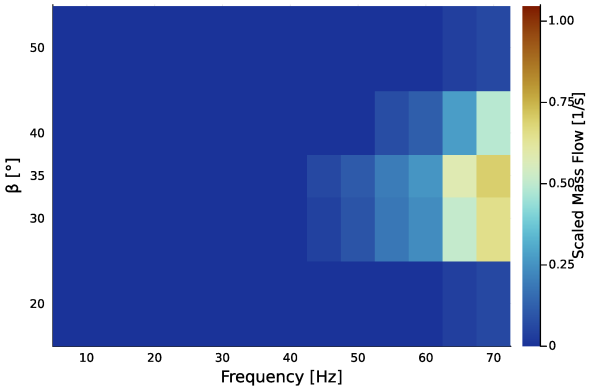

Figure 6.16: Heatmap of the simulated scaled mass flow for different frequencies and β angles ($\alpha = 5°$)

A first observation, made on the output videos of the simulations, was the accumulation of the particles on the starting end of the trough in the first seconds of the simulated time due to the inclination of the base. That is to be expected due to the perfectly circular geometry of the simulated particles, that thus tend to roll down the inclined trough without any kind of geometrical constraints that can limit their movement. This behavior will soon prove to be the main limit for the predictive capabilities of the model in this particular scenario since it will prove much more difficult for the simulated conveyor to push the particles upward along the incline. The variation of the β angle, that describes the inclination of the actuator with respect to the horizontal in the real setup, was simulated by changing the vibration pattern of the lower boundary. In particular, the horizontal and vertical component of the vibrations were computed by scaling the known variable amplitude by the cosine of the desired β angle to be simulated, making it possible to simulate the changing inclination of the virtual actuator.

The scaled mass flow was computed as usual, by dividing the number of fallen particles over time by the total amount, obtaining the scaled particle flow illustrated in Figure 6.16. Compared

to the experimental results presented in Chapter 5.4.5, the simulated scaled mass flow is overall much lower with a reduced zone in which transport is observed. It is possible to appreciate a reduction in the first transport frequency on the more extreme values of β, indicating that the predictive power of the model deteriorates quickly outside of the actuation zone for which it was calibrated. It is also interesting to note how the peak that was observed in the experimental data for frequency of 55 Hz seems to be lost in the simulated data. As for the other comparisons, one of the main factors that played in the reduction of the discharged mass flow was, probably, the perfect circularity of the simulated particles. In this particular scenario, with the virtual trough inclined of 5°, the particles are free to roll down along the incline without any kind of stopping action. Furthermore, the perfect circularity together with the low rolling friction makes it much more difficult for the movement of the trough to be transformed in forward jumps for the particles, since part of the energy is lost to the rotational degree of freedom.

As a final point, the difference between the simulated and experimental scaled mass flow were computed and the results plotted in the heatmap of Figure 6.17, where the values were computed as follows.

$$\Delta\bar{m}_s = \bar{m}_{sim} - \bar{m}_{exp} \tag{6.13}$$

The biggest deviations are observed in the higher range of frequencies, with reduction in scaled mass flow up to $0.5\,s^{-1}$ from what was observed experimentally. As previously noted, another big difference is along the column corresponding to a frequency of 55 Hz, where a strong reduction in scaled mass flow is observed due to the absence of the peak in the simulated data.

In general, it must be noted that the model shows much greater discrepancies with the experimental results for this configuration with $\alpha = 5°$ than with the horizontal conveyor. The inclination of the model plays an important role in the accuracy of the prediction and its influence on the results must be evaluated further to better characterize the model to make it a reliable design tool for vibrational conveyors.

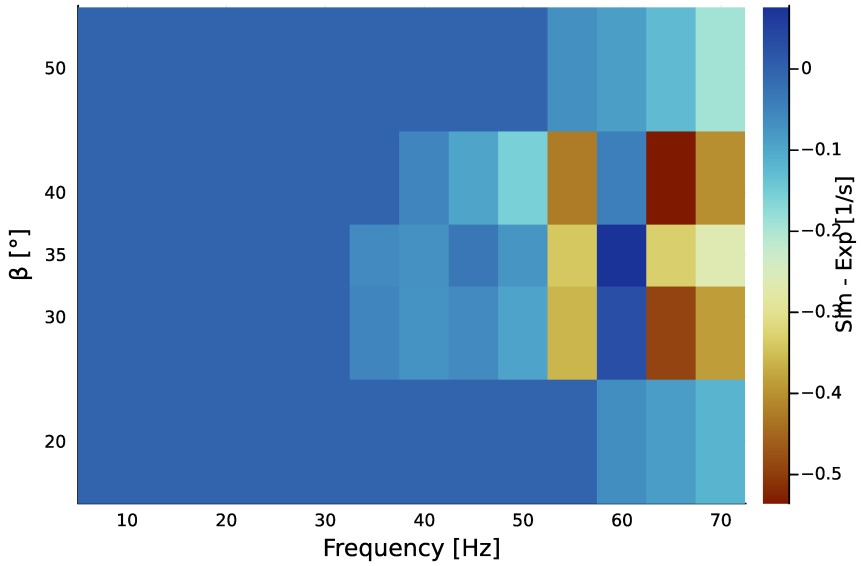

Figure 6.17: Heatmap of the difference between simulated and experimental scaled mass flow for different frequencies and β angles ($\alpha = 5°$

Chapter 7

Results

With the successful development, testing, and validation of the DEM code using real-life experimental data, it is time to employ this new instrument as a method for studying and predicting environments and configurations that have not been yet tested in real life. In this chapter some new results, based only on the simulation developed so far, will be presented. Specifically, the DEM code was employed to predict the behavior of a vibratory conveyor under the influence of lunar and Martian gravity conditions. By simulating the vibratory conveyor in these different gravitational environments, it is possible to gain important insights regarding its performance and operation capabilities in extraterrestrial settings. These predictions will offer new important information regarding the behavior of a conveyor system under reduced gravity conditions, facilitating the understanding of potential challenges and opportunities that may arise during extraterrestrial ISRU missions. Since the numerical model does not include any other environmental effect, such as aerodynamic drag or charging, the only variation with respect to the simulations presented so far will be a changed constant of gravitational acceleration that will take the values measured on the surface of Moon and Mars, respectively.

In both lunar and Martian gravity conditions, the gravitational acceleration experienced by the bulk material within the vibratory conveyor will be significantly lower compared to Earth's gravity. As discussed in Chapter 3.3, this difference in gravitational force will have an impact on the transport speed of the bulk material along the trough. By conducting simulations under lunar and Martian gravity, the DEM code will provide results specific to these extraterrestrial environments, which will then be compared to the findings obtained under Earth's gravity to study and comprehend the effects of gravity on the transport behavior of vibratory conveyors.

7.1 Simulations in lunar conditions

In the pursuit of expanding humanity's presence beyond Earth's boundaries, the Moon has become an enticing target for scientific exploration and resource utilization. Considering the unique characteristics of the Moon and the significance of utilizing available resources in-situ, the lunar surface offers a interesting environment for the deployment of vibratory conveyor technology. Such conveyors can play a crucial role in extracting and processing resources directly on the Moon's surface, minimizing the need for external supplies and enhancing self-sufficiency. That is

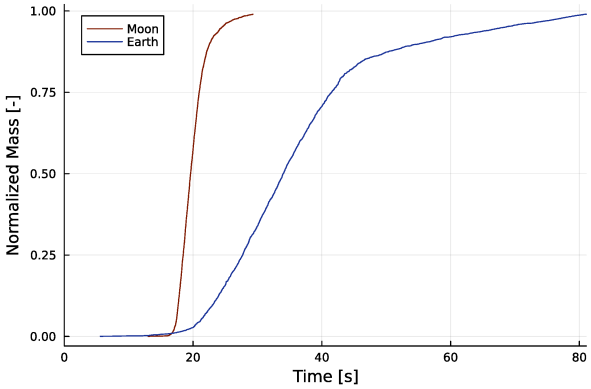

Figure 7.1: Comparison of simulated discharge curves, Earth - Moon (f =30 Hz)

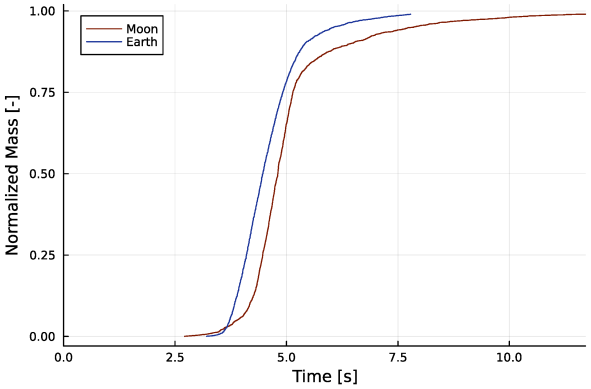

Figure 7.2: Comparison of simulated discharge curves, Earth - Moon (f =55 Hz)

why this chapter will delve into the simulation of a vibratory conveyor setup placed under lunar gravity. As previously said, the numerical model, in its current state, is only able to simulate the change in the gravitational acceleration that is observed in other celestial bodies. The gravitational acceleration on the Moon's surface is approximately 1.625 m s^{-2} [50], which is about 16.6 % that on Earth's surface, meaning that objects on the Moon will weigh about 1/6 of what they do on Earth.

The simulations were launched with the same mechanical parameters used in the ones made under Earth-like conditions, since the bulk's particles are considered to be the same. The simulation was run with about 3750 round particles which, following the conversion presented in Chapter 5.2.1, should represent the real life scenario of a vibratory conveyor with around 10 g of sample material. Just as before, the particles were considered mono-sized, with a diameter of 200 µm, since it was the only type of particles for which the validation results were available. To be able to compare these new simulations with the previous results the vibration settings were kept unchanged, with the same frequency range, going from 30 to 60 Hz, and the same variation of the amplitude with the frequency, as observed in the experimental setup. Two comparisons between the discharge patterns of the simulations done on Earth's gravity and those under Moon's gravity are presented in Figure 7.1 and 7.2, obtained with an actuation frequency of 30 Hz and 55 Hz respectively. The discharge curves obtained under lunar gravity are drawn in red, and it is clear how they correspond to higher mass flows given that they appear to be steeper, indicating a higher discharge rate over time. While the difference between the two curves is particularly evident at low frequency, as in Figure 7.1, it reduces at higher frequency, with the two curves going back to similar inclinations in their central part, as in Figure 7.2.

In addition to that, the scaled mass flow was computed. As explained before, in the case of simulations, the mass flow is to be intended more as a discrete particle flow, with the simulated particles falling out of the simulated trough over time. Just as before the mass flow, simulated and experimental, was scaled using the total number of particles or the total sample mass, respectively. The results are presented in Figure 7.3, where the evolution of the simulated mass flow over the frequency in lunar conditions is compared with the one obtained on Earth like gravity.

In Figure 7.3 it is possible to appreciate how the different gravitational acceleration causes no-

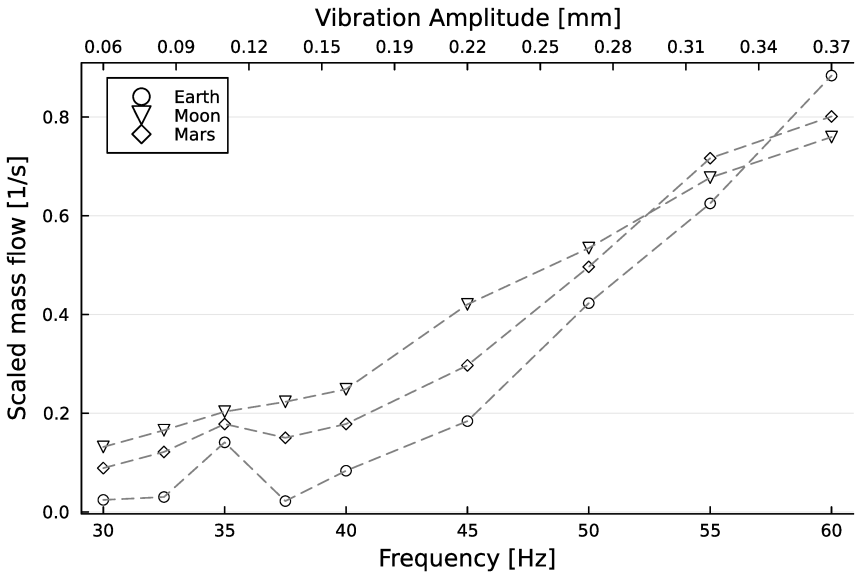

Figure 7.3: Comparison of scaled mass flow under Earth, Moon and Mars gravity

ticeable difference in the evolution of the mass flow with respect to the different frequencies. In particular it is possible to see how the scaled mass flow in lunar conditions is higher than on Earth for almost all actuation condition. Only in the last point of the graph, for an actuation frequency of 60 Hz, the mass flow predicted by the model under Earth gravity overcomes the lunar one achieving a scaled mass flow of almost $0.9\,s^{-1}$. In the lower frequency range the difference between the two conditions is stark, with the predicted lunar mass flow being almost five time higher than the reference. As the actuation frequency increases, the difference between the mass flow under lunar and earth gravity becomes increasingly smaller. This effect could be explained due to the different interaction between particles' and trough's motion since, while the vibratory motion of the trough is considered to be constant independently of the external environment, the particle's cinematic motion while hopping on the trough obviously depends on the gravitational acceleration of the planet. Remembering what was explained in the theory in Chapter 3.3, two of the important parameters that helps to shape the motion of hopping particles on a vibratory conveyor are the difference between trough's and gravitational acceleration, and the moment of impact of the particle on the moving trough along their parabolic trajectory. Both these parameters are heavily influenced by the change in gravitational acceleration because, while for the former the implication is clear, the differences in the latter becomes evident when thinking about the effect of a different acceleration on the trajectory of every single particle. Probably, at higher frequency, there is a sub optimal combination of these factors that slows the overall movement of the particles along the trough when compared to the same actuation frequency applied under Earth's gravity.

Another important difference that can be noted is the fact that, under Moon's gravity, the spike observed at around 35 Hz in all of the previous analysis is no more visible. The evolution of the scaled mass flow over frequency looks smooth and almost linear with no visible spikes. Even if the upward transport capabilities were not yet tested, it would be reasonable to expect that the conveyor under lunar gravity should perform even better than on Earth, since the lower gravitational acceleration should make it easier for the bulk's particle to climb to the trough's

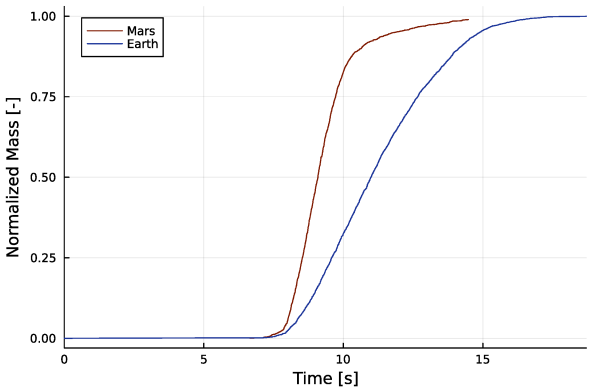

Figure 7.4: Comparison of simulated discharge curves, Earth - Mars ($f = 35\,\text{Hz}$)

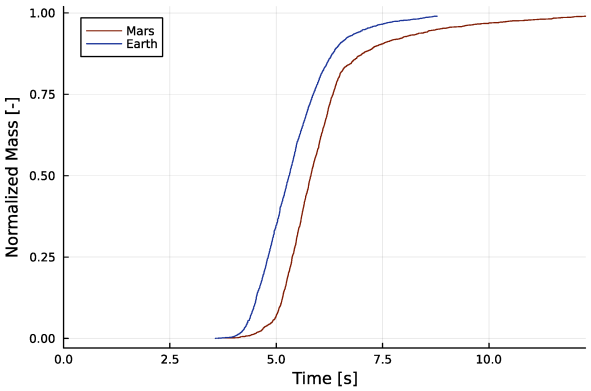

Figure 7.5: Comparison of simulated discharge curves, Earth - Mars ($f = 50\,\text{Hz}$)

edge without weighting down the particles under them too much. Keeping the same actuation parameters a higher mass flow should then be expected.

7.2 Simulations in martian conditions

The second tested condition was the one under Mars' gravitational acceleration. Since Mars is considered to be next big target for human exploration it is of great interest to start studying possible solutions to be used on future rovers and exploration systems that will need to transport small amounts of martian sand around. The simulation were conducted by imposing an average gravitation acceleration of $3.7208\,\text{m}\,\text{s}^{-2}$ [51], which corresponds to about 38 % of that of Earth. This means that object on the surface on Mars will weight about one third of what they normally do on Earth.

Just like for the lunar case, a whole set of simulations was run with this new gravity settings, covering the usual range of frequencies for a total number of particles of about 3750, equivalent to about 10 g of experimental glass spheres. An example of two simulated discharge curves, compared to the ones obtained under Earth gravity, are presented in Figure 7.4 and 7.5, obtained with an actuation frequency of 35 Hz and 50 Hz respectively. Again, even under martian gravity, the long discharge tails are present in the simulated discharge curves. In the two proposed example it is already clear how, at low frequencies the simulation under martian gravitational acceleration yielded a higher mass flow than what observed on Earth. At the same time, Figure 7.5 shows how the difference between the two curves is reduced at higher frequency, just like what was observed in the Moon's case. For a better analysis the next paragraph will focus on the computation and comparison of the mass flow at different frequencies.

As for all of the previous cases, the mass flow was computed considering the central 70 % of the total number of particles, between the first 10 % and the last 80 %, as to ignore the long final discharge tail. The results are presented in Figure 7.3 together with the ones obtained under Earth and Moon gravity. The data shows that the predicted scaled mass flow in martian gravity condition should be an intermediate between the lunar and terrestrial one, with the computed mass flow being almost constantly in the mean point between the other two data points for actuation frequencies lower than 55 Hz. Between 50 Hz and 55 Hz it is possible to note how the martian

scaled mass flow becomes higher than the one obtained on lunar conditions, producing a higher discharge rate also at the maximum simulated frequency of 60 Hz. While under Mars gravity, just like the results obtained in lunar condition, the mass flow is higher than the one observed on Earth for the majority of the tested frequency range, also in this case in the last tested frequency the predicted scaled mass flow in Earth gravity overcomes the one obtained on Mars, becoming, again the highest predicted mass flow.

The motivation behind this behavior can be linked to the same argumentation made for the Moon's case. The lower gravity helps in the transport of the bulk material in the trough due to the physical nature of the hopping transport. The particles are able to make bigger jumps given the same excitation energy thus making faster progress in their movement along the conveyor. For the same reason it could be possible to speculate that the different trajectory plays in favor of high frequencies on higher values of gravitational acceleration while, on celestial bodies with lower gravity, it would be beneficial to work with lower actuation frequencies, enabling the use of smaller, lighter and less powerful devices.

Chapter 8

Conclusions and outlook

In the field of In Situ Resource Utilization for planetary exploration and colonization a big open question is the identification of suitable logistical solutions for the transport of locally available material for both experimental and construction purposes. The necessity of harnessing the materials that are present on the surface of other planets and moons sparks from both the necessity of analyzing and transporting scientific samples of sand and rocks to various analysis instruments, and from the difficulty and cost of sending construction material from the Earth with traditional space launches. This thesis was aimed at addressing at least a part of the problem by focusing on the study of vibratory conveyors as a possible solution for the transport of small amount bulk materials in extraterrestrial environments, focusing on the possibility of utilizing them on the surface of the Moon.

Vibratory conveyors are a common industrial solution to the problem of transporting granulate materials being employed in a wide variety of application, from the movement of soils, to food processing, to pharmaceutical industries. As it was presented, they offer a noticeable set of advantages, being easy to clean, relatively low-maintenance than other types of mechanical conveyors, and with a fewer moving parts that could be subject to abrasion. Small vibratory conveyors are an ideal solution for moving modest amounts of material in a space application, being particularly low-power and able to sustain abrasion and corrosion due to special coatings and materials that can be used to build the trough. In the field of space application a particular interesting solution to the problem of generating the necessary vibrations of the trough is the use of piezoelectric actuators. In contrast to classical types of actuation based on the use of electric rotary motors, piezoelectric actuators convert electrical energy to mechanical energy directly without the use of moving parts, based on the principle of piezoelectricity, a property of certain materials that are able to deform when subjected to an electric field. The absence of moving part, low energy requirements, and the ability to work in a vacuum without major setbacks make this type of actuation an ideal choice for space application, so that is why it was chosen to be the actuation mechanism used in the experimental setup.

To help in the design of this kind of systems for future applications, a simulation framework was written from scratch to simulate the behavior of bulk materials on the trough of a vibratory conveyor. The numerical model was based on the Discrete Element Model (DEM) proposed by

Cundall in 1979. It describes granular materials as an assembly of thousands of virtual particles that are free to move in a mesh-less simulation domain and to interact and collide with each other. The implementation of the algorithm was written in the high-performance Julia Programming Language, as to optimize the performance of the code given the high computational load that are typical of these kinds of simulations. The simulation was built in a bidimensional domain to simplify the numerical scheme. To be able to utilize the code to obtain results that match with what is observed in real life an important step is its calibration, meaning the evaluation of the important parameters that must be changed in the code in order to make it produce results that are similar to reality, with the desired level of accuracy. That is part of the reasons why an extensive experimental campaign was conducted.

In particular, with the overall aim of increasing the knowledge regarding bulk material transport on vibratory conveyors and to produce useful data for calibration, an experimental campaign was conducted on a preexisting experimental setup at the Chair of Astronautics consisting on a vibratory conveyor setup actuated with a piezoelectric motor. The conveyor setup was fitted with a high-precision measuring scale to accurately evaluate the discharged mass released by the conveyor over time. This rig was used to gain data regarding the transport capabilities of the vibratory conveyor under different actuation configuration using, as a reference bulk material, a variable amount of glass spheres with a diameter of about 200 µm. The piezoelectric motor was excited as to produce vibrations at different frequencies, causing drastic changes in the transport behavior of the material.

It was noted how the amount of sample material on the trough has an influence in the normalized shape of the discharge pattern, with higher masses showing a higher mass flow in the first half of the discharge process than what is observed later, while the experiments with a lower mass showed the opposite. After scaling the time with the frequency, it was possible to observe that the relationship between actuation frequency and time of total discharge is super-linear. This proves to be an interesting starting point for future research since, the determination of a precise relationship between this two quantities could prove to be particularly useful in the design of control systems to be employed to precisely control the discharge flow of these systems.

All of the gathered data was put together to show the evolution of the discharged mass flow with the actuation frequency, noticing the presence of a spike in the mass flow at around 35 Hz which was attributed to the presence of some kind of mechanical resonance of the system. This led to further analysis of the behavior of the conveyor leading to the discovery of an important relation between the actuation frequency and the vibration amplitude, which were thought to be unrelated up until that point. Without the knowledge of the changing amplitude, gained with the additional experiments, it would have been impossible to correctly determine the origin of the observed spike. Finally the upward transport capabilities of the setup were explored by inclining the whole conveyor to a 5 deg angle showing that the system was able to easily transport material upward along the trough as long as the frequency was sufficiently high. This could prove to be particularly useful for ISRU application where the material will have to be gathered from the ground and transported up, towards some kind of analysis apparatus.

A set of simple experiments were devised to evaluate important mechanical parameters to be used in the simulation code. In particular, the coefficient of friction, friction angle, cohesion, and the coefficient of rolling friction were experimentally evaluated, obtaining important values that

were then introduced in the code. Against what observed in previous research, the coefficient of rolling friction was found to be related to the inclination angle of the surface. Given the low resolution of the employed instruments, the data here presented is not sufficient in drawing any kind of conclusions regarding that, but the data was still successfully used in the numerical simulation. Realizing that the 2D simulation could be considered as a longitudinal "slice" of the real 3D experiment, a simple conversion between the volume of sample material and an appropriate number of virtual particles to be used in the simulation was derived.

After the acquisition of all of this data, the simulation was updated with the newfound values and was then put to the test against a set of simple analytical cases, such as a bouncing ball or a ball rolling down an incline. This validation process proved the accuracy of the DEM model and of the underlying numerical scheme making it possible to test bigger simulations with a higher number of particles. The results of these simulations were compared with the experiments in terms of transport speed and mass flow. Even if a certain deviation was always present, the results of the DEM simulation can be considered satisfactory for its use as a preliminary design tool. The main sources of "error" between the simulation and the experimental data are to be attributed to the limited 2D domain of the code and to the perfectly circular particles used in the simulation.

The calibrated and validated DEM simulation was finally used to generate new results regarding the performance of the same vibratory conveyor under lunar and martian gravity. The simulated data showed a much higher mass flow than what was observed on Earth-like conditions, which was to be expected from the simple analytical theories that are commonly used for these systems. From the comparison of the discharged mass flow it was noted how it is possible to find an optimal frequency for each gravitation constant. In particular, for higher frequencies, higher values of gravitation acceleration proved to generate a higher mass flow, while lower gravitational accelerations worked best with lower actuation frequencies. This behavior is possibly linked to the different cinematic of the bulk's particles which, under different gravitational environment, respond in a different way to the excitation frequency.

The work presented so far shows numerous areas that could be improved in the future. Firstly the simulation code is in need of an important optimization work, including the integration of more advanced neighborhood algorithm such as the *sort and sweep* algorithm based on the computation of bounding boxes for each particle. In regards to the complexity of the particles interaction a big leap forward would be the integration of more advanced non-linear collision models which could be able to more accurately describe the interaction between virtual particles. On the other hand, the introduction of irregular polygonal particles could easily prevent all of the problems associated with the use of perfectly circular particles, making the simulation able to better predict complex emergent behaviors such as arching or locking between particles. Other interesting addition would be the introduction of the effect of tribocharging on the particles, a common long range interaction that is typical of these types of bulk materials. As a final point, the extension of the simulation to a tridimensional domain could prove to be the final step in increasing the quality of the simulation results and in obtaining more useful results in a wider variety of applications.

Ringraziamenti

Mi è doveroso dedicare questo spazio della mia tesi a tutte le persone che, nel corso della mia vita, mi hanno supportato nel mio percorso di crescita personale e professionale.

Un primo ringraziamento va al mio relatore, professor Zaccariotto, per il supporto durante il periodo di lavoro e scrittura.

Ai miei genitori, per il loro incrollabile sostegno, anno dopo anno, esame dopo esame, giorno dopo giorno. Sono stati i loro continui sacrifici e il loro costante impegno e supporto a permettermi di arrivare fino a qui, dove sono adesso. Quindi grazie, dal profondo del mio cuore.

A tutta la mia famiglia che, standomi accanto per tutti questi anni, mi ha dato sempre la forza di andare avanti, contro ogni difficoltà sul mio percorso. A mia sorella, ai nonni, agli zii e ai cugini va il mio più grande ringraziamento e un forte abbraccio.

Un ringraziamento particolarmente sentito deve andare alla Cattedra di Tecnologie per l' Esplorazione Lunare e Planetaria della Technische Universität München (TUM). Il continuo sostegno e aiuto da parte di Alexander Smolka, del Prof. Philipp Reiss, e di tutto il suo gruppo di ricerca, sono stati fondamentali per la buona riuscita di questo lavoro di ricerca, a partire dall'ideazione, fino alla esecuzione della parte sperimentale. L'esperienza dei mesi passati a Monaco di Baviera rimarrà per sempre nel mio cuore.

Un ringraziamento speciale va ad Asia, con cui abbiamo affrontato tante avventure e difficoltà, e non mi ha mai fatto mancare il supporto di cui ho avuto bisogno (e di cui sicuramente necessiterò ancora) in tutti i momenti più difficili questi mesi e anni di lavoro e studio. E un posto speciale nel mio cuore va a tutti i miei amici, Davide, Alessandro, Andrea, Giovanni, Tomás, e a tutti gli altri che hanno condivisio con me questo percorso. Grazie per essere stati, giorno dopo giorno, fonte inesauribile di supporto, risate, discorsi, bevute e lauti pranzi. Grazie a tutti i ragazzi del progetto Lift UP, che mi hanno fatto vivere una grande avventura e mi hanno permesso di mettermi in gioco. Questi anni di Università non sarebbero stati gli stessi senza tutti voi.

In ultimo, un grazie a me stesso, per non aver mollato anche quando sembrava tutto nero. Che questo possa essere il primo grande traguardo di una vita lunga e felice.

Per aspera ad astra

Bibliography

[1] Yue Jing Zhao, Feng Shan Huang, and Zhi Lin Zhao. "Dynamic Analysis on Vertical Vibratory Conveyor". In: *Advanced Materials Research* 694–697 (May 2013), pp. 3–6. ISSN: 1662-8985. DOI: 10.4028/www.scientific.net/AMR.694-697.3. (Visited on 04/14/2023).

[2] P. A. Cundall and O. D. L. Strack. "A Discrete Numerical Model for Granular Assemblies". In: *Géotechnique* 29.1 (Mar. 1979), pp. 47–65. ISSN: 0016-8505, 1751-7656. DOI: 10.1680/geot.1979.29.1.47. (Visited on 10/12/2022).

[3] Huazhi Chen et al. "A Vibratory Conveying Method for Planetary Regolith: Preliminary Experiment and Numerical Simulation". In: *IEEE Access* 7 (2019), pp. 29386–29396. ISSN: 2169-3536. DOI: 10.1109/ACCESS.2019.2902348. (Visited on 10/10/2022).

[4] Zeljko Despotovic et al. "Vibration Control of Resonant Vibratory Feeders with Electromagnetic Excitation". In: *FME Transaction* 42.4 (2014), pp. 281–289. ISSN: 1451-2092. DOI: 10.5937/fmet1404281d. (Visited on 03/09/2023).

[5] Željko V. Despotović et al. "Mathematical Modeling of Resonant Linear Vibratory Conveyor with Electromagnetic Excitation: Simulations and Experimental Results". In: *Applied Mathematical Modelling* 41 (Jan. 2017), pp. 1–24. ISSN: 0307904X. DOI: 10.1016/j.apm.2016.09.010. (Visited on 03/09/2023).

[6] P.A. Cundall. "Formulation of a Three-Dimensional Distinct Element Model—Part I. A Scheme to Detect and Represent Contacts in a System Composed of Many Polyhedral Blocks". In: *International Journal of Rock Mechanics and Mining Sciences & Geomechanics Abstracts* 25.3 (June 1988), pp. 107–116. ISSN: 01489062. DOI: 10.1016/0148-9062(88)92293-0. (Visited on 10/15/2022).

[7] R Hart, P A CUNDALLt, and J Lemos. "Formulation of a Three-dimensional Distinct Element Model Part II. Mechanical Calculations for Motion and Interaction of a System Composed of Many Polyhedral Blocks". In: (1988), p. 9.

[8] John M. Ting et al. "An Ellipse-Based Discrete Element Model for Granular Materials". In: *International Journal for Numerical and Analytical Methods in Geomechanics* 17.9 (Sept. 1993), pp. 603–623. ISSN: 0363-9061, 1096-9853. DOI: 10.1002/nag.1610170902. (Visited on 01/17/2023).

[9] J. Morris et al. "The Distinct Element Method - Application to Structures in Jointed Rock". In: (Nov. 2001).

[10] J.C. Laurentie, P. Traoré, and L. Dascalescu. "Discrete Element Modeling of Triboelectric Charging of Insulating Materials in Vibrated Granular Beds". In: *Journal of Electrostatics* 71.6 (Dec. 2013), pp. 951–957. ISSN: 03043886. DOI: 10.1016/j.elstat.2013.08.001. (Visited on 10/12/2022).

[11] J.N. Rasera et al. "Modelling the Tribocharging Process in 2D and 3D". In: *Powder Technology* 407 (July 2022), p. 117607. ISSN: 00325910. DOI: 10.1016/j.powtec.2022.117607. (Visited on 10/09/2022).

[12] C. R. Woodcock and J. S. Mason. *Bulk Solids Handling*. Dordrecht: Springer Netherlands, 1988. ISBN: 978-94-010-7689-0 978-94-009-2635-6. DOI: 10.1007/978-94-009-2635-6. (Visited on 12/26/2022).

[13] Xiangwu Zeng, Chunmei He, and Allen Wilkinson. "Geotechnical Properties of NT-LHT-2M Lunar Highland Simulant". In: *Journal of Aerospace Engineering* 23.4 (Oct. 2010), pp. 213–218. ISSN: 0893-1321, 1943-5525. DOI: 10.1061/(ASCE)AS.1943-5525.0000026. (Visited on 03/25/2023).

[14] K. R. Schrag and M. Corn. "Comparison of Particle Size Determined with the Coulter Counter and by Optical Microscopy". In: *American Industrial Hygiene Association Journal* 31.4 (July 1970), pp. 446–453. ISSN: 0002-8894. DOI: 10.1080/0002889708506272. (Visited on 03/25/2023).

[15] M. Cyr and A. Tagnit-Hamou. "Particle Size Distribution of Fine Powders by LASER Diffraction Spectrometry. Case of Cementitious Materials". In: *Materials and Structures/Matériaux et Constructions* 34 (July 2001), pp. 342–350.

[16] A. Castellanos et al. "Cohesion and Internal Friction of Fine Glass Beads as Affected by Small Intensity Vertical Vibration". In: *AIP Conference Proceedings*. Golden (Colorado): AIP, 2009, pp. 707–710. DOI: 10.1063/1.3180025. (Visited on 11/14/2022).

[17] T. Eaves and T. M. Jones. "Cohesion and Tensile Strength of Bulk Solids". In: *Rheologica Acta* 10.1 (Mar. 1971), pp. 127–134. ISSN: 0035-4511, 1435-1528. DOI: 10.1007/BF01972489. (Visited on 03/26/2023).

[18] Michael J. Carr, Alan W. Roberts, and Craig A. Wheeler. "A Revised Methodology for the Determination of Bulk Material Cohesion and Adhesion". In: *Advanced Powder Technology* 30.10 (Oct. 2019), pp. 2110–2116. ISSN: 09218831. DOI: 10.1016/j.apt.2019.06.025. (Visited on 03/26/2023).

[19] A. Drescher, A. J. Waters, and C. A. Rhoades. "Arching in Hoppers: I. Arching Theories and Bulk Material Flow Properties". In: *Powder Technology* Volume 84.Issue 2 (Aug. 1995), pp. 165–176. DOI: 10.1016/0032-5910(95)02981-7.

[20] Nepu Saha et al. "Characterization of Particle Size and Moisture Content Effects on Mechanical and Feeding Behavior of Milled Corn (Zea Mays L.) Stover". In: *Powder Technology* 405 (June 2022), p. 117535. ISSN: 00325910. DOI: 10.1016/j.powtec.2022.117535. (Visited on 03/26/2023).

[21] Ch J. Boukouvalas et al. "Effect of Material Moisture Content and Temperature on the True Density of Foods". In: *International Journal of Food Properties* 9.1 (Apr. 2006), pp. 109–125. ISSN: 1094-2912, 1532-2386. DOI: 10.1080/10942910500473970. (Visited on 03/26/2023).

[22] Claudia C. Corredor, Dongsheng Bu, and Douglas Both. "Comparison of near Infrared and Microwave Resonance Sensors for At-Line Moisture Determination in Powders and Tablets". In: *Analytica Chimica Acta* 696.1-2 (June 2011), pp. 84–93. ISSN: 00032670. DOI: 10.1016/j.aca.2011.03.048. (Visited on 03/27/2023).

[23] Ernest W. Tollner and W. L. Rollwitz. "Nuclear Magnetic Resonance for Moisture Analysis of Meals and Soils". In: *Transactions of the ASAE* 31.5 (1991), pp. 1608–1615. ISSN: 2151-0059. DOI: 10.13031/2013.30908. (Visited on 03/27/2023).

[24] Oleksandr Zabolotnyi and Mikola Koshevoi. "An Effective Method of Bulk Materials Moisture Measurement Using Capacitive Sensors". In: *Journal of Stored Products Research* 89 (Dec.

2020), p. 101733. ISSN: 0022474X. DOI: 10.1016/j.jspr.2020.101733. (Visited on 03/26/2023).

[25] Hiroyuki Kawamoto, Kazuaki Nogami, and Yuta Kadono. "Vibration Conveyance of Lunar Regolith in Lunar Environment". In: *Acta Astronautica* 197 (Aug. 2022), pp. 139–144. ISSN: 00945765. DOI: 10.1016/j.actaastro.2022.05.028. (Visited on 10/09/2022).

[26] Domingos Rade et al. "Piezoelectric Driving of Vibration Conveyors: An Experimental Assessment". In: *Sensors* 13.7 (July 2013), pp. 9174–9182. ISSN: 1424-8220. DOI: 10.3390/s130709174. (Visited on 12/26/2022).

[27] Laura Grill. "Lab Bench Report". In: (2020), p. 33.

[28] Carter and Kensley. *Introduction to Piezoelectric Transducers*. Piezo.com, 2022. (Visited on 03/09/2023).

[29] Stefan Johann Rupitsch. *Piezoelectric Sensors and Actuators: Fundamentals and Applications*. Topics in Mining, Metallurgy and Materials Engineering. Berlin, Heidelberg: Springer Berlin Heidelberg, 2019. ISBN: 978-3-662-57532-1 978-3-662-57534-5. DOI: 10.1007/978-3-662-57534-5. (Visited on 03/09/2023).

[30] H. A. Gaberson. "Particle Motion on Oscillating Conveyors". In: *Journal of Engineering for Industry* (Feb. 1972).

[31] Jeff Bezanson et al. "Julia: A Fresh Approach to Numerical Computing". In: *SIAM review* 59.1 (2017), pp. 65–98.

[32] Hans-Georg Matuttis and J. F. Chen. *Understanding the Discrete Element Method: Simulation of Non-Spherical Particles for Granular and Multi-Body Systems*. Hoboken, NJ: John Wiley & Sons Inc, 2014. ISBN: 978-1-118-56720-3.

[33] K Maslova, V L B de Jesus, and D G G Sasaki. "Understanding the Effect of Rolling Friction in the Inclined Track Experiment". In: *Physics Education* 55.5 (Sept. 2020), p. 055010. ISSN: 0031-9120, 1361-6552. DOI: 10.1088/1361-6552/ab9217. (Visited on 01/26/2023).

[34] Rod Cross. "Simple Measurements of Rolling Friction and Deformation When $\mu_r < 0.001$". In: *European Journal of Physics* 36.6 (Nov. 2015), p. 065018. ISSN: 0143-0807, 1361-6404. DOI: 10.1088/0143-0807/36/6/065018. (Visited on 04/13/2023).

[35] Carl E Mungan. "Rolling Friction on a Wheeled Laboratory Cart". In: *Physics Education* 47.3 (May 2012), pp. 288–292. ISSN: 0031-9120, 1361-6552. DOI: 10.1088/0031-9120/47/3/288. (Visited on 04/13/2023).

[36] A. Doménech, T. Doménech, and J. Cebrián. "Introduction to the Study of Rolling Friction". In: *American Journal of Physics* 55.3 (Mar. 1987), pp. 231–235. ISSN: 0002-9505, 1943-2909. DOI: 10.1119/1.15223. (Visited on 04/13/2023).

[37] Hans-Georg Matuttis. "Simulation of the Pressure Distribution under a Two-Dimensional Heap of Polygonal Particles". In: *Granular Matter* 1.2 (Sept. 1998), pp. 83–91. ISSN: 1434-5021, 1434-7636. DOI: 10.1007/s100350050013. (Visited on 01/17/2023).

[38] John M. Ting and Brent T. Corkum. "Computational Laboratory for Discrete Element Geomechanics". In: *Journal of Computing in Civil Engineering* 6.2 (Apr. 1992), pp. 129–146. ISSN: 0887-3801, 1943-5487. DOI: 10.1061/(ASCE)0887-3801(1992)6:2(129). (Visited on 11/25/2022).

[39] N T Bridges and M Benzit. "MEASUREMENTS OF THE COEFFICIENT OF RESTITUTION OF QUARTZ SAND ON BASALT: IMPLICATIONS FOR ABRASION RATES ON EARTH AND MARS M." In: (2005).

[40] Graham Weir and Peter McGavin. "The Coefficient of Restitution for the Idealized Impact of a Spherical, Nano-Scale Particle on a Rigid Plane". In: *Proceedings of the Royal Society A:*

Mathematical, Physical and Engineering Sciences 464.2093 (May 2008), pp. 1295–1307. ISSN: 1364-5021, 1471-2946. DOI: 10.1098/rspa.2007.0289. (Visited on 04/13/2023).

[41] Goro Kuwabara and Kimitoshi Kono. "Restitution Coefficient in a Collision between Two Spheres". In: *Japanese Journal of Applied Physics* 26.8R (Aug. 1987), p. 1230. ISSN: 0021-4922, 1347-4065. DOI: 10.1143/JJAP.26.1230. (Visited on 01/17/2023).

[42] Kristoffer Carlson. *DifferentialEquations.Jl*. 2022.

[43] H. Kruggel-Emden et al. "Selection of an Appropriate Time Integration Scheme for the Discrete Element Method (DEM)". In: *Computers & Chemical Engineering* 32.10 (Oct. 2008), pp. 2263–2279. ISSN: 00981354. DOI: 10.1016/j.compchemeng.2007.11.002. (Visited on 04/10/2023).

[44] Ch. Tsitouras. "Runge–Kutta Pairs of Order 5(4) Satisfying Only the First Column Simplifying Assumption". In: *Computers & Mathematics with Applications* 62.2 (July 2011), pp. 770–775. ISSN: 08981221. DOI: 10.1016/j.camwa.2011.06.002. (Visited on 04/10/2023).

[45] David B Newell and Eite Tiesinga. *The International System of Units (SI):: 2019 Edition*. Tech. rep. NIST SP 330-2019. Gaithersburg, MD: National Institute of Standards and Technology, Aug. 2019, NIST SP 330–2019. DOI: 10.6028/NIST.SP.330-2019. (Visited on 03/02/2023).

[46] Open Source Physics (OSP). *Tracker*. Open Source Physics (OSP). 2023.

[47] OSPP. *Open Source Physics*. 2023.

[48] Rahul K Soni. "Studies and Implementation of Discrete Element Method (DEM)". In: (2011). DOI: 10.13140/RG.2.2.33072.15366. (Visited on 10/30/2022).

[49] B.K. Mishra and Raj K. Rajamani. "The Discrete Element Method for the Simulation of Ball Mills". In: *Applied Mathematical Modelling* 16.11 (Nov. 1992), pp. 598–604. ISSN: 0307904X. DOI: 10.1016/0307-904X(92)90035-2. (Visited on 03/17/2023).

[50] C. Hirt and W.E. Featherstone. "A 1.5km-Resolution Gravity Field Model of the Moon". In: *Earth and Planetary Science Letters* 329–330 (May 2012), pp. 22–30. ISSN: 0012821X. DOI: 10.1016/j.epsl.2012.02.012. (Visited on 04/11/2023).

[51] C. Hirt et al. "Kilometer-Resolution Gravity Field of Mars: MGM2011". In: *Planetary and Space Science* 67.1 (July 2012), pp. 147–154. ISSN: 00320633. DOI: 10.1016/j.pss.2012.02.006. (Visited on 04/12/2023).

Appendix A

Experimental Data

A.1 Estimation of rolling friction coefficient

Table A.1: Results of the rolling friction coefficient experiment with a conveyor angle of 5°

	Time $[s]$	Acc $[m/s^2]$	μ_R
Run 1	12,9	0,0030	0,0622
Run 2	7,9	0,0080	0,0617
Run 3	8,5	0,0069	0,0618
Run 4	9,9	0,0051	0,0620
Run 5	9,2	0,0059	0,0619
Run 6	7,7	0,0084	0,0616
Run 7	7,9	0,0080	0,0617
Run 8	9,8	0,0052	0,0620
Run 9	9,3	0,0058	0,0619
Run 10	9,1	0,0060	0,0619
Run 11	8,2	0,0074	0,0617
Run 12	7,2	0,0096	0,0615
Run 13	6,9	0,0105	0,0614
Run 14	7,4	0,0091	0,0616
Avg	8,7	0,0071	0,0618

A.2 Tilting Plate experiment data

Table A.2: Results of the rolling friction coefficient experiment with a conveyor angle of 10°

	Time $[s]$	Acc $[m/s^2]$	μ_R
Run 1	4,5	0,0247	0,1234
Run 2	2,9	0,0595	0,1198
Run 3	2,8	0,0638	0,1193
Run 4	3,1	0,0520	0,1206
Run 5	3	0,0556	0,1202
Run 6	3,2	0,0488	0,1209
Run 7	2,9	0,0595	0,1198
Run 8	2,8	0,0638	0,1193
Run 9	3,6	0,0386	0,1220
Run 10	3,4	0,0433	0,1215
Run 11	3	0,0556	0,1202
Run 12	3,1	0,0520	0,1206
Run 13	2,9	0,0595	0,1198
Run 14	2,8	0,0638	0,1193
Avg	3,1	0,0529	0,1205

Table A.3: Experiment results for the evaluation of shear friction coefficients with tilting plate method

ID	Mass [g]	L [mm]	α [deg]	$mg/A \cos ff$	$mg/A \sin ff$
1	8,0	50	13,5	0,029	0,0071
2	8,0	80	19	0,018	0,0062
3	8,0	100	18	0,014	0,0047
4	16,9	60	11	0,052	0,0101
5	16,9	90	13,5	0,034	0,0082
6	16,9	100	13	0,031	0,0072
7	16,9	120	17	0,025	0,0077
8	32,1	50	10	0,119	0,0210
9	32,1	80	10	0,075	0,0131
10	32,1	100	12	0,059	0,0126
11	32,1	120	16	0,049	0,0139
12	32,1	140	14	0,042	0,0105
13	32,1	160	15	0,037	0,0098
14	32,1	180	17	0,032	0,0098
15	48,2	50	7	0,180	0,0221
16	48,2	80	8,5	0,112	0,0168
17	48,2	120	11	0,074	0,0144
18	48,2	100	10	0,089	0,0158
19	48,2	150	13	0,059	0,0136
20	48,2	170	15	0,052	0,0138
21	64,2	120	10	0,099	0,0175
22	64,2	140	11	0,085	0,0165
23	64,2	160	14	0,073	0,0183
24	64,2	180	16	0,065	0,0186